Quantum Phase Transitions in Collective Spin Models. Applications to Adiabatic Quantum Computation

Pedro Ribeiro

UNIVERSITE PIERRE & MARIE CURIE
LA SCIENCE A PARIS

Thèse de Doctorat de l'Université Paris VI - Pierre et Marie Curie

Champ disciplinaire: Physique

Présentée par RIBEIRO Pedro

Pour l'obtention du grade de Docteur de l'Université Pierre et Marie Curie.

Sujet de thèse:

Transitions de Phase Quantiques dans des Modèles de Spin Collectif. Applications au Calcul Adiabatique

---

Quantum Phase Transitions in Collective Spin Models. Applications to Adiabatic Quantum Computation

---

Thèse dirigée par Mosseri Rémy

Au Laboratoire Physique Théorique de la Matière Condensée

Soutenue le 12 septembre 2008

Devant le jury composé de:

M. CERF, Nicolas - (Professeur, QuIC Bruxelles) - Rapporteur
M. ESTÈVE, Daniel - (Ingénieur CEA) - Examinateur
M. HAROCHE, Serge - (Prof. Collège de France, LKB-ENS-UPMC) - Examinateur
M. LEBOEUF, Patricio - (DR CNRS, Orsay) - Rapporteur
M. MOSSERI, Rémy - (DR CNRS, UPMC) - Directeur de Thèse
M. SACRAMENTO, Pedro D. - (Professeur, IST Lisbonne) - Examinateur

Auteur: Pedro RIBEIRO,

Laboratoire de Physique Théorique de la Matière Condensée,
Université Pierre et Marie Curie
Tour 24, Boîte 121, 4, Place Jussieu,
75252 Paris Cedex 05, France

. 2008

Transitions de Phase Quantiques dans des Modèles de Spin Collectif. Applications au Calcul Adiabatique

Résumé

Partie I: Modèles de spin collectif
On utilise le formalisme des états cohérents de spin pour étudier des modèles de spin collectif, qui ont plusieurs champs d'application en physique. Le modèle de Lipkin-Meshkov-Glick (LMG) a en particulier été analysé à la limite thermodynamique. La méthode développée au cours de ce travail peut être utilisée, en principe, pour des Hamiltoniens plus généraux, s'écrivant en fonction des générateurs de l'algèbre su(2).
Nous avons pu dériver exactement la densité d'états intégrée du modèle. La nature des singularités de la densité d'états a été mise en évidence. Les premières corrections de taille finie ont également été calculées. Les valeurs moyennes d'observables ont été étudiées.
Près des singularités, la quantification de Bohr-Sommerfeld, adaptée aux spins, n'est pas valable. Pour traiter ces cas, nous avons développé une nouvelle approche, permettant alors de décrire le spectre au voisinage des points critiques.

Partie II : Calcul quantique adiabatique
Nous avons construit un modèle simple permettant de mettre en évidence la relation entre les transitions de phase quantiques et le calcul (quantique) adiabatique. Ce modèle met en évidence l'importance du choix du Hamiltonien initial et du chemin adiabatique considéré dans l'espace des paramètres, et peut servir comme un cas d'école pour des modèles plus réalistes.
Nous avons enfin étudié la dynamique des populations des états à travers une transition de phase, pour le cas du modèle LMG abordé dans la première partie. Une analyse numérique nous a montré que ces changements de population sont très sensibles à la présence des points exceptionnels dans le spectre, ce qu'un modèle simplifié de l'évolution quantique permettait de suggérer.

Mots clés

Transitions de Phase Quantiques
Traitement Quantique de l'Information
Modèles de Spin Collectif
Modèle de Lipkin-Meshkov-Glick
États cohérents de Spin
Représentation de Majorana
Limite Semi-classique
Calcul Quantique Adiabatique

Quantum Phase Transitions in Collective Spin Models.
Applications to Adiabatic Quantum Computation

Abstract

Part I: Quantum Collective Spin Systems
We use a coherent spin state formalism in order to study collective spin models, which have many applications in physics. In particular, the Lipkin-Meshkov-Glick (LMG) has been analyzed in the thermodynamic limit. The method developed during this work can, in principle, be used for more general Hamiltonians written as a function of the su(2) algebra generators.
We have derived exact expressions for the integrated density of states for this model. The nature of the density of states singularities has been detailed. The first order finite size corrections as well as observables expectation values were also computed.
The standard Bohr-Sommerfeld quantization approach, adapted to the spin case, is no longer valid near the spectral singularities. In order to treat these cases, we have developed a new approach that permits to describe the spectrum in the neighbourhood of the critical points.

Part II: Adiabatic Quantum Computation
We have proposed a simple model which highlights the relations between quantum phase transitions and adiabatic (quantum) computation. This model puts in evidence the importance of the choice of the initial Hamiltonian and of the adiabatic path in the parameter space; it should be helpful as a toy model for more realistic cases.
We have also studied the state populations dynamics when a quantum phase transition point is crossed, for the LMG model studied in the first part. Numerical simulations show that the dynamics of the populations is very sensitive to the presence of exceptional points in the spectrum, which a simplified model for the quantum evolution already suggests.

Key words

Quantum Phase Transitions
Quantum Information
Collective Spin Systems
Lipkin-Meshkov-Glick Model
Coherent Spin States
Majorana Representation
Semi-classical Limit
Adiabatic Quantum Computation

Remerciements - Acknowledgements

P. Ribeiro was partially supported by FCT and EU FEDER through POCTI and QuantLog POCI/MAT/55796/2004 Project of CLC-DM-IST, SQIG-IT and grant SFRH/BD/16182/2004/2ZB5.

Contents

Part I

Quantum Collective Spin Systems

Résumé

Les modèles de spin collectif apparaissent assez naturellement dans de nombreux domaines de la physique, par exemple dans l'étude de systèmes à deux niveaux avec des interactions symétriques ou bien encore dans des systèmes bosoniques (du à des symétries particulières du Hamiltonien). On se concentre le plus souvent sur le secteur symétrique de spin total maximum s qui contient en général l'état fondamental du système. Pour ces modèles le Hamiltonien conserve le spin total s et peut être écrit en fonction des opérateurs de spin S_i $(i = x, y, z)$ qui sont les générateurs de l'algèbre $su(2)$ correspondante.

Dû à la simplicité de l'algèbre $su(2)$, ces modèles sont integrables, ce qui veut dire qu'il est possible de donner un ensemble de relations explicites permettant de caractériser les états propres et les énergies propres du Hamiltonien. Ces relations surgissent assez naturellement quand on utilise le formalisme des états cohérents de spin, cadre dans lequel s'exprime très simplement la représentation de Majorana pour des spins quelconques. La fonction d'onde dans cette représentation est donnée par un polynôme d'ordre $2s$ et peut donc être complètement caractérisée, à une constante non physique près, par la donnée de l'ensemble de ses zéros. Il est alors possible d'écrire explicitement des équations (en général compliquées) pour les zéros des fonctions propres et les énergies associées.

Nous nous sommes intéressés en particulier ici à la limite thermodynamique, où le nombre de sous-systèmes en interaction tend vers l'infini ($s \to \infty$). Cette limite peut être vue comme l'analogue de la limite semi-classique de la mécanique quantique où $2s$ joue le rôle de l'inverse de la constante de Planck $\hbar^{-1}$. Dans cette limite, une approche du type WKB et des règles de quantification à la Bohr-Sommerfeld, adaptées au cas des spins, permettent d'obtenir le spectre du système.

Dans cette partie de la thèse, le modèle de Lipkin-Meshkov-Glick (LMG) est étudié dans le détail. Ce modèle a été introduit il y a plus de quarante ans, dans le domaine de la physique nucléaire, pour étudier les transitions de phase dans des noyaux; mais il a été utilisé depuis (et redécouvert) dans beaucoup d'autres domaines, comme par exemple pour l'étude des propriétés magnétiques de certaines molécules, de systèmes de bosons en interaction dans des structures de double puits, de condensats de Bose-Einstein, ou enfin de jonctions Josephson.

Nous avons pu résoudre exactement le spectre du modèle LMG dans limite thermodynamique. La méthode développée au cours de ce travail peut être utilisée, en principe, pour tout Hamiltonien qui s'écrit en fonction des générateurs de $su(2)$. Dans un premier temps, une analyse de type champ moyen a été effectuée conduisant à une mise en relation entre les singularités des orbites semi-classiques et celles du spectre du modèle. Cela

nous a permis de caractériser différentes régions dans l'espace de paramètres du modèle, distinctes quant à leurs propriétés spectrales. Ces singularités de la densité d'états, qui se produisent pour des niveaux excités (appelés parfois "points exceptionnels"), peuvent d'un certain point de vue être considérées comme engendrant une généralisation des transitions de phase quantiques habituelles, non plus au niveau de l'état fondamental, mais à l'intérieur du spectre.

L'analyse de la structure des zéros du polynôme de Majorana associé aux états propres nous a permis de dériver exactement la densité d'états intégrée du modèle. La nature des singularités de la densité d'états (et leur comportement logarithmique) a été mise en évidence. Les premières corrections de taille finie ont également été calculées. Les valeurs moyennes d'observables ont été étudiées, toujours dans la limite semi-classique. Enfin nous avons pu déduire une relation entre les éléments de matrice des observables, calculés entre états propres du Hamiltonien, avec les coefficients de Fourier de l'observable classique, sur la trajectoire classique.

Près des singularités, la quantification de Bohr-Sommerfeld, adaptée aux spins, n'est pas valable, car elle s'appuie sur une approximation du type WKB qui diverge près des points hyperboliques caractérisant ces orbites critiques. Pour traiter ces cas, nous avons développé une nouvelle approche, en analogie avec celle déjà connue pour la représentation de Schrödinger, permettant alors d'obtenir les valeurs propres dans ce voisinage des points critiques. Les propriétés physiques des état propres ont aussi été étudiées, par la caractérisation des éléments de matrice des observables entre états d'énergie proche de l'énergie critique.

Chapter 1

Introduction

1.1 Quantum Phase Transitions

Phase transitions are among the most important physical phenomena, and have been the subject of decades of experimental and theoretical studies. They occur whenever a minute variation of an external control parameter (like temperature or pression) imposed on a physical system leads to a qualitative change in its properties, as seen for example in the behaviour of appropriate order parameters. Classical phase transitions are analysed in terms of a subtle competition between energy and entropy contributions, and a prominant role is played by thermal fluctuations. Exact solutions, within the statistical thermodynamics framework, of simple models exhibiting phase transitions (like the celebrated 2-dimensional Ising model), paved the route for very rich and deep later theoretical investigations. In particular, universal properties characterising the vicinity of the transition where understood within the renormalisation group analysis.

In more recent years, a strong emphasis has been put on a related kind of phenomena, the quantum phase transitions (QPT)[1]. They occur at zero temperature when there are qualitative changes in the ground state of the system, induced by a variation of the coupling constants in the Hamiltonian. Here, the transitions are driven by quantum fluctuations, and the ground state changes translate into singular behaviour of order parameters defined as observables expectation values. As in the classical case, one defines the order of a quantum phase transition in relation to the nature of the non-analytical behaviour of the order parameter. A discontinuous order parameter characterizes a first order QPT, while a continuous order parameter with a discontinuous first order derivative signals a second order QPT, and so on. Here also, the critical behaviour of correlation functions can be focused on, instead of an order parameter analysis.

At a generic first order QPT point, the gap between the two lowest energy states goes to zero exponentially as the size of the system increases. Whenever a correlation length can be defined, it also presents a singular behaviour, with exponentially fast varying spatial correlations. At second order QPT points, universal scaling behaviors are observed. The energy gap between the two lowest energy states, as well as spatial correlations, show algebraic behaviour with the system size. The latter QPT belong to separate universality

classes, characterised by sets of shared exponents. Even quantum state entanglement is believed to be strongly sensitive to the proximity of the QPT. Typical examples of QPT are found in many fields in physics, like nuclear physics [2, 3, 4, 5], describing transitions of shape, geometry and magnetic properties of nuclei, atomic physics [6, 7, 8] or condensed matter systems [9, 1]

More recently, singular behaviours not limited to the ground state, and therefore arising throughout the excitation spectrum of certain many-body models, have been under focus [10, 11, 12, 13, 14]. We shall discuss such cases in the present work, in the context of collective spin systems.

1.2 Quantum Spin Systems

There are many examples such that the main physical properties of a given system can be written in terms of collective spin or pseudospin variables. They arise naturally in the study of mutually interacting two-level systems, or due to symmetries present in collective bosonic Hamiltonians [15, 16]. Examples are found in nuclear [17, 2, 5], atomic [6, 7, 8] and molecular physics [18]. A typical example is given by the the Lipkin-Meshkov-Glick (LMG) model proposed in 1965 to describe shape phase transition in nuclei [17]. This model is used to describe magnetic properties of molecules [18], interacting bosons in double-well structures [15, 16] and to investigate the role of entanglement in quantum phase transitions (QPT) [19, 20]. This model presents a second-order quantum phase transition. It can be viewed directly as a large spin system, or equivalently as a system formed by a n interacting spins 1/2, splitted into total spin representations, with a particular focus on a restriction to the symmetric sector.

For such models, the analog of the semi-classical limit is obtained when the number of interacting sub-systems increases (thermodynamic limit) [21, 22]. The semi-classical parameter $\hbar$ is replaced by the the inverse of number of interacting sub-systems n^{-1} which is related to the size of the considered $su(2)$ representation, $n = 2s$.

$su(2)$-coherent states [23, 24] prove to be very useful in the treament of collective spin models. They also allow for a simple presentation for the Majorana representation [25], a very elegant approach to display the (generic) spin geometry. Analytic properties [26] of the wave function, in the coherent state representation, permits to obtain the quantization conditions. In the WKB framework, for regular orbits, i.e. away from critical energies where the classical orbit is given by a separatrix, this approach leads to the Bohr-Sommerfeld (B-S) quantization for spin systems [21, 27], also derived in a path integral formalism [28].

Due to the simplicity of the $su(2)$ algebra, with Cartan subalgebra of dimension 1, this type of models is completely integrable, in the sense that is possible to give a set

of explicit algebraic relations characterizing the eigenstates and eigenvalues of a given Hamiltonian. This relations are simply obtained in the coherent state representation. In this representation, the wave function is given as a polynomial of order n and can be completely characterized, up to a non-physical constant, by the set of its zeros. It is possible to give an explicit, but in general quite complicated, algebraic relation for the set of zeros corresponding to the Hamiltonian eigenstates.

In this work, we study into details the LMG model, in the thermodynamic limit, and then along finite size corrections. First, a mean field analysis is done, relating singular classical orbits with singularities arising within the spectum. This allows us to characterize different regions in the parameter space of the model, with respect of their qualitative spectral differences. The analysis of the structure of the zeros of the Majorana polynomial (associated to the eigenstates) permits to derive the exact integrated density of states in the thermodynamic limit. A rather precise study of the spectral singularities, location and non-analytic behavior, is proposed. We also address the behavior of matrix elements of generic observables in the eigenstates basis and relate them to the Fourier coefficients of the (equivalent) classical observables, obtained by integrating the flow equations.

We finally analyse, in a semi-classical framework, the set of classical trajectory separatrix, and their associated stationary hyperbolic points (HP). The regular Bohr-Sommerfeld quantization conditions have to be modified for energies of order n^{-1} around the critical energy. Orbits passing thought a HP signal a qualitative change in the classical orbits topology. Quantization for this kind of orbits were obtained in the Schrödinger representation for a particle in an anharmonic potential [29, 30, 31, 32]. Here, we propose an equivalent treatment adapted for the (coherent) spin case, which permits in particular to obtain the eigenvalues at energies located near the semi-classical separatix. We then go further, and analyse the behaviour of observable matrix elements near the separatrix, a point which will be useful in the second part of this thesis.

Chapter 2

Semi-classical Limit for Spin Systems

2.1 Coherent States for Spin Systems

2.1.1 Coherent States - A brief introduction

Coherent states (CS) representations are as old as quantum mechanics, even though not named as such. Indeed, already in 1926, Schrödinger used sets of non-orthogonal wave functions to describe non-spreading wave packets for quantum harmonic oscillators. They provided the first example of quantum states whose dynamics satisfy on aspect of the correspondence principle, i.e. the quantum dynamics tends to the classical one in the limit $\hbar \to 0$. In the sixties, these types of states regain much attention [33, 34], in particular following the work of Glauber, who showed in 1963 that they provide a good description of the electromagnetic field [34]. Note that a particular feature of coherent states, that they form an overcomplete basis, present number of advantages compared with a usual orthogonal basis. Since the seminal works of Glauber, CS have pervaded almost all areas of quantum physics, and are very useful in the context of semi-classical analysis.

The first CS, as introduced by Schrödinger, are related to the so-called Heisenberg-Weyl group, the group obtained by exponentiating the operators $\{1, a, a^\dagger, a^\dagger a\}$. Recall that the CS are eigenstates of the annihilation operator a. Whenever the Hamiltonian of a system is written within the algebra formed by this set of operators, i.e. can be written as a sum of such operators, the Weyl group is said to be the dynamical symmetry group of the system. In particular, under time evolution, a coherent state remains coherent, which permits a simplified analysis of the dynamics in terms of the one associated with the related classical problem.

The generalization of coherent states for systems whose dynamical symmetry group is an arbitrary Lie group was introduced independently by Perelomov and Gilmore [35, 36, 37]. The parametrization of CS permits to characterize the phase space of the associated classical system, and therefore to address the semi-classical limit. Beside the important cases covered by the Weyl group, a similar analysis is clearly very interesting for spin systems. Spin coherent states (SCS) have been introduced to cover this case, associated with an $SU(2)$ dynamical group. They are now presented.

2.1.2 Spin Coherent States

In this section we review the spin coherent states [23, 24], associated with the $SU(2)$ group.

Let us denote by $\{|s,m\rangle\}$ the standard eigenbasis of $\left\{\mathbf{S}^2, S_z\right\}$ with eigenvalues $s(s+1)$ and m respectively. For fixed s these states span a $2s+1$ dimensional space in which the generators of the $su(2)$ algebra act irreducibly. For such an irreducible representation we define the unnormalized spin coherent-state $|\alpha\rangle$ as

$$|\alpha\rangle = e^{\alpha S_+}|s,-s\rangle. \tag{2.1}$$

The scalar product of two such states can be obtained from the commutation relations of the $su(2)$ algebra, considering the Baker-Campbell-Hausdorff formulas for $su(2)$ (see [37]) also called gaussian decomposition formulas [23], and reads

$$\langle\alpha'|\alpha\rangle = (1+\bar{\alpha'}\alpha)^{2s}, \tag{2.2}$$

where $\bar{\alpha}$ is the complex conjugate of α. These coherent states obey the following closure relation:

$$\int \mathrm{d}\mu(\bar{\alpha},\alpha)\frac{|\alpha\rangle\langle\alpha|}{\langle\alpha|\alpha\rangle} = 1, \tag{2.3}$$

where

$$\mathrm{d}\mu(\bar{\alpha},\alpha) = \frac{n+1}{(1+\bar{\alpha}\alpha)^2}\frac{\mathrm{dRe}(\alpha)\ \mathrm{dIm}(\alpha)}{\pi}, \tag{2.4}$$

and $n = 2s$.

In this representation, a quantum state $\Psi(\bar{\alpha}) = \langle\alpha|\Psi\rangle$ is a polynomial in $\bar{\alpha}$, and the action of the spin operators on Ψ translates into differential operators:

$$S_+ = 2s\bar{\alpha} - \bar{\alpha}^2\partial_{\bar{\alpha}}, \tag{2.5}$$
$$S_- = \partial_{\bar{\alpha}}, \tag{2.6}$$
$$S_z = -s + \bar{\alpha}\partial_{\bar{\alpha}}, \tag{2.7}$$

where $S_\pm = S_x \pm \mathrm{i}S_y$. These relations can be obtained using Eq. (2.1) together with the $su(2)$ commutation relations

$$[S_+, S_-] = 2S_z, \tag{2.8}$$
$$[S_z, S_\pm] = \pm S_\pm. \tag{2.9}$$

We now discuss the representation of $\Psi(\bar{\alpha})$ in terms of its zeroes (the Majorana representation).

2.1.3 Majorana Polynomial and Majorana Sphere

Any $|\Psi\rangle$ can be represented by its Majorana polynomial [25] defined as

$$\Psi(\bar{\alpha}) = \langle\alpha|\Psi\rangle = \sum_{m=-s}^{s} \sqrt{\frac{(2s)!}{(s-m)!(m+s)!}} \langle s,m|\Psi\rangle \bar{\alpha}^{m+s}, \tag{2.10}$$

$$= C \prod_{k=1}^{d} (\bar{\alpha} - \bar{\alpha}_k), \tag{2.11}$$

where $d \leqslant 2s$ is the degree of this polynomial in $\bar{\alpha}$ ($d = 2s$ for a generic state). The roots $\bar{\alpha}_k$ of $\Psi(\bar{\alpha})$ fully characterize a quantum state $|\Psi\rangle$ up to a global unphysical constant.

It is also possible to represent such a state $|\Psi\rangle$ on the so-called Majorana sphere, which can be seen as a generalization of the celebrated Bloch sphere used for spin $\frac{1}{2}$ states. To do so, one first complement the d roots $\Psi(\bar{\alpha})$ with $(2s-d)$ roots at infinity in the complex plane. Next, the resulting set of $2s$ complex numbers $\bar{\alpha}_k$ is mapped onto $2s$ points on the unit sphere by an inverse stereographic map: $\Pi^{-1}(\xi) = (1+|\xi|^2)^{-1}\{2\mathrm{Re}(\xi), 2\mathrm{Im}(\xi), |\xi|^2 - 1\}$ for $\xi \in \mathbb{C}$. For instance, the basis states $|s,m\rangle$ are represented by $(s-m)$ points on the north pole and $(s+m)$ points on the south pole (Fig. 2.1). Less trivial examples can be found in Fig. 2.1-(b,c) for an eigenstate of a quadratic Hamiltonian and for a random state, respectively.

Another, perhaps more physical, way of motivating the use of the Majorana polynomial is to consider the spin s system as the symmetric sector of a collection of n spins $1/2$, each of them characterized by an unnormalized wave function of the form $|\psi_i\rangle = -\bar{\alpha}_i|1/2,-1/2\rangle + |1/2,1/2\rangle$. To each such function, it corresponds an (order one) Majorana polynomial which simply writes $\langle\alpha|\psi_i\rangle = \bar{\alpha} - \bar{\alpha}_i$, where the inverse stereographic projection of $\bar{\alpha}_i$ is the antipode on the Riemann sphere of the standard Bloch representation. Let $\mathbb{P}_n$ be the projector onto the symmetric sector, for $n = 2$

$$\mathbb{P}_2 = \frac{1}{2}(1 + \mathcal{P}_{1,2}) \tag{2.12}$$

with $\mathcal{P}_{i,j} = \frac{1}{2}(1 + \boldsymbol{\sigma}^{(i)}.\boldsymbol{\sigma}^{(j)})$ the operator permuting spin i and j and σ_i the Pauli matrices defined as

$$\sigma_x = \begin{pmatrix} 0 & 1 \\ 1 & 0 \end{pmatrix}; \quad \sigma_y = \begin{pmatrix} 0 & -\mathrm{i} \\ \mathrm{i} & 0 \end{pmatrix}; \quad \sigma_z = \begin{pmatrix} 1 & 0 \\ 0 & -1 \end{pmatrix}. \tag{2.13}$$

For a general n we have

$$\mathbb{P}_n = \prod_{i<j} \frac{1}{2}(1 + \mathcal{P}_{i,j}). \tag{2.14}$$

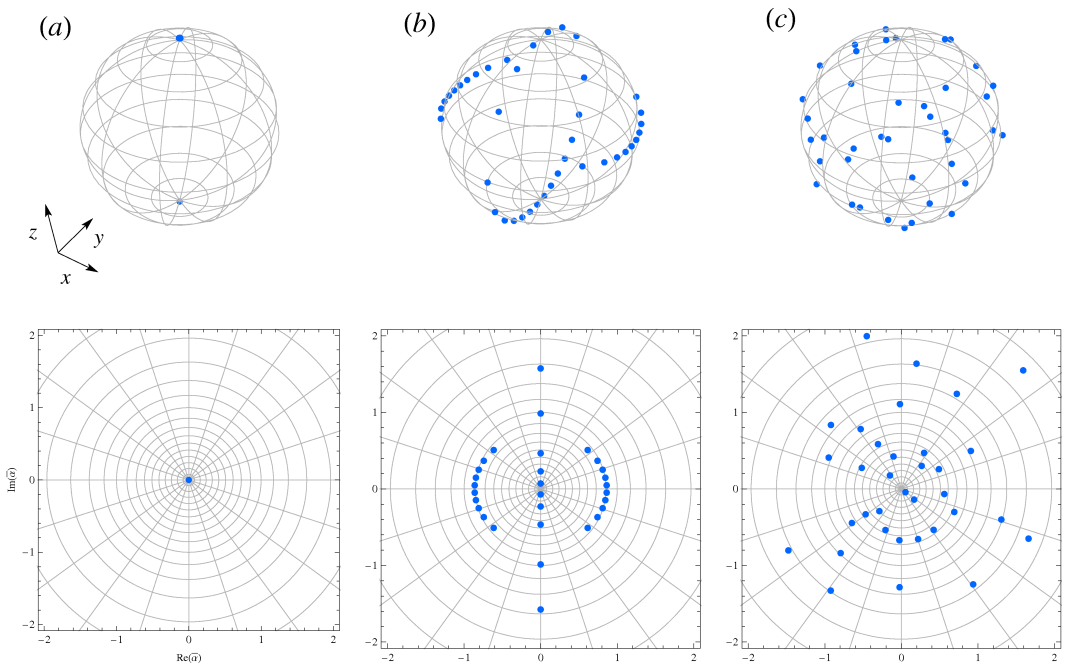

Figure 2.1: Zeros of the Majorana polynomial represented in the Riemann Sphere and in the complex plane for $s = 20$. (a) $|s, m\rangle$ having $(s - m)$ points on the north pole and $(s + m)$ points on the south pole; (b) eigenstate of a quadratic Hamiltonian having the zeroes aligned along lines; (c) Random state.

The tensor product of a collection of n spin-1/2 states projected onto the symmetric sector has a well defined total spin $s = n/2$, the zeros of the Majorana polynomial of this composite symmetric state are given by the set of zeros of the spin 1/2 polynomials, as can be seen easily from

$$|\alpha_s\rangle = \bigotimes_{i=1}^{n} |\alpha_{s=1/2}\rangle, \tag{2.15}$$

and so

$$\langle \alpha_s | \Psi_s \rangle = \langle \alpha_s | \mathbb{P}_n \left(\bigotimes_{i=1}^{n} |\psi_i\rangle \right) = C \prod_{i=1}^{n} (\bar{\alpha} - \bar{\alpha}_i) \,. \tag{2.16}$$

The Majorana representation is thus the generalization of the Bloch sphere for a symmetrized set of two level systems.

Let us also introduce $G(\bar{\alpha})$, the logarithmic derivative of $\Psi(\bar{\alpha})$,

$$G(\bar{\alpha}) = \frac{1}{n} \partial_{\bar{\alpha}} \ln \Psi(\bar{\alpha}) = \frac{1}{n} \sum_{k=1}^{n} \frac{1}{\bar{\alpha} - \bar{\alpha}_k}, \tag{2.17}$$

having simple poles, with residue $1/n$, at the zeros of the Majorana polynomial and $\Omega(\bar{\alpha}, \alpha)$, the logarithm of the inner product of coherent states,

$$\Omega(\bar{\alpha}, \alpha) = \frac{1}{n} \ln\langle\alpha|\alpha\rangle = \ln(1 + \bar{\alpha}\alpha). \tag{2.18}$$

The $1/n$ factor is here to ensure that G and Ω are well behaved at the (infinite n) thermodynamic limit. Using the $G(\bar{\alpha})$, a state $|\Psi\rangle$, writes in the coherent state basis:

$$\Psi(\bar{\alpha}) = \mathrm{e}^{n \int_{\bar{\alpha}_0}^{\bar{\alpha}} \mathrm{d}\bar{\alpha}' G(\bar{\alpha}')} \tag{2.19}$$

where the normalization is taken such that $\Psi(\bar{\alpha}_0) = \langle\alpha_0|\Psi\rangle = 1$.

2.1.4 Operators in the CS Basis

We consider operators that, in the coherent state basis, can be written as

$$\hat{A} = \sum_{i=0}^{n} p_i(\bar{\alpha}) \frac{1}{n^i} \partial_{\bar{\alpha}}^i, \tag{2.20}$$

where the p_i's are polynomial functions of $\bar{\alpha}$. This is a quite general family of operators, in particular all reasonable physical quantities are of this form. Indeed, the $su(2)$ generators Eq. (2.5,2.6,2.7) and their positive powers can be written in this way. To each operator we can associate several functions of two variables, referred in the literature as the "symbols of the operator" [23]. We define two such functions. $\mathcal{A}$ which is defined such that

$$\hat{A} = \mathcal{A}(\bar{\alpha}, n^{-1}\partial_{\bar{\alpha}}) \tag{2.21}$$

and, by (2.20), is given explicitly as

$$\mathcal{A}(\bar{\alpha}, \zeta) = \sum_{i=0}^{n} p_i(\bar{\alpha}) \zeta^i. \tag{2.22}$$

And A, defined as the normalized matrix element of the operator $\hat{A}$ between two coherent states

$$\mathrm{A}(\bar{\alpha}, \alpha) = \frac{\langle\alpha|\hat{A}|\alpha\rangle}{\langle\alpha|\alpha\rangle}. \tag{2.23}$$

For the set of considered operators, it is possible to give an explicit algebraic relation between A and $\mathcal{A}$; this is done perturbatively in n^{-1} in section A.1.2.

2.1.5 Generalized Husimi Function

The Husimi function is defined as the probability of finding a state Ψ in a CS $|\langle\alpha|\Psi\rangle|^2\langle\alpha|\alpha\rangle^{-1}$. It was introduced by Husimi for the Heisenberg-Weyl group [38] and extended for general Lie groups [39] in order to study eigenstates of chaotic Hamiltonians [39, 40].

We define the generalized Husimi function associated with two general states $|\Psi\rangle$ and $|\Phi\rangle$ as,

$$W_{\Psi,\Phi}(\bar{\alpha},\alpha) = \frac{\langle\Psi|\alpha\rangle\langle\alpha|\Phi\rangle}{\langle\alpha|\alpha\rangle} = \mathrm{e}^{nS_{\Psi,\Phi}(\bar{\alpha},\alpha)}, \tag{2.24}$$

with

$$S_{\Psi,\Phi}(\bar{\alpha},\alpha) = \int_{\bar{\alpha}_\Phi}^{\bar{\alpha}} G_\Phi(\bar{\alpha}')\mathrm{d}\bar{\alpha}' + \int_{\alpha_\Psi}^{\alpha} \bar{G}_\Psi(\alpha')d\alpha' - \Omega(\bar{\alpha},\alpha), \tag{2.25}$$

with G defined in the last section and states α_Φ and α_Ψ defined such that $\langle\alpha_\Phi|\Phi\rangle = \langle\Psi|\alpha_\Psi\rangle = 1$.

Using the closure relation given in Eq. (2.3), matrix elements of an operator $\hat{A}$ can be computed with the help of the Husimi function

$$\begin{aligned}
\langle\Psi|\hat{A}|\Phi\rangle &= \int \mathrm{d}\mu(\bar{\alpha},\alpha)\frac{\langle\Psi|\alpha\rangle\langle\alpha|\hat{A}|\Phi\rangle}{\langle\alpha|\alpha\rangle}, &(2.26)\\
&= \int d\mu(\bar{\alpha},\alpha)\; W_{\Psi,\Phi}(\bar{\alpha},\alpha)\; \mathcal{A}[\bar{\alpha}, n^{-1}\partial_{\bar{\alpha}} + G_\Phi(\bar{\alpha})], &(2.27)
\end{aligned}$$

where $\mathcal{A}[\bar{\alpha}, n^{-1}\partial_{\bar{\alpha}} + G_\Phi(\bar{\alpha})] = \langle\alpha|\Phi\rangle^{-1}\hat{A}\langle\alpha|\Phi\rangle$.

We now consider maximal sets of the generalized Husimi function, the extremal conditions being given by

$$\begin{aligned}
\partial_\alpha S_{\Psi,\Phi}(\bar{\alpha},\alpha) &= \bar{G}_\Phi(\alpha) - \partial_\alpha\Omega(\bar{\alpha},\alpha) = 0, &(2.28)\\
\partial_{\bar{\alpha}} S_{\Psi,\Phi}(\bar{\alpha},\alpha) &= G_\Psi(\bar{\alpha}) - \partial_{\bar{\alpha}}\Omega(\bar{\alpha},\alpha) = 0. &(2.29)
\end{aligned}$$

As we shall see below, these conditions imposed together with having Ψ and Φ as eigenstates of an Hamiltonian, will permit to compute matrix elemens of observables in the semi-classical limit. Moreover we shall also see that for $\Psi = \Phi$ the Husimi function is exponentially localized around semi-classical orbits, which are the level sets of the classical energy surface.

2.2 WKB method and Bohr-Sommerfeld Quantization for Spin Systems

The WKB, BWK, WBK, BWKJ, ..., method approximates a real Schrödinger wave function by a sinusoidal oscillation whose phase is given by the space integral of the classical momentum. The method was introduced independentely in 1926 by G. Wentzel [41] and L. Brillouin [42], and improved by H. A. Kramers [43] few months later. In these early days of quantum theory, problems such as the tunnelling phenomenon through a potential barrier, energy eigenstates in a potential well, among many others, required to solve differential equations which, in general, and even in one dimension, have no analytic solutions. Approximating the wave function by an oscillatory wave depending on a phase integral proved very useful in providing physical intuition, and qualitative and quantitative solutions.

The original formulation of the Schrödinger equation was given in the space of positions, the so-called Schödinger representation, where functions of the operator $\hat{x}$ are diagonal. In this representation, the WKB approach in not always simple, due to the existence of caustics, and matching formulas are needed. The phase-space representation, introduced by Bargmann [44], wich is equivalent to the coherent state representation for the Heisenberg-Weyl group, was recognised to have many advantages [26] when combined with WKB methods. In particular the quantization rules follow simply from imposing analicity to the eigenfunctions [26, 21].

We present here a derivation of the WKB approximation for a spin system using $n^{-1} = (2s)^{-1}$ as the semi-classical parameter. We also obtain the Bohr-Sommerfeld quantization based on the analiticity of the WKB function along the classical trajectory.

2.2.1 WKB Wave Function

In this section we give the WKB approximation of the eigenstates of a hermitian operator H. This is done by developing the involved quantities in powers of n^{-1}.

Let us first write the time-independent Schrödinger equation $\hat{H}|\Psi\rangle = \varepsilon|\Psi\rangle$ in the coherent-state representation. Note that for sake of simplicity we take $n\hat{H}$ and not $\hat{H}$ to be an extensive operator. Using Eq. (2.19), one transforms the Schrödinger equation into a non-linear differential equation for its logarithmic derivative $G(\bar{\alpha})$, which satisfies the following Riccati-like equation

$$\mathcal{H}\left[\bar{\alpha}, n^{-1}\partial_{\bar{\alpha}} + G(\bar{\alpha})\right] = \varepsilon. \tag{2.30}$$

We suppose that all involved quantities admit a n^{-1} development:

$$\mathcal{H} = \sum_{i=0}^{\infty} n^{-i}\mathcal{H}_i \; ; \quad G = \sum_{i=0}^{\infty} n^{-i}G_i \; ; \quad \varepsilon = \sum_{i=0}^{\infty} n^{-i}\varepsilon_i. \tag{2.31}$$

$\mathcal{H}_0$ is, sometimes, called the principal symbol of the operator $\hat{H}$ and $\mathcal{H}_{i>0}$ its sub-symbols.

The perturbative expansion in powers of n^{-1} permits, after some algebraic manipulations (see section A.1.1), to obtain a hierarchy of equations for the G_i's. For computing the wave function at leading order we give explicitely the relations for both the leading G_0 and the next to leading G_1, orders

$$\varepsilon_0 = \mathcal{H}_0\left(\bar{\alpha}, G_0\right), \tag{2.32}$$

$$\varepsilon_1 = \mathcal{H}_1\left(\bar{\alpha}, G_0\right) + \frac{\partial_{\bar{\alpha}} G_0}{2}\partial_\zeta^2 \mathcal{H}_0\left(\bar{\alpha}, G_0\right) + G_1 \partial_\zeta \mathcal{H}_0\left(\bar{\alpha}, G_0\right), \tag{2.33}$$

where $\partial_\zeta \mathcal{H}_0\left(\bar{\alpha}, G_0\right)$ is the derivative of the symbol $\mathcal{H}_0(\bar{\alpha}, \zeta)$ computed in $\zeta = G_0(\bar{\alpha})$. Simplifying the equation for G_1 we get

$$G_1(\bar{\alpha}) = -\frac{1}{2}\frac{\mathrm{d}}{\mathrm{d}\bar{\alpha}} \log\left[\partial_\zeta \mathcal{H}_0\left(\bar{\alpha}, G_0\right)\right] + \frac{\varepsilon_1 - \mathcal{H}_1\left(\bar{\alpha}, G_0\right) + \frac{1}{2}\partial_{\bar{\alpha}}\partial_\zeta \mathcal{H}_0\left(\bar{\alpha}, G_0\right)}{\partial_\zeta \mathcal{H}_0\left(\bar{\alpha}, G_0\right)}. \tag{2.34}$$

The WKB wave function then writes,

$$\begin{aligned} \langle \alpha | \Psi \rangle &= \mathrm{e}^{n\int_{\bar{\alpha}_0}^{\bar{\alpha}} \mathrm{d}\bar{\alpha}'\ G(\bar{\alpha}')} \\ &= \frac{\sqrt{\partial_\zeta \mathcal{H}_0\left(\bar{\alpha}, G_0\right)|_{\bar{\alpha}_0}}}{\sqrt{\partial_\zeta \mathcal{H}_0\left(\bar{\alpha}, G_0\right)|_{\bar{\alpha}}}} \mathrm{e}^{n\int_{\bar{\alpha}_0}^{\bar{\alpha}} \mathrm{d}\bar{\alpha}'\left[G_0 + \frac{1}{n}\frac{\varepsilon_1 - \mathcal{H}_1 + \frac{1}{2}\partial_{\bar{\alpha}}\partial_\zeta \mathcal{H}_0}{\partial_\zeta \mathcal{H}_0}\right]} [1 + O(n^{-1})], \end{aligned} \tag{2.35}$$

where G_0 is given by Eq. (2.32). The square root is defined as: $\sqrt{x} = e^{\frac{1}{2}\ln(x)}$, and the branch cut of the logarithm is taken to be the negative real axis.

2.2.2 Bohr-Sommerfeld Quantization

Quantization of the energies is obtained by imposing that $\Psi(\bar{\alpha})$ is a univaluated function of $\bar{\alpha} \in \mathbb{C}$. Writing the $\Psi(\bar{\alpha})$ as in Eq. (2.19) the wave function has to take the same value when evaluated along the two different paths of Fig. (2.2). In terms of G this translates to

$$\mathcal{I}_\gamma = -\frac{1}{2\pi \mathrm{i}} \oint_\gamma \mathrm{d}\bar{\alpha}\, G(\bar{\alpha}) = \frac{k}{n}, \tag{2.36}$$

with $k \in \mathbb{N}$ and for all closed paths γ.

We define $\mathcal{I}$ as being $\mathcal{I}_{\gamma=\mathcal{C}}$ where the curve $\mathcal{C}$ is defined such that the probability amplitude $W_{\Psi,\Psi}(\bar{\alpha}, \alpha)$ of finding the system in the coherent state $|\alpha\rangle$ is maximal, see Eq. (2.28, 2.29):

$$\mathcal{C} = \{\bar{\alpha} :\ \mathcal{H}\left[\bar{\alpha}, \partial_{\bar{\alpha}}\Omega(\bar{\alpha}, \alpha) + n^{-1}\partial_{\bar{\alpha}}\right] = \mathrm{H}\left(\bar{\alpha}, \alpha\right) = \varepsilon\}. \tag{2.37}$$

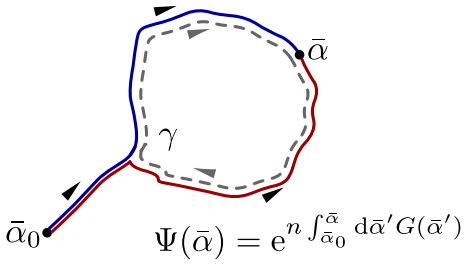

Figure 2.2: Quantization (2.36) derives from imposing that $\Psi(\bar{\alpha})$ be univaluated.

For this particular curve, one can see that $\mathcal{I}$ is given by the action of the classical flow with energy ε

$$\mathcal{I} = -\frac{1}{2\pi \mathrm{i}} \oint_{\mathcal{C}} \mathrm{d}\bar{\alpha}\, \partial_{\bar{\alpha}} \Omega(\bar{\alpha}, \alpha) = \frac{1}{2\pi} \int_{\Sigma} \omega, \tag{2.38}$$

obtained upon integrating the symplectic 2-form $\omega = \mathrm{i}\partial_{\bar{\alpha}}\partial_{\alpha}\Omega(\bar{\alpha}, \alpha)\mathrm{d}\alpha \wedge \mathrm{d}\bar{\alpha}$ (see section A.2.3) over the interior of the classical trajectory Σ.

In the semi-classical limit we define similarly the classical-orbit:

$$\mathcal{C}_0 = \{\bar{\alpha} :\ \mathcal{H}_0\left[\bar{\alpha}, \partial_{\bar{\alpha}}\Omega(\bar{\alpha}, \alpha)\right] = \mathrm{H}_0\left(\bar{\alpha}, \alpha\right) = \varepsilon_0\}. \tag{2.39}$$

The relation between $\mathcal{H}_0$ and H_0 is obtained in section A.1.2. If $\mathcal{C}_0$ contains no points such that $\partial_{\zeta}\mathcal{H}_0 = 0$, the WKB solution (2.35) is an analytic function of $\bar{\alpha}$ in the vicinity of $\mathcal{C}_0$. Hyperbolic points for which $\partial_{\zeta}\mathcal{H}_0 = 0$ are treated in chapter 5. In the regular case, Eq. (2.36) can be explicitly computed by choosing $\gamma = \mathcal{C}_0$ and using the semi-classical expansion of G. Expanding $\mathcal{I} = \sum_{i=0} n^{-i}\mathcal{I}_i$, one obtains the Bohr-Sommerfeld quantization condition

$$\mathcal{I}_0 + n^{-1}\mathcal{I}_1 + O(n^{-2}) = n^{-1}k, \tag{2.40}$$

where $\mathcal{I}_0$ is given by the classical action

$$\mathcal{I}_0 = -\frac{1}{2\pi \mathrm{i}} \oint_{\mathcal{C}_0} \mathrm{d}\bar{\alpha}\, \partial_{\bar{\alpha}} \Omega(\bar{\alpha}, \alpha) = \frac{1}{2\pi} \int_{\Sigma} \omega, \tag{2.41}$$

and

$$\mathcal{I}_1 = \frac{1}{2} - \frac{1}{2\pi \mathrm{i}} \oint_{\mathcal{C}_0} \mathrm{d}\bar{\alpha} \frac{\varepsilon_1 - \mathcal{H}_1 + \frac{1}{2}\partial_{\zeta}\partial_{\bar{\alpha}}\mathcal{H}_0}{\partial_{\zeta}\mathcal{H}_0}, \tag{2.42}$$

with the $1/2$ term coming from the square root branch cut of Eq. (2.35).
For spin systems $\omega = \mathrm{i}(1 + \bar{\alpha}\alpha)^{-2}\mathrm{d}\bar{\alpha} \wedge \mathrm{d}\alpha$ and $\mathcal{I}_0$ is the solid angle sustained by classical trajectory divided by 2π.

Chapter 3

The Lipkin-Meshkov-Glick Model

3.1 Introduction

The Lipkin-Meshkov-Glick (LMG) model was proposed in 1965 to describe shape phase transitions in nuclei [17, 45, 46]. This model is often used to describe the magnetic properties of molecules such as Mn_{12} acetate [18]. However, it also captures the physics of interacting bosons in a double-well-like structure [15, 16] and is thus relevant to (two-mode) Bose-Einstein condensates [6] as well as Josephson junctions. It has also been recently used in optical cavity quantum electrodynamics in its dissipative version [8, 47], for studying the decoherence of a single spin coupled to spin bath [48, 49] or quench dynamics [50]. Note also that, in recent years, the entanglement properties of its ground state [19, 20, 51, 52, 53, 54, 55, 56, 57] as well! as the finite-size behavior [58, 59, 12, 60] have focused much attention on this model.

An exact solution of this model has been derived [61, 62, 63] but it requires the solution of Bethe-like equations, which is more costly in terms of computational effort than exact diagonalization. Although the low-energy physics of the model has been widely studied through different approaches (variational [17, 64, 65], bosonization [58, 66, 67], and coherent states [68, 67]), its high-energy properties have only been very recently investigated numerically [11, 69, 70] and several interesting features have been revealed. More precisely, for special values of the energy, the spectrum has been shown to display singularities which are reminiscent of the critical point responsible for the well-known quantum phase transition at zero temperature.

Note that along this chapter we use the total spin s as the expansion parameter instead of $n = 2s$, and some care should then be taken when identifying with the notation taken in the previous chapter.

3.2 The Lipkin-Meshkov-Glick model

The LMG model describes a set of n spins $\frac{1}{2}$ particles mutually interacting through an (anistropic) XY-like Hamiltonian and coupled to an external transverse magnetic field h. The Hamiltonian of this system can be expressed in terms of the total spin operators

$S_\alpha = \sum_{i=1}^{n} \sigma_\alpha^i/2$ where the σ_α's are the Pauli matrices:

$$H = -\frac{1}{n}\left(\gamma_x S_x^2 + \gamma_y S_y^2\right) - h\, S_z. \tag{3.1}$$

In the following, for simplicity, we only consider the maximum spin sector $s = n/2$ with N even. Given the symmetry of the spectrum of H, we focus on the parameter range $h \geqslant 0$; $|\gamma_y| \leqslant \gamma_x$. Note also that $\left[H, \mathbf{S}^2\right] = 0$ and $\left[H, \mathrm{e}^{\mathrm{i}\pi(S_z - s)}\right] = 0$ (spin-flip symmetry). In the standard eigenbasis $\{|s, m\rangle\}$ of $\mathbf{S}^2$ and S_z, this latter symmetry implies that odd and even m states decouple. In the thermodynamic limit, both subspaces are isospectral so that we further limit the following analysis to the $(s+1)$-dimensional sector with m even. It is known that H exhibits a quantum phase transition for $h = \gamma_x$ or $h = \gamma_y$.

3.3 Classical-energy surface

In the thermodynamic limit, a variational description of the ground state [17, 64, 65], built with respect to the $|\alpha\rangle$ states, leads to the dominant behaviour of the model and, in particular, the location of the quantum phase transition. The latter can be obtained from an analysis of the minima of the variational energy H_0:

$$\mathrm{H}_0(\bar{\alpha}, \alpha) \;=\; \lim_{s\to\infty} \frac{1}{s}\frac{\langle\alpha|H|\alpha\rangle}{\langle\alpha|\alpha\rangle} = \frac{2\left(1 - \alpha^2\bar{\alpha}^2\right)h - \left(\alpha + \bar{\alpha}\right)^2\gamma_x + \left(\alpha - \bar{\alpha}\right)^2\gamma_y}{2\left(1 + \alpha\bar{\alpha}\right)^2}. \tag{3.2}$$

Note that, in this limit, a classical spin description is valid, such that the correspondence between a state $|\alpha\rangle$ and a classical vector is simply obtained via a stereographic map from the complex plane onto the $\mathcal{S}^2$ sphere [with $\alpha = \mathrm{e}^{\mathrm{i}\theta}\tan(\phi/2)$], leading to the following parametrization

$$\mathbf{S} = \frac{n}{2}(\sin\theta\cos\phi, \sin\theta\sin\phi, \cos\theta). \tag{3.3}$$

Here we shall first be interested in the geometrical properties of the whole classical energy surface $\mathrm{H}_0(\bar{\alpha}, \alpha)$. Its extrema, obtained by imposing $\partial_{\bar{\alpha}}\mathrm{H}_0 = \partial_\alpha \mathrm{H}_0 = 0$, are given in Table 3.1 together with the corresponding energy. When one further imposes that α and $\bar{\alpha}$ are complex conjugate, the configuration space (spanned by the Hamiltonian parameters) is split into distinct regions characterized by the number of extrema and saddle points in $\mathrm{H}_0(\bar{\alpha}, \alpha)$.

This phase diagram coincides with that derived from the analysis of density of states singularities, as done in the next section. We shall describe below how far the classical analysis can help in understanding the spectral results. Note that a related analysis of the classical energy surface, including comparisons to numerically derived spectra, has already been proposed by Castaños *et al.* [70] in terms of the (θ, ϕ) angles instead of the present $(\bar{\alpha}, \alpha)$.

α	$\bar{\alpha}$	H_0
0	0	h
$-\left(\frac{-h-\gamma_x}{h-\gamma_x}\right)^{1/2}$	$-\left(\frac{-h-\gamma_x}{h-\gamma_x}\right)^{1/2}$	$-\frac{h^2+\gamma_x^2}{2\gamma_x}$
$\left(\frac{-h-\gamma_x}{h-\gamma_x}\right)^{1/2}$	$\left(\frac{-h-\gamma_x}{h-\gamma_x}\right)^{1/2}$	$-\frac{h^2+\gamma_x^2}{2\gamma_x}$
$-\left(\frac{h+\gamma_y}{h-\gamma_y}\right)^{1/2}$	$\left(\frac{h+\gamma_y}{h-\gamma_y}\right)^{1/2}$	$-\frac{h^2+\gamma_y^2}{2\gamma_y}$
$\left(\frac{h+\gamma_y}{h-\gamma_y}\right)^{1/2}$	$-\left(\frac{h+\gamma_y}{h-\gamma_y}\right)^{1/2}$	$-\frac{h^2+\gamma_y^2}{2\gamma_y}$
∞	∞	$-h$

Table 3.1: Extrema of the energy surface H_0.

3.3.1 Classical description of the phase diagram

The zero-temperature phase diagram of the LMG model is usually discussed in terms of its ground-state properties. In this case, only two phases are distinguished [17, 65, 59]. For $h > \gamma_x$ (symmetric phase), the ground state is unique and $\lim_{s\to\infty} \langle S_z \rangle / s = 1$, whereas for $h < \gamma_x$ (broken phase), the ground state is two-fold degenerate and $\lim_{s\to\infty} \langle S_z \rangle / s = h/\gamma_x$. Note that the degeneracy in the broken phase arises only in the thermodynamic limit, where the gap between the ground and first excited states vanishes exponentially with s. The quantum phase transition at $h = \gamma_x$ is of second order and characterized by mean-field critical exponents [65] as well as nontrivial finite-size scaling behavior [58, 59, 12].

We have shown [14, 71] that, when considering the full spectrum, four different zones arise instead of two, corresponding to a splitting of the broken phase region into three distinct parts characterized by different singularities in the density of states (see Fig. 3.1).

Note that such singularities have already been pointed out in the numerical study of the special case $\gamma_x = -\gamma_y$ [11, 69] and were called "exceptional points". We emphasize in the present study that *these exceptional points are associated with saddle points of the energy surface.* Of course, the absolute minimum (maximum) gives the lower (upper) bound of the spectrum. Note that these bounds may be degenerate.

In the thermodynamic limit, to a given energy in the spectrum corresponds a level set on $\mathrm{H}_0(\bar{\alpha}, \alpha)$. At that energy, the Husimi function local maxima are known to concentrate along this level set, which forms the classical orbit. Singularities of the surface (maxima, minima or saddle points) translate into singularities of the level sets (a main ingredient in Morse surface theory). This, in turn, affects the density of states computation, as illustrated in the next section, and explains why the singularities in the $\mathrm{H}_0(\bar{\alpha}, \alpha)$ surface and in the density of states are in close correspondance.

As an illustration, we display in Fig. 3.2 the classical-energy surface for ($\gamma_x = 5, \gamma_y =$

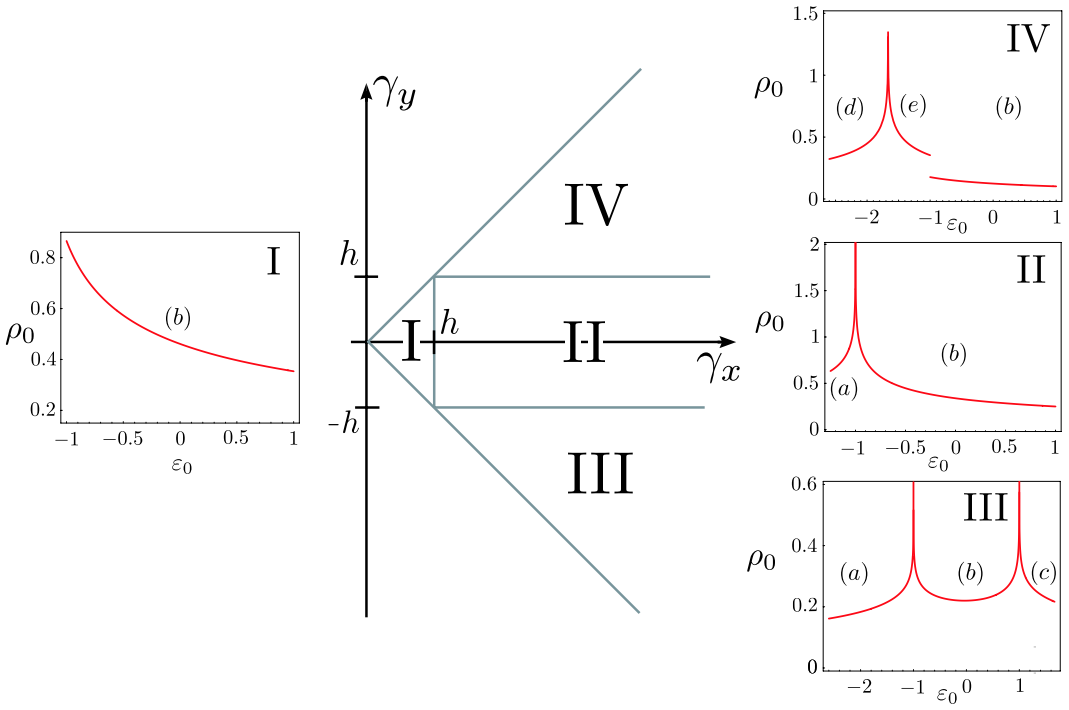

Figure 3.1: Phase diagram in the (γ_x, γ_y) plane at fixed $h > 0$ and typical density of states for (γ_x, γ_y, h) equal to I: (1/2, 1/3, 1), II: (2, 1/2, 1), III: (5, -3, 1), and IV: (5, 3, 1)

$3, h = -1$) which is precisely the point of zone IV whose density of states is shown in Fig. 3.1. As can be seen, the density of states contains two different types of singular points, being either the locus of a divergence or discontinuity. The analysis of the classical-energy surface allows one to qualitatively understand all these features. Indeed, it contains two absolute minima (noted m) which provide the lower bound of the spectrum (two-fold degenerate ground-state energy); two saddle points (noted s) corresponding to the singular behaviour of density of states; one local maximum (noted M) which is associated with the discontinuity, and one absolute maximum, not shown here, giving the upper bound of the spectrum.

The same geometrical analysis can be performed throughout the configuration space. A typical classical surface in zone I displays one minimum and one maximum, which respectively signal the lower and upper edges of the spectrum. A zone II surface has two absolute minima (corresponding to the broken phase degenerate ground states), a saddle point (corresponding to the density of states singularity), and one maximum (the upper spectrum edge). Finally, a generic zone III surface has (again) two absolute minima, two saddle points (corresponding to the two singularities in the spectrum, arising at different energies), and two absolute maxima (corresponding to a degenerate upper state). Note that, when displayed on the sphere, one recovers the standard result for surfaces singu-

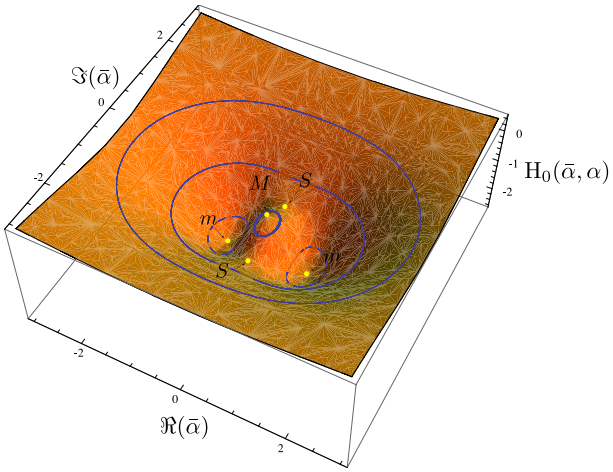

Figure 3.2: Typical classical-energy surface in zone IV ($\gamma_x = 5, \gamma_y = 3, h = -1$), containing several critical points: two minimal points (m); two saddle points (S); one local maximum (M). It also contains a global maximum, outside the range of this plot. The level curves of H_0 (classical trajectories) are plotted in blue.

larities, which states that the number of maxima plus the number of minima minus the number of saddle points equals the genus of the sphere, *i. e.*, 2.

Thus, the analysis of the classical-energy surface allows us to qualitatively describe the phase diagram shown in Fig. 3.1. However, it does not give any quantitative information concerning the density of states. The aim of what follows is to develop a reliable method to exactly compute the full spectrum of the LMG model.

3.4 Majorana representation and spectrum

3.4.1 From Schrödinger to Riccati

Let us now write the time-independent Schrödinger equation $H|\Psi\rangle = E|\Psi\rangle$ in the coherent-state representation. Using relations (2.5), (2.6), and (2.7), one transforms the Schrödinger equation into the following linear differential equation

$$\left[\frac{P_2(\bar{\alpha})}{(2s)^2}\partial_{\bar{\alpha}}^2 + \frac{P_1(\bar{\alpha})}{2s}\partial_{\bar{\alpha}} + P_0(\bar{\alpha})\right]\Psi(\bar{\alpha}) = \varepsilon\Psi(\bar{\alpha}), \tag{3.4}$$

where $\varepsilon = E/s$ and

$$P_0(\bar{\alpha}) = \frac{1}{4s}\Big[\bar{\alpha}^2(2s-1)(\gamma_y-\gamma_x)-\gamma_x-\gamma_y\Big]+h, \tag{3.5}$$

$$P_1(\bar{\alpha}) = \bar{\alpha}\Big\{\frac{2s-1}{2s}\Big[\alpha^2(\gamma_x-\gamma_y)-\gamma_x-\gamma_y\Big]-2h\Big\}, \tag{3.6}$$

$$P_2(\bar{\alpha}) = -\frac{1}{2}\left[\left(\bar{\alpha}^2-1\right)^2\gamma_x-\left(\bar{\alpha}^2+1\right)^2\gamma_y\right]. \tag{3.7}$$

The next step consists in converting the linear second-order differential equation (3.4) for Ψ into a nonlinear first-order differential equation for its logarithmic derivative $G(\alpha)$, which satisfies the following Riccati-like equation

$$P_2(\bar{\alpha})\left[\frac{G'(\bar{\alpha})}{2s}+G^2(\bar{\alpha})\right]+P_1(\bar{\alpha})G(\bar{\alpha})+P_0(\bar{\alpha})=\varepsilon. \tag{3.8}$$

3.4.2 Density of states and poles of G

The density of states is then obtained from the analysis of the poles of the function G. To illustrate the poles location, several typical states are displayed in Fig. 3.3 on the Majorana sphere. Each dot represents one pole of G, *i. e.*, one Majorana zero α_k, which is mapped from the complex plane to the sphere by an inverse stereographic projection

The cornerstone of this study is that, for the LMG model, the α_k's spread over two curves Γ_0 and Γ_1 in the complex plane. In addition, the n-th excited state of H has $2n$ poles on Γ_1 and $2(s-n)$ on Γ_0 (thus defining both curves). This remarkable property stems mainly from existing maps (which may differ between parameter space regions) between the LMG model and the problem of a particle in an effective one-dimensional potential (see Appendix A.3). In the latter case, the oscillation theorem indexes the excited states by the number of wavefunction nodes on the real axis. This leads here to (at least one set of) zeroes lying on simple lines in the complex plane, where the pole density varies monotoneously with energy.

Let us consider the normalized integrated density of states $\mathcal{N}(\varepsilon) \in [0,1]$. We shall enumerate by n the eigenstates of increasing energy, starting from $n=0$ for the ground state, to $n=s$ for the highest-energy state. The special location of the G poles leads to a simple relation between $\mathcal{N}(\varepsilon)$ and p, the number of poles lying in Γ_1, which reads

$$\mathcal{N}(\varepsilon) = \frac{n+1}{s+1} = \frac{1}{s+1}\left(1+\frac{p}{2}\right), \tag{3.9}$$

$$= \frac{1}{s+1}\left[1+\frac{s}{2\mathrm{i}\pi}\oint_{\widetilde{\Gamma}_1} G(\bar{\alpha})\,\mathrm{d}\bar{\alpha}\right], \tag{3.10}$$

where $\widetilde{\Gamma}_1$ is a contour that surrounds Γ_1 and oriented such that $\mathcal{N}\geq 0$, $\widetilde{\Gamma}_1$ is homotopic to the classical trajectory $\mathcal{C}_0$. For the sake of simplicity, we shall further consider the density

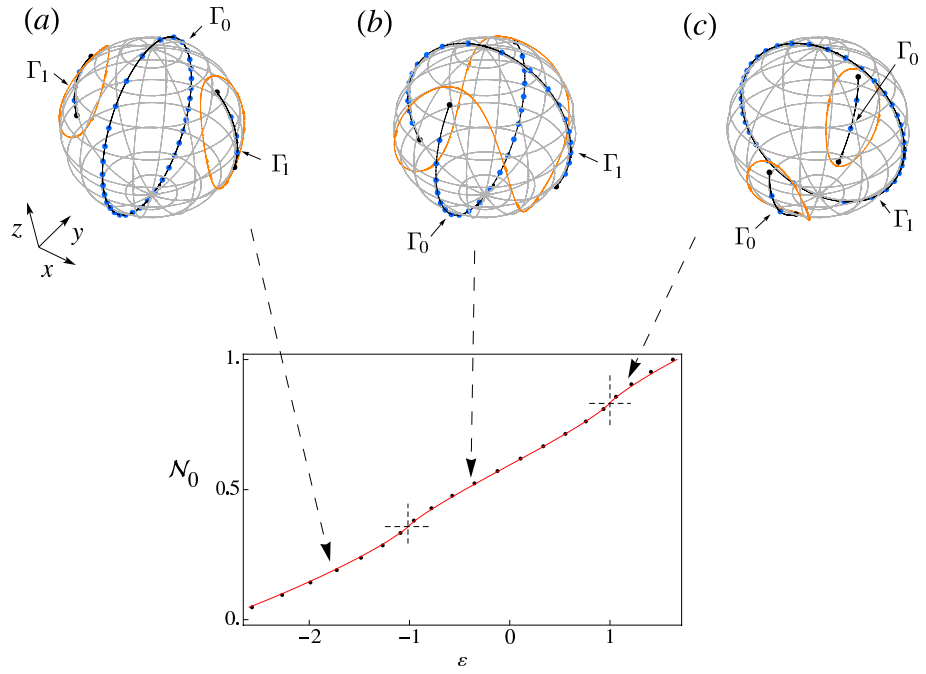

Figure 3.3: Upper part: representation of the poles of G on the Majorana sphere (blue dots) for three typical eigenstates computed for $h = 1, \gamma_x = 5, \gamma_y = -3$ and $s = 20$ (zone III in Fig. 3.1). Black lines correspond to the G_0 branch cuts Γ_0 and Γ_1, orange lines correspond to the classical orbits. Lower part: Numerical (black dots $s = 20$) versus analytical (red line $s = \infty$) integrated density of states. The two crosses indicate the singularities of the density of states $N_0^{\mathrm{III}}(-h)$ and $N_0^{\mathrm{III}}(h)$ [Eqs. (3.27) and (3.31) respectively] in the thermodynamic limit.

of poles in Γ_1, called $\mathcal{I} \in [0, 1]$, which simply reads

$$\mathcal{I}(\varepsilon) = \frac{p}{2s} = \frac{1}{2\mathrm{i}\pi} \oint_{\tilde{\Gamma}_1} G(\bar{\alpha})\, \mathrm{d}\bar{\alpha}, \tag{3.11}$$

In general, Eqs. (3.11) and (3.8) cannot be exactly solved for arbitrary s. The main goal of this paper is to solve these in the thermodynamic limit ($s \to \infty$) and to capture the leading finite-size corrections in a $1/s$ expansion.

3.4.3 Algebraic Relations for the Zeros of Eigenstates

Since the LMG Hamiltonian and collective spin Hamiltonian in general are integrable is possible to give a set of algebraic relations characterising the eigenstates. In order to do that let us consider Eq. (3.8) with $G(\bar{\alpha})$ given in (2.17)

$$\frac{P_2(\bar{\alpha})}{(2s)^2} \sum_{k \neq k'} \frac{1}{(\bar{\alpha} - \bar{\alpha}_k)(\bar{\alpha} - \bar{\alpha}_{k'})} + \frac{P_1(\bar{\alpha})}{2s} \sum_k \frac{1}{\bar{\alpha} - \bar{\alpha}_k} + P_0(\bar{\alpha}) = \varepsilon. \tag{3.12}$$

Generically $\bar{\alpha}_k \neq \bar{\alpha}_{k'}$ for $k \neq k'$ and the polynomials $P_i(\bar{\alpha}_k) \neq 0$, assuming these general hypothesis we can develop the above equation around a zero $\bar{\alpha}_i$ obtaining

$$\frac{1}{2s}\frac{1}{\bar{\alpha}-\bar{\alpha}_i}\left[2\frac{P_2(\bar{\alpha}_i)}{(2s)}Y_i(\bar{\alpha}_i)+P_1(\bar{\alpha}_i)\right]+$$
$$P_0(\bar{\alpha})-\varepsilon+\frac{1}{2s}\left[P_1(\bar{\alpha}_i)Y_i(\bar{\alpha}_i)+P_1'(\bar{\alpha}_i)\right]+\frac{1}{(2s)^2}Y_i(\bar{\alpha}_i)\left[P_2(\bar{\alpha}_i)Y_i(\bar{\alpha}_i)+2P_2'(\bar{\alpha}_i)\right]+O(\bar{\alpha}-\bar{\alpha}_i)=0 \tag{3.13}$$

with $Y_i(\bar{\alpha}_i)=\sum_{k\neq i}\frac{1}{(\bar{\alpha}_i-\bar{\alpha}_k)}$. The condition of cancelation of order $(\bar{\alpha}-\bar{\alpha}_i)^{-1}$ gives a set of $2s$ non-linear coupled equations verified by the zeros of an eigenstate of H

$$2\frac{P_2(\bar{\alpha}_i)}{(2s)}Y_i(\bar{\alpha}_i)+P_1(\bar{\alpha}_i)=0 \qquad i=1,...,2s. \tag{3.14}$$

These equations present at least as many as $2s+1$ sets of solution determining completely the eigenstates of the system. The energy of each state can be obtained considering the order $(\bar{\alpha}-\bar{\alpha}_i)^0$ in Eq. (3.13). Once the set of solutions is obtained by (3.14) the energy of the corresponding eigenstate is given as

$$\varepsilon=P_0(\bar{\alpha}_i)+\frac{1}{2s}\left[P_1(\bar{\alpha}_i)Y_i(\bar{\alpha}_i)+P_1'(\bar{\alpha}_i)\right]+\frac{1}{(2s)^2}Y_i(\bar{\alpha}_i)\left[P_2(\bar{\alpha}_i)Y_i(\bar{\alpha}_i)+2P_2'(\bar{\alpha}_i)\right]. \tag{3.15}$$

The existence of such set of equations is a characteristic of integrable systems; similar equations arise, for example, for the eigenstates of integrable one dimensional systems following the Bethe-ansatz procedure, or in matrix models.

3.5 The thermodynamic limit

3.5.1 Leading-order expansion for G

Let us assume that G, and ε, can be expanded in the form

$$G=\sum_{i\in\mathbb{N}}\frac{G_i}{s^i}, \quad \varepsilon=\sum_{i\in\mathbb{N}}\frac{\varepsilon_i}{s^i}. \tag{3.16}$$

At leading order $(1/s)^0$, Eq. (3.8) becomes a second-order polynomial equation for G_0 whose solutions are

$$G_0^{\pm}(\bar{\alpha})=\frac{\bar{\alpha}\left[\bar{\alpha}^2(\gamma_y-\gamma_x)+\gamma_x+\gamma_y+2h\right]\pm\sqrt{2Q(\bar{\alpha})}}{2P_2(\bar{\alpha})}, \tag{3.17}$$

where

$$Q(\bar{\alpha}) = \kappa\left(\bar{\alpha}^2 - r_-^2\right)\left(\bar{\alpha}^2 - r_+^2\right) \tag{3.18}$$

$$\kappa = -\left(\gamma_x - \gamma_y\right)\left(h + \varepsilon_0\right), \tag{3.19}$$

$$r_\pm = (-\kappa)^{-1/2}\sqrt{h^2 + \gamma_x\gamma_y + \left(\gamma_x + \gamma_y\right)\varepsilon_0 \pm A}, \tag{3.20}$$

$$A = \sqrt{\left(h^2 + \gamma_x^2 + 2\gamma_x\varepsilon_0\right)\left(h^2 + \gamma_y^2 + 2\gamma_y\varepsilon_0\right)}. \tag{3.21}$$

The four roots of Q, $\pm r_\pm$, are branch points of G_0. The integrated density of states in the thermodynamic limit, $\mathcal{N}_0(\varepsilon_0)$, now reads

$$\mathcal{N}_0(\varepsilon_0) = \lim_{s\to\infty}\mathcal{N}(\varepsilon) = \lim_{s\to\infty}\mathcal{I}(\varepsilon) = \mathcal{I}_0(\varepsilon_0), \tag{3.22}$$

$$= \frac{1}{2\mathrm{i}\pi}\int_{\Gamma_1}\mathrm{d}\alpha\left[G_0^+(\bar{\alpha}) - G_0^-(\bar{\alpha})\right]. \tag{3.23}$$

A natural choice for the G_0 branch cuts is given by the curves Γ_0 and Γ_1, on which the G poles accumulate as s increases. It indeed corresponds to the direction, in the complex plane, for which the quantity computed in Eq. (3.22) is real at each (infinitesimal) step of the integration. This latter condition was in fact implemented to draw the curves Γ_0 and Γ_1 in the different figures.

In the next section, we analyze in detail the four above mentioned different regions in the phase diagram, in terms of $\mathcal{N}_0(\varepsilon_0)$, its derivative and the density of states $\rho_0(\epsilon_0) = \partial_{\varepsilon_0}\mathcal{N}_0(\varepsilon_0)$. These quantities are, in most cases, computed as indicated in Eq. (3.22). It may happen, as noted below, that the Γ_1 curve has a complex shape, while Γ_0 is simple. Since the integral over all branch cuts, corresponding to Γ_0 and to Γ_1, sums to unity, we can safely consider the integral over Γ_0, instead of the non-trivial one over Γ_1, and write $\mathcal{N}_0(\varepsilon_0)$ as one minus this integral. We also face the case of state degeneracies, with corresponding symmetric or nonsymmetric classical orbits. Each such orbit is considered separately, by imposing the analyticity of G_0 in the region containing this orbit, bounded eventually by a closed branch cut on the sphere. The related $\Psi(\alpha)$ is zero along this line, and can be considered as vanishing outside the considered region. This corresponds quite well to the (numerically derived) eigenstate in the nonsymmetric case. However, in the symmetric case this description fails to reproduce the exact eigenstates since the latter is generically a linear combination of states located close to the classical orbits.

3.5.2 Analytical expressions of the densities of states

A precise study of the branch cuts Γ_0 and Γ_1 allows one to distinguish between five different forms of the density of states (labelled (a, b, c, d, e) below) that can be expressed in terms

of the complete elliptic integral of the first kind

$$K(m) = \int_0^{\pi/2} (1 - m\sin^2\theta)^{-1/2} \mathrm{d}\theta, \tag{3.24}$$

the incomplete elliptic integral of the third kind

$$\Pi(n, \phi|m) = \int_0^{\phi} (1 - n\sin^2\theta)^{-1} (1 - m\sin^2\theta)^{-1/2} \mathrm{d}\theta, \tag{3.25}$$

and the complete elliptic integral of the third kind $\Pi(n|m) = \Pi(n, \pi/2|m)$.

Depending on the Hamiltonian parameters, we have already distinguished between four different zones, following the classical surface singularities. We will now show how these zones are characterized in terms of the density of states behavior. Indeed, each time a classical surface singularity (maximum, minimum or saddle point) is crossed, the level sets (classical orbits or Husimi function local maxima) experience topological changes, as well as the integration contours, leading to a new expression for the integrated density of states. We now detail these different expressions, by describing each zone.

• Zone I: $|\gamma_y| < \gamma_x < h$.

Within this range of parameters (which coincides to the "symmetric phase" discussed in Sec. 3.3.1) the spectrum lies in the interval $-h \leqslant \varepsilon_0 \leqslant h$ and the density of states is a smooth decreasing function of the energy as can be seen in Fig. 3.1. The distribution of Majorana polynomial roots in this zone is similar to that displayed in Fig. 3.3(b). In the complex plane, Γ_0 and Γ_1 lie in the imaginary and real axes respectively. The integrated density of states is given by

$$\mathcal{N}_0^{(b)}(\varepsilon_0) = 1 + \frac{\sqrt{2}}{\pi r_+ \sqrt{-\kappa\ \gamma_x\gamma_y}} \Big[a_-^2 \Pi\Big(\mu r_-^2 \Big| \frac{r_-^2}{r_+^2}\Big) - a_+^2 \Pi\Big(\frac{r_-^2}{\mu} \Big| \frac{r_-^2}{r_+^2}\Big) + 2\sqrt{\gamma_x\gamma_y}(h + \varepsilon_0) K\left(\frac{r_-^2}{r_+^2}\right) \Big],$$

with

$$a_\pm = h \pm \sqrt{\gamma_x\gamma_y} \quad , \quad \mu = \frac{\sqrt{\gamma_x} - \sqrt{\gamma_y}}{\sqrt{\gamma_x} + \sqrt{\gamma_y}}. \tag{3.26}$$

• Zone II: $|\gamma_y| < h < \gamma_x$.

In this region, one must distinguish between two cases:

– II (a): $-\frac{h^2+\gamma_x^2}{2\gamma_x} \leqslant \varepsilon_0 \leqslant -h$. Γ_0 coincides with the whole imaginary axis while Γ_1 is made of two disconnected segments in the real axis as depicted in Fig. 3.3(a). Here, the integrated density of states reads

$$\begin{aligned} \mathcal{N}_0^{(a)}(\varepsilon_0) \;=\; 1 + \frac{\sqrt{\kappa} r_+^2}{\pi r_- \sqrt{2\gamma_x\gamma_y}} \Bigg[& \Pi\left(1 - \frac{r_+^2}{\mu} \Big| 1 - \frac{r_+^2}{r_-^2}\right) \left(1 - \frac{r_-^2}{\mu}\right) - \\ & \Pi\left(1 - \mu r_+^2 \Big| 1 - \frac{r_+^2}{r_-^2}\right) (1 - \mu r_-^2) \Bigg]. \end{aligned}$$

– II (b): $-h \leqslant \varepsilon_0 \leqslant h$. Γ_0 and Γ_1 are the same as in zone I and the analytic expression of the density of states is given by Eq. (3.26).

These two branches (a) and (b) of the density of states diverge at $\varepsilon_0 = -h$. Indeed, the integrated density of states can be simplified into the following form

$$\mathcal{N}_0^{\rm II}(-h) \;=\; 1 + \frac{2}{\pi\sqrt{\gamma_x\gamma_y}}\left\{a_- \tan^{-1}\left[\frac{a_-}{b_+(h)}\right] - a_+ \tan^{-1}\left[\frac{a_+}{b_0(h)}\right]\right\},$$

with

$$b_\pm(h) \;=\; \pm\big(\sqrt{h\gamma_x} - \sqrt{h\gamma_y}\big) + \sqrt{(\gamma_x - h)\,(h - \gamma_y)}, \tag{3.27}$$

$$b_0(h) \;=\; \sqrt{h\gamma_x} + \sqrt{h\gamma_y} + \sqrt{(\gamma_x - h)(h - \gamma_y)}, \tag{3.28}$$

and one can check that $\rho_0^{\rm II}(-h) = \partial_{\varepsilon_0}\mathcal{N}_0^{\rm II}(\varepsilon_0)|_{-h}$ diverges. One can further extract the leading behavior of the density of states near this point to obtain

$$\lim_{\varepsilon_0\to -h} \rho_0^{\rm II}(\varepsilon_0) = -\frac{\log|\varepsilon_0 + h|}{2\pi\sqrt{(\gamma_x - h)\,(h - \gamma_y)}}. \tag{3.29}$$

• Zone III: $h < -\gamma_y < \gamma_x$.

In this region, one must distinguish between three cases:

– III (a): $-\frac{h^2+\gamma_x^2}{2\gamma_x} \leqslant \varepsilon_0 \leqslant -h$. Γ_0 and Γ_1 are the same as in II(a), and the integrated density of states is given by Eq. (3.27).

– III (b): $-h \leqslant \varepsilon_0 \leqslant h$. Γ_0 and Γ_1 are the same as in I, and the density of states $\mathcal{N}_0^{(b)}(\varepsilon_0)$ is given in Eq. (3.26).

– III (c): $h \leqslant \varepsilon_0 \leqslant -\frac{h^2+\gamma_y^2}{2\gamma_y}$. Γ_0 is made of two disconnected segments on the imaginary axis while Γ_1 coincides with the whole real axis as depicted on the Majorana sphere in Fig. 3.3(c). The integrated density of states simply reads

$$\mathcal{N}_0^{(c)}(\varepsilon_0) \;=\; 1 - \mathcal{N}_0^{(a)}(\varepsilon_0), \tag{3.30}$$

where $\mathcal{N}_0^{(a)}$ is given in Eq. (3.27).

In this zone III, the density of states has two singularities at $\varepsilon_0 = \pm h$. The integrated density of states for these energies is given by $\mathcal{N}_0^{\rm III}(-h) = \mathcal{N}_0^{\rm II}(-h)$ [see Eq. (3.27)] and

$$\mathcal{N}_0^{\rm III}(h) = \frac{2}{\pi\sqrt{\gamma_x\gamma_y}}\left[a_+ \tan^{-1}\frac{a_+}{b_0(-h)} - a_- \tan^{-1}\frac{a_-}{b_-(-h)}\right]. \tag{3.31}$$

As done in zone II, one can compute the leading behaviour of the density of states near these points and one gets

$$\lim_{\varepsilon_0\to +h} \rho_0^{\rm III}(\varepsilon_0) = -\frac{\log|\varepsilon_0 - h|}{2\pi\sqrt{-\,(\gamma_x + h)\,(h + \gamma_y)}}. \tag{3.32}$$

For $\gamma_x = -\gamma_y$, the spectrum is symmetric with respect to $\varepsilon_0 = 0$ and the above expression gives the exact location, in the thermodynamic limit, of the so-called exceptional point observed in Ref. [11, 69] where a more complex diverging behavior was conjectured.

• Zone IV: $h < \gamma_y < \gamma_x$.

In this zone the density of states presents three different regions, of type d, e and b. The curve Γ_1 is more complex here, while Γ_0 always lies on a straight line in the complex plane. This is why we choose to integrate around Γ_0 instead of Γ_1.

– IV(d): $-\frac{h^2+\gamma_x^2}{2\gamma_x} \leqslant \varepsilon_0 \leqslant -\frac{h^2+\gamma_y^2}{2\gamma_y}$. Γ_0 coincides with the whole imaginary axis while Γ_1 has two disconnected branches lying symmetrically on the unit circle with respect to the imaginary axes. We are here facing a case where the classical orbits are related by symmetry (see Fig. 3.4(d)). One finds, for this region,

$$\begin{aligned}\mathcal{N}_0^{(d)}(\varepsilon_0) &= 1+\frac{2\sqrt{2}r_-}{\pi\left(r_- - r_+\right)\sqrt{-\gamma_x\gamma_y\left(h+\varepsilon_0\right)}}\Bigg[\frac{a_-^2}{u\left(-r_-\right)u\left(r_-\right)}\mathcal{E}\left(r_-,y\right) - \\ &\qquad \frac{a_+^2}{r_-^2 u\left(-\frac{1}{r_-}\right)u\left(\frac{1}{r_-}\right)}\mathcal{E}\left(\frac{1}{r_-},-y\right)\Bigg], \qquad (3.33)\end{aligned}$$

with

$$\begin{aligned}\mathcal{E}\left(r_-,y\right) &= \Pi\left[-\frac{u\left(-r_-\right)}{yu\left(r_-\right)},\sin^{-1}\sqrt{-y}\Big|\frac{1}{y^2}\right] - \Pi\left[-\frac{u\left(-r_-\right)}{yu\left(r_-\right)},\sin^{-1}\sqrt{y}\Big|\frac{1}{y^2}\right] - \\ &\quad \Pi\left[-\frac{u\left(r_-\right)}{yu\left(-r_-\right)},\sin^{-1}\sqrt{-y}\Big|\frac{1}{y^2}\right] + \Pi\left[-\frac{u\left(r_-\right)}{yu\left(-r_-\right)},\sin^{-1}\sqrt{y}\Big|\frac{1}{y^2}\right], \qquad (3.34)\end{aligned}$$

where

$$y = \frac{r_- - r_+}{r_- + r_+}, \qquad (3.35)$$

$$u\left(r_-\right) = \sqrt{\sqrt{\gamma_x}-\sqrt{\gamma_y}}r_- + \sqrt{\sqrt{\gamma_x}+\sqrt{\gamma_y}}. \qquad (3.36)$$

– IV(e): $-\frac{h^2+\gamma_y^2}{2\gamma_y} \leqslant \varepsilon_0 \leqslant -h$. This region shows two disconnected classical trajectories not related by symmetry (see Fig. 3.4), corresponding to two qualitatively different kinds of states which alternate in the spectrum. Γ_0 comprises two disconnected components lying in the imaginary axis, while Γ_1 is still complex and, moreover, is different for the two kinds of states. One finds

$$\begin{aligned}\mathcal{N}_0^{(e)}(\varepsilon_0) &= 1+\frac{\sqrt{2}}{\pi r_+\sqrt{-\kappa\gamma_x\gamma_y}}\Bigg\{-4\varepsilon_0\sqrt{\gamma_x\gamma_y}K\left(\frac{r_-^2}{r_+^2}\right) + a_-^2\left[\Pi\left(\frac{1}{\mu r_+^2}\Big|\frac{r_-^2}{r_+^2}\right) - \Pi\left(\mu r_-^2\Big|\frac{r_-^2}{r_+^2}\right)\right] + \\ &\quad a_+^2\left[\Pi\left(\frac{r_-^2}{\mu}\Big|\frac{r_-^2}{r_+^2}\right) - \Pi\left(\frac{\mu}{r_+^2}\Big|\frac{r_-^2}{r_+^2}\right)\right]\Bigg\}. \qquad (3.37)\end{aligned}$$

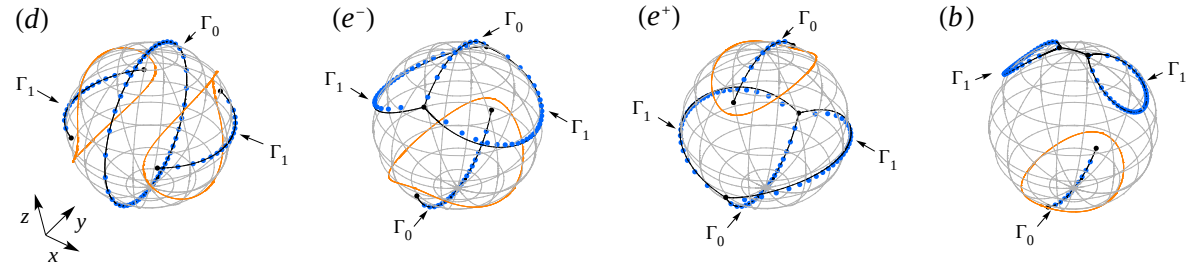

Figure 3.4: Roots of the Majorana polynomial (blue dots) ($\gamma_x = 10, \gamma_y = 5, h = 1$, and $s = 40$), classical orbits (orange curves), Γ_0 and Γ_1 (black curves), for eigenstates (labelled by n) in zone IV(d) ($n = 15$), zone IV(e) [(e^-): $n = 25$, (e^+): $n = 26$] and zone IV(b) ($n = 35$). In zone IV(e) two kinds of states coexist, of type (e^-) and (e^+), associated with the two classical orbits nonrelated by symmetry that alternate in the spectrum.

For the critical energy, at the boundary between IV(d) and IV(e), the integrated density of states simplifies to

$$\mathcal{N}_0^{\mathrm{IV}}\left(-\frac{h^2+\gamma_y^2}{2\gamma_y}\right) = 1 + \frac{1}{\pi\sqrt{\gamma_x\gamma_y}}\big[a_- c(-h) - a_+ c(h)\big], \tag{3.38}$$

with

$$c(h) = \tan^{-1}\left[\frac{h\sqrt{\gamma_x}+\gamma_y^{3/2}}{\sqrt{(\gamma_x-\gamma_y)(\gamma_y^2-h^2)}}\right], \tag{3.39}$$

$$\mathcal{N}_0^{\mathrm{IV}}(-h) = 1 - \frac{h}{\sqrt{\gamma_x\gamma_y}}. \tag{3.40}$$

In addition, the density of states singular behaviour is not symmetrical, and reads

$$\lim_{\varepsilon_0 \to \left(-\frac{h^2+\gamma_y^2}{2\gamma_y}\right)^-} \rho_0^{(e)} = -\frac{\log\left|\varepsilon_0 + \frac{h^2+\gamma_y^2}{2\gamma_y}\right|\sqrt{\gamma_y}}{\pi\sqrt{(\gamma_x-\gamma_y)\left(\gamma_y^2-h^2\right)}}, \tag{3.41}$$

$$= 2 \lim_{\varepsilon_0 \to \left(-\frac{h^2+\gamma_y^2}{2\gamma_y}\right)^+} \rho_0^{(d)}. \tag{3.42}$$

– IV(b): $-h \leqslant \varepsilon_0 \leqslant h$. Γ_0 is simply connected and lies on the imaginary axes. Like in the previous case, Γ_1 is non-trivial (see figure 3.4). Nevertheless, the expression found for $\mathcal{N}_0$ in this region coincides with that given by Eq. (3.26).

We now discuss the particular features found in the spectral region IV(e). At $\varepsilon_0 = -h$, the density of states is discontinuous (see Fig. 3.1), a fact which can be understood already

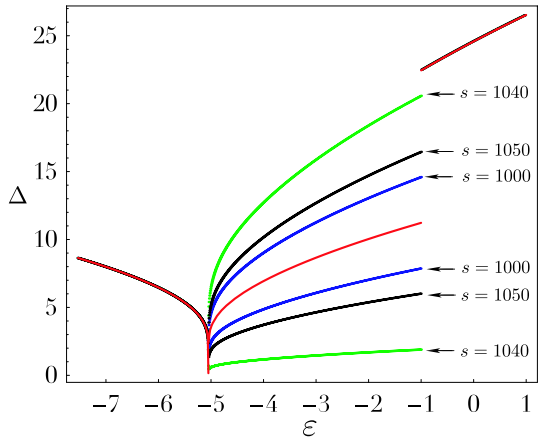

Figure 3.5: Gap between two consecutive levels as a function of the energy in region IV for $\gamma_x = 15$, $\gamma_y = 10$ and $h = 1$. In the central region, one sees a real lack of convergence toward the red line when increasing s, which is the average gap as computed in the thermodynamic limit.

from the topological analysis of the classical surface H_0. Indeed, the transition from zone (e) to zone (b) corresponds to leaving a local maximum of H_0 (see Fig. 3.2);therefore a family of classical orbits no longer contribute to the density of states.

In addition, as opposed to all other regions, the energy difference between two consecutive levels $\Delta^{(i)} = E^{(i+1)} - E^{(i)}$, computed for increasing s, does not converge towards the analytical result and, actually, does not converge at all. In region IV(e), $\Delta^{(i)}$ spreads over two branches $(+)$ and $(-)$, depending on the parity of the i, which oscillate without converging as s increases, as can be seen in Fig. 3.5. In this case, the gap we compute, in the thermodynamic limit, is actually the average gap, namely $\Delta_0(\varepsilon_0) = \frac{1}{2}\left[\Delta^{(+)}(\varepsilon_0) + \Delta^{(-)}(\varepsilon_0)\right]$. This is clearly to be understood in relation with the existence of two kinds of states alternating in the spectrum. Indeed, when analyzed separately within each set of states (e^+ or e^-), the computed energy gaps (between levels j and $j+2$ in the energy spectrum) converge as $s \to \infty$. In addition, both such gaps converge to twice the value of $\Delta_0(\varepsilon_0)$ (otherwise the two kind of states would not alternate as observed numerically). The oscillatory behaviour noted in Fig. 3.5 signals an energy drift (with s) of one set of energy levels with respect to the other.

3.6 Finite-size corrections

In the previous section, we have analyzed the thermodynamic limit of the LMG model spectrum by considering the leading terms in the expansion (3.16) [order $(1/s)^0$]. We now express the next-order corrections, which have already been shown, at least for the ground

state, to display nontrivial scaling properties [65, 58, 59, 12]. For the sake of simplicity, we limit the present analysis to the case $\gamma_x = 1, \gamma_y = 0$.

3.6.1 First-order expansion for G

Identifying terms of order $1/s$ in Eq. (3.8), one obtains the following form for the first-order term of G:

$$G_1^{\pm}(\alpha) = \hat{G}_1(\bar{\alpha}) + \tilde{G}_1^{\pm}(\bar{\alpha}), \tag{3.43}$$

with

$$\hat{G}_1(\bar{\alpha}) = \frac{h\bar{\alpha}\left[h\left(\bar{\alpha}^2+1\right)-\bar{\alpha}^2+1\right]}{2\left(1-\bar{\alpha}^2\right)Q(\bar{\alpha})}, \tag{3.44}$$

$$\tilde{G}_1^{\pm}(\bar{\alpha}) = \pm\frac{h\left(\bar{\alpha}^2+1\right)+2\left(\bar{\alpha}^2-1\right)\varepsilon_1}{2\left(\bar{\alpha}^2-1\right)\sqrt{2Q(\bar{\alpha})}}. \tag{3.45}$$

$\hat{G}_1$ is thus an analytic function of $\bar{\alpha}$ with poles at $\pm r_-$ and $\pm r_+$ while $\tilde{G}_1$ has the same branch cuts as G_0. $\mathcal{I}(\varepsilon)$ reads, recalling Eq. (3.11), and developing up to first order

$$\mathcal{I}(\varepsilon) = \frac{1}{2\mathrm{i}\pi}\oint_{\tilde{\Gamma}_1} G_0(\bar{\alpha})\,\mathrm{d}\bar{\alpha} + \frac{1}{s}\frac{1}{2\mathrm{i}\pi}\oint_{\tilde{\Gamma}_1} G_1(\bar{\alpha})\,\mathrm{d}\bar{\alpha}, \tag{3.46}$$

$$= \mathcal{I}_0(\varepsilon) + \frac{1}{s}\mathcal{I}_1(\varepsilon), \tag{3.47}$$

where $\mathcal{I}_0(\varepsilon)$ is given in Eq. (3.22) and where one can rewrite

$$\mathcal{I}_1(\varepsilon) = \frac{1}{4} + \frac{1}{2\mathrm{i}\pi}\int_{\Gamma_1} \mathrm{d}\bar{\alpha}\left[\tilde{G}_1^{+}(\bar{\alpha}) - \tilde{G}_1^{-}(\bar{\alpha})\right], \tag{3.48}$$

the $\frac{1}{4}$ coming from the integration over the poles.

For $\gamma_x = 1, \gamma_y = 0$, one has only zones I and II to consider, which focuses the analysis on only two energy regions. In zone I and II(b) one obtains

$$\mathcal{I}_1^{(b)}(\varepsilon) = \frac{1}{4} + \frac{(h+2\varepsilon_1)K\left(\frac{r_-^2}{r_+^2}\right) - 2h\ \Pi\left(r_-^2\middle|\frac{r_-^2}{r_+^2}\right)}{\pi r_+\sqrt{-\kappa}}, \tag{3.49}$$

whereas in region II(a) one finds

$$\mathcal{I}_1^{(a)}(\varepsilon) = \frac{1}{\pi\sqrt{\kappa}}\left\{\frac{2h}{r_-\left(r_+^2-1\right)}\left[K\left(1-\frac{r_+^2}{r_-^2}\right) - r_+^2\Pi\left(1-r_+^2\middle|1-\frac{r_+^2}{r_-^2}\right)\right] + \frac{h+2\varepsilon_1}{r_+}K\left(1-\frac{r_-^2}{r_+^2}\right)\right\}. \tag{3.50}$$

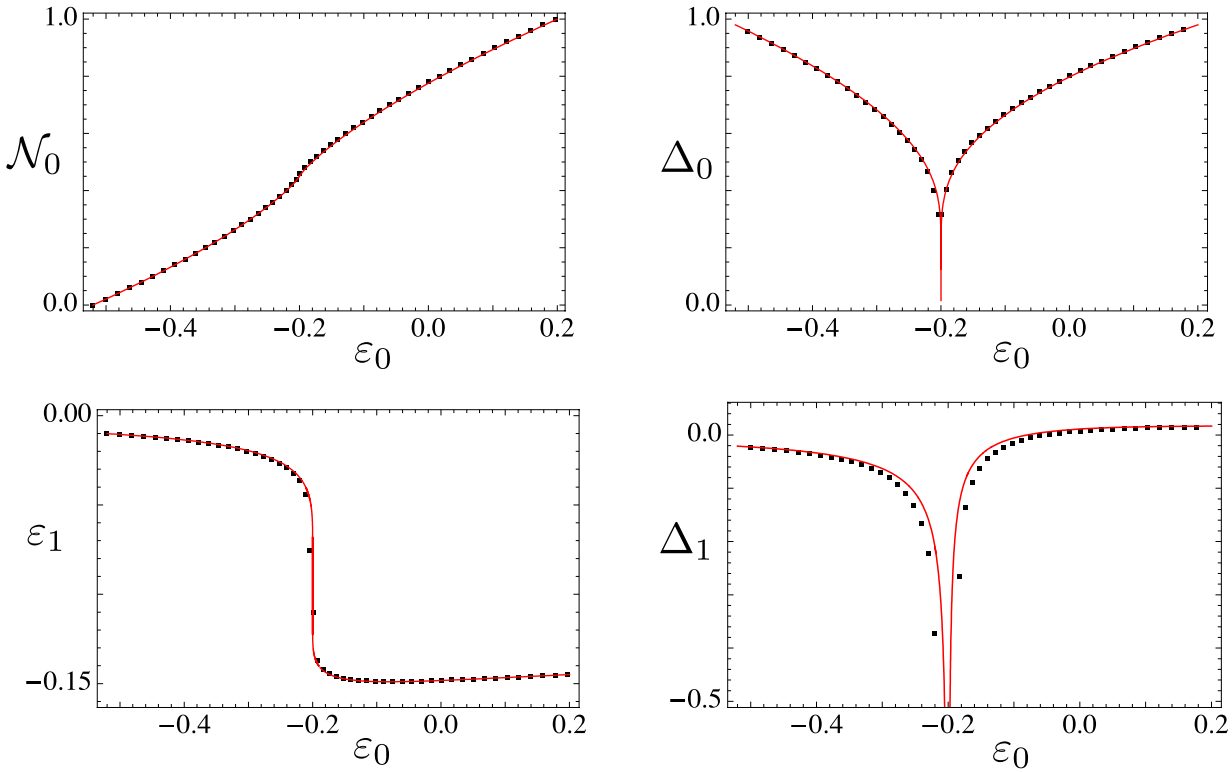

Figure 3.6: Comparison between analytical (red line) and numerical ($s = 50$ black dots) results for the (zeroth order) integrated density of states $\mathcal{N}_0$ (upper left) and energy gap Δ_0 (upper right) and the first order finite-size corrections to the energy ε_1 and to the gap (Δ_1, lower right).

Now, for all s, we expect that $\mathcal{I}(\varepsilon) = \mathcal{I}_0(\varepsilon_0)$, which implies, at order $1/s$, $\mathcal{I}_1(\varepsilon - \varepsilon_1/s) = \mathcal{I}_1(\varepsilon_0) = 0$. This condition allows one to compute the first-order correction to the energy, ε_1, which is displayed in Fig. 3.6 (lower left), and compares nicely with the numerical values, already for small values of s (here $s = 50$).

3.6.2 Energy gaps

The gap between two successive levels has already been discussed above in the zone IV case. At the thermodynamic limit, it generically reads

$$\Delta_0(\varepsilon_0) = \frac{1}{\rho_0(\varepsilon)} = \frac{\partial \varepsilon_0}{\partial \mathcal{N}_0(\varepsilon_0)}. \tag{3.51}$$

With the analysis done in the previous section, we can now compute finite size corrections to the gap. To first order, we obtain

$$\Delta = \Delta_0 + \frac{1}{s}\Delta_1 = \Delta_0\left(1 + \frac{1}{s}\frac{\partial\varepsilon_1}{\partial\varepsilon_0}\right). \tag{3.52}$$

The above derived values of ε_1 allow us to get a closed form for Δ_1, which nicely compares to the numerical values, as can be seen in Fig. 3.6 (lower right) for $s = 50$.

The Δ_1 correction is singular at the exceptional points, which are, as discussed in Sec. 3.5 located at $\varepsilon_0 = -h$. Note that Leyvraz and Heiss numerically found a logarithmic singularity at the exceptional points [12]. A related feature was already observed for the gap between the ground state and the first excited state [58, 59]. In the latter case, a scaling hypothesis led to a derivation of the first order correction, showing a $n^{-1/3}$ behavior. Unfortunately, the scaling hypothesis cannot be used here at the exceptional points. We have determined the behavior of the gap in their vicinity; setting $\eta = |h + \varepsilon_0|$, one gets

$$\begin{aligned}
\Delta(\varepsilon_0 \to -h^+) &= -\frac{2\pi\sqrt{(1-h)h}}{\log\eta}\left\{1 - \frac{1}{s}\left[\frac{1}{4(h-1)} + \frac{\sqrt{(1-h)h}\sin^{-1}(1-2h)}{\eta\log^2\eta}\right]\right\}, \\
\Delta(\varepsilon_0 \to -h^-) &= -\frac{2\pi\sqrt{(1-h)h}}{\log\eta}\left[1 - \frac{1}{s}\frac{2\sqrt{(1-h)h}\sin^{-1}\sqrt{h}}{\eta\log^2\eta}\right].
\end{aligned} \tag{3.53}$$

Note that the leading term is simply the inverse of ρ_0 which is given in Eq. (3.29) and vanishes when η goes to zero.

3.7 Observable expectation values

In this section, we discuss the expectation values of spin observables for generic eigenstates of the LMG model. The simplest way to perform such a calculation is to use the Hellmann-Feynman theorem, which relates these expectation values to partial derivative of the eigenenergies with respect to Hamiltonian parameters. For instance

$$\langle\Psi|S_z|\Psi\rangle = -\partial_h E \quad , \quad \langle\Psi|S_x^2|\Psi\rangle = -2s\ \partial_{\gamma_x} E. \tag{3.54}$$

As an illustration, we compare in Figs. 3.7 and 3.8 three cases, computed numerically (at finite s) and via the Hellmann-Feynman theorem in the thermodynamic limit, *i. e.* replacing E by $s\,\varepsilon_0$. As expected, one can see an almost perfect agreement, except for zone IV(e) discussed below.

Let us still make use of the semi-classical analysis discussed in previous sections. The expectation value $\langle\Psi|\hat{O}|\Psi\rangle$ for an observable O reads [72], at leading order,

$$\langle\hat{O}\rangle = \frac{\langle\Psi|\hat{O}|\Psi\rangle}{\langle\Psi|\Psi\rangle} = \frac{1}{T}\int_0^T \mathrm{d}t\ \langle\alpha(t)|\hat{O}|\alpha(t)\rangle, \tag{3.55}$$

where T is the period of the classical orbit with energy ε_0 and $\alpha(t)$ the solution of the classical dynamics equation [21].

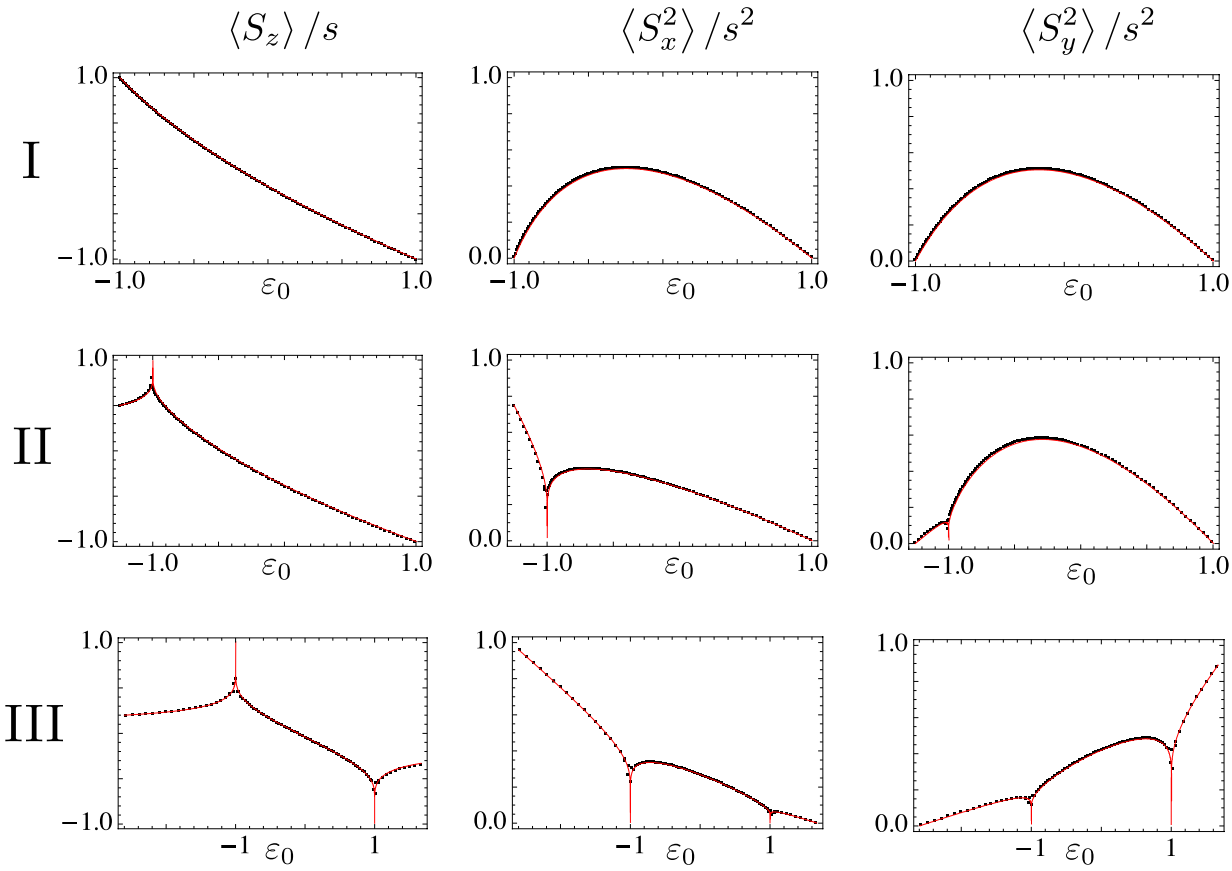

Figure 3.7: Comparison of expectation values of several observables obtained from numerical diagonalizations (black dots) and from the Hellmann-Feynman theorem in the thermodynamic limit (red lines). Plot parameters: $s = 60$, zone I : $(\gamma_x = 1/2, \gamma_y = 1/3, h = 1)$, zone II : $(\gamma_x = 2, \gamma_y = 1/2, h = 1)$, zone III : $(\gamma_x = 5, \gamma_y = -3, h = 1)$.

Let us focus on the $\langle S_z \rangle$ case. In zone I, it is maximal for the ground state. Indeed, in that region, H_0 is minimum for $\alpha = 0$, where the classical orbit degenerates to a single point at which the ground-state amplitude $|\Psi(\alpha)|^2$ is concentrated. As a result, although this true ground state differs from the simple fully-polarized state, $\langle S_z \rangle$ reaches its maximum value s.

This also occurs, in region II and III, for energies corresponding to the exceptional points. Here, classical orbits display a characteristic "figure eight" shape, with the values of α therefore differing from zero. The saturation effect results in that case from the fact that the period of the orbit diverges, with a vanishingly small classical velocity near $\alpha = 0$, forcing the expression in Eq. (3.55) to saturate. In all cases except zone IV(e), this latter computation leads to the same result as that simply obtained from the Hellmann-Feynman theorem.

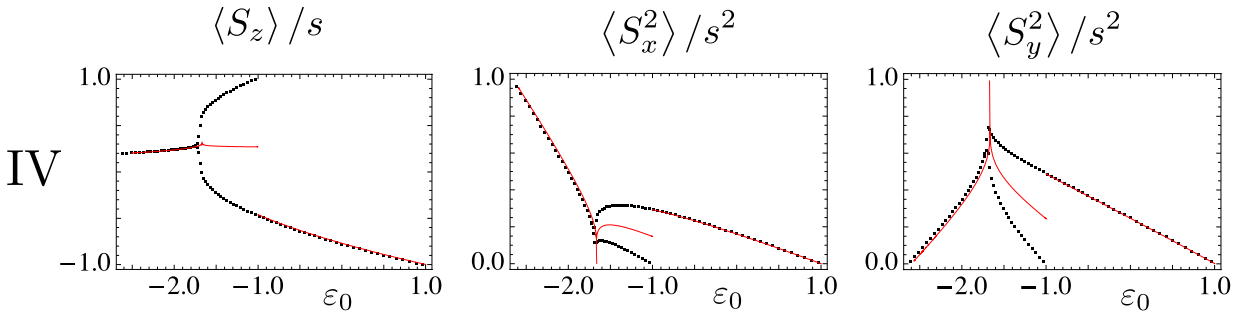

Figure 3.8: Same as Fig. 3.7, for a typical point in zone IV ($\gamma_x = 5, \gamma_y = 3, h = 1$) and $s = 60$. In the central region [zone IV(e)], there is a clear discrepancy between the numerical values (black dots), and those derived from the Hellmann-Feynman theorem (red lines).

In zone IV(e), the numerically computed expectation values alternate along two distinct curves, differing from the Hellmann-Feynman result. This corresponds to the already discussed existence, for the same energy ε_0, of two kinds of classical trajectories unrelated by symmetry (see Fig. 3.4). For each numerically derived eigenstate, the associated $|\Psi(\alpha)|^2$ concentrates alternatively near one of the two classical orbits. Integrating separately along each orbit precisely gives the two branches that are observed numerically (Fig. 3.8), while the Hellmann-Feynman computation leads to an averaged value.

3.8 Conclusion

We have studied in detail the full spectrum of the Lipkin-Meshkov-Glick model, by means of a coherent-states formalism. In a first step, we simply determined the main characteristics of the (zero temperature) phase diagram by analyzing extrema and saddle points of the classical-energy surface. This leads us to distinguish between four zones in the phase diagram corresponding to various patterns of the density of states whereas the usual ground-state criterion leads to only two distinct phases.

In a second step, we analyzed more deeply the nature of the eigenstates in terms of their associated Majorana polynomial roots. This enabled us to exactly compute the integrated density of states in the thermodynamic limit as well as the first finite-size corrections. This remarkable result mainly stems from the fact that the roots of the Majorana polynomial lies on well-defined curves, where their density varies monotoneously with the energy. We also clarified the nature of the so-called "exceptional" points in the spectrum.

Finally, we addressed the question of computing generic observable expectation values, in particular when, owing to subtle spectral reasons, the Hellmann-Feynman theorem cannot be used.

In principle, the same type of analysis could be performed for any spin Hamiltonian expressed in terms of single-spin operators (so-called "collective models"). Preliminary investigations of such models with cubic or quartic interactions are currently under study. Another perspective, also presently under investigation, concerns the dynamical properties both for evolutions under fixed and variable Hamiltonian parameters.

Chapter 4
Matrix Elements in the Semi-Classical Limit

4.1 Introduction

Semi-classical approximations for eigenstate wave-functions and energies clearly provide valuable informations on physical systems. Computing matrix elements of observables is also of prime interest, for example in order to address dynamical properties.

In this section we derive, in the case of spin systems, a semi-classical formula for operators matrix elements. We then apply our results in order to derive matrix elements between eigenstates of the LMG Hamiltonian.

Even if in the following we only treat a spin system which is effectively one dimensional, this approach generalizes for integrable systems having many degrees of freedom (see, for example, [73, 72]).

4.1.1 Semi-Classical Development

Let us fist recall the expression of the unnormalized matrix elements in Eq. (2.26) now computed between eigenstates $|\eta_l\rangle$ and $|\eta_m\rangle$ of the Hamiltonian $\hat{H}$. For this case Eq. (2.26) writes

$$\langle \eta_m|\hat{A}|\eta_l\rangle \;=\; \int \mathrm{d}\mu(\bar{\alpha},\alpha)\; \mathrm{e}^{nS_{m,l}(\bar{\alpha},\alpha)}\; \mathcal{A}[\bar{\alpha}, n^{-1}\partial_{\bar{\alpha}} + G^{(l)}(\bar{\alpha})], \tag{4.1}$$

with

$$S_{m,l}(\bar{\alpha},\alpha) = \int_{\bar{\alpha}_l}^{\bar{\alpha}} G^{(l)}(\bar{\alpha}')\mathrm{d}\bar{\alpha}' + \int_{\alpha_m}^{\alpha} \bar{G}^{(m)}(\alpha')\mathrm{d}\alpha' - \Omega(\bar{\alpha},\alpha), \tag{4.2}$$

where the normalization of the states is taken such that $\langle \eta_m|\alpha_m\rangle = 1$ and $\langle \alpha_l|\eta_l\rangle = 1$. We evaluate the integral in Eq. (4.1) using a saddle point approximation in the semi-classical parameter n, using the already defined (logarithmic derivative) G for wave functions computed from the WKB approximation, satisfying the extremal conditions

$$\partial_\alpha S_{m,l}(\bar{\alpha},\alpha) = \bar{G}_0^{(m)}(\alpha) - \partial_\alpha\Omega(\bar{\alpha},\alpha) + O(n^{-1}) = 0 \tag{4.3}$$

$$\partial_{\bar{\alpha}} S_{m,l}(\bar{\alpha},\alpha) = G_0^{(l)}(\bar{\alpha}) - \partial_{\bar{\alpha}}\Omega(\bar{\alpha},\alpha) + O(n^{-1}) = 0. \tag{4.4}$$

G_0 obeys Eq. (2.32), and, for a generic couple of conjugated complex variables $\{\bar{\alpha}, \alpha\}$, conditions (4.3) and (4.4) are not fullfilled, . In that case, the integration leads to an exponentially small contribution. However, whenever $\varepsilon_0^{(l)} = \varepsilon_0^{(m)} = \varepsilon_0$ and $\overline{\bar{G}_0^{(m)}}(\alpha) = G_0^{(l)}(\bar{\alpha}) = G_0(\bar{\alpha})$, Eq. (4.3) and (4.4) do have a set of solutions corresponding to the classical orbit $\mathcal{C}_0$ with energy ε_0. States with a different "macroscopic" energy ε_0 are exponentially concentrated in a band of order n^{-1} around different classical trajectories and their overlap is exponentially small in n. Non-zero matrix elements are obtained for states corresponding to the same energy at first order in n.

In order to fix the normalization condition, we define a function from the spectral energies to the orbit $\mathcal{C}$, $\bar{\alpha}_0(\varepsilon^{(m)}) = \bar{\alpha}_m$. This function is chosen such that, in the thermodynamic limit, $\bar{\alpha}_0(\varepsilon_0)$ is a point in the classical trajectory $\mathcal{C}_0$ varying continuously with ε_0.

The steepest descent approximation follows by integrating the second order fluctuations of $S_{m,l}$ perpendicular to the classical trajectory and evaluating the non-exponential diverging terms over the classical trajectory. This is done explicitly in section A.2.

Upon choosing the parametrization $\bar{\alpha}(\tau)$ given by the classical evolution (section A.2.2), we finally obtain

$$\langle \eta_m | \hat{A} | \eta_l \rangle \;=\; C \times e^{\Phi_{m,l}} \int_{-T/2}^{T/2} \mathrm{d}\tau \, \mathrm{e}^{\mathrm{i}(\varepsilon_1^{(m)} - \varepsilon_1^{(l)})\tau} \mathrm{A}_0(\bar{\alpha}, \alpha)[1 + O(n^{-1})], \tag{4.5}$$

where T is the period of the classical evolution corresponding to the energy ε_0 (see section A.2.2), C and $\Phi_{m,l}$ are defined respectively in Eq. (A.25) and (A.26).

4.1.2 Regular Orbits

For regular orbits (e.g. far from singular classical orbits), for which the WKB solution (2.35) is always well defined, the period T is finite. Moreover, for this case, we assume that a function $\varepsilon(\mathcal{I})$ exits and has a good thermodynamic limit, $\mathcal{I}^{(m)}$ being the action defined in Eq. (2.41) computed for the state m. The energy difference between near levels, l and m, is thus given by

$$\varepsilon^{(m)} - \varepsilon^{(l)} = \varepsilon(\mathcal{I}^{(m)}) - \varepsilon(\mathcal{I}^{(l)}) = \frac{2\pi(m-l)}{T} + O(n^{-1}), \tag{4.6}$$

where we use the fact that, at leading order, the classical action is the same for both states and the results of section A.2.3. The leading order term of the normalized matrix element, for the regular case, writes then

$$f_{m,l}^{\hat{A}} = \frac{\langle \eta_m | \hat{A} | \eta_l \rangle}{\sqrt{\langle \eta_m | \eta_m \rangle \langle \eta_l | \eta_l \rangle}} \;=\; \mathrm{e}^{\mathrm{i}\tilde{\Phi}} \int_{-T/2}^{T/2} \frac{\mathrm{d}\tau}{T} \mathrm{e}^{\frac{\mathrm{i}\,2\pi(m-l)\tau}{T}} \mathrm{A}_0[\bar{\alpha}(\tau), \alpha(\tau)], \tag{4.7}$$

with $\tilde{\Phi} = \frac{\mathrm{i}\ (\varepsilon^{(m)} - \varepsilon^{(l)})}{2} \left[\partial_\varepsilon \alpha_0(\varepsilon_0)\partial_\alpha \Omega(\bar{\alpha}_0, \alpha_0) - \partial_\varepsilon \bar{\alpha}_0(\varepsilon_0)\, \partial_{\bar{\alpha}} \Omega(\bar{\alpha}_0, \alpha_0)\right]$. In the following we consider that we can always chose a parametrization $\bar{\alpha}_0(\varepsilon_0)$ such that $\tilde{\Phi} = 0$ (for example taking $\bar{\alpha}_0(\varepsilon_0)$ real for all ε_0).

Eq.(4.7) translates the fact that the matrix elements in the semi-classical limit are given by the $(m-l)$-th Fourier coefficients of the classical observable evaluated along the classical flow. Since the integral of the classical flow equations is regular, A is an analytic function of τ. This fact implies that the amplitude of the Fourier mode decays exponentially as $|m-l| \to \infty$. This can be seen by considering the integral

$$f_k = \int_{-T/2}^{T/2} \frac{\mathrm{d}\tau}{T} \mathrm{e}^{\mathrm{i}k\frac{2\pi\tau}{T}} \mathrm{A}_0(\tau), \tag{4.8}$$

with $\mathrm{A}_0(\tau)$ a periodic and analytic function of τ with period T, and k stands for $m-l$. Note that, since integration is proceeded along a classical orbit, parametrized by τ, we dropped the $\alpha(\tau)$ dependance in $\mathrm{A}_0(\tau)$. Supposing $k > 0$, we can deform the contour like in Fig.4.1, by allowing for complex τ values. Periodicity, $\mathrm{A}_0(\tau + T) = \mathrm{A}_0(\tau)$, implies that the contributions (1) and (3) cancel and, for k sufficiently large, the contribution of (2) goes to zero as the contour is pushed to infinity. We can then write the integral as a sum over the poles τ_p of $\mathrm{A}_0(\tau)$:

$$f_k = \frac{2\pi\mathrm{i}}{T} \sum_p e^{\mathrm{i}k\frac{2\pi\tau_p}{T}} \mathrm{Res}[\mathrm{A}_0(\tau_p)] \xrightarrow[k\to\infty]{} 2\pi\mathrm{i}\ \mathrm{Res}[\mathrm{A}_0(\tau_1)] \frac{e^{ik\frac{2\pi\tau_1}{T}}}{T}, \tag{4.9}$$

where $\mathrm{Im}(\tau_1) < \mathrm{Im}(\tau_2) < \ldots$. Since $\mathrm{Im}(\tau_1) > 0$, f_k vanishes exponentially as $k \to \infty$. The procedure is similar for $k < 0$ where the contour is chosen in the half plane $\mathrm{Im}(\tau) < 0$.

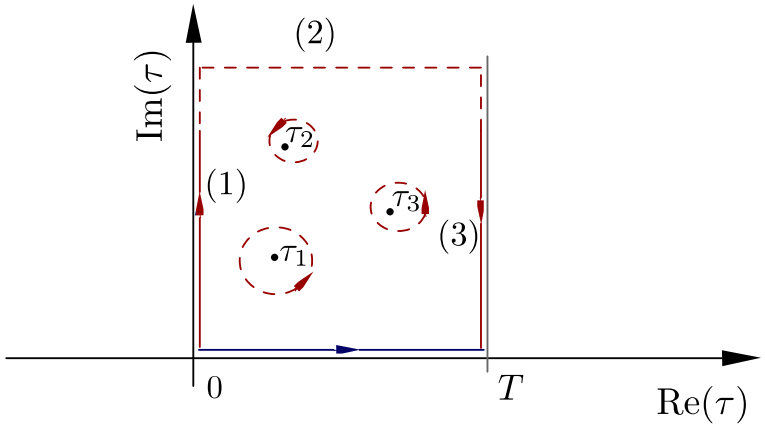

Figure 4.1: Integration contour for f_k in the complex τ plane.

For the present spin system, the symbol A_0 of a regular operator have poles for $[1 + \bar{\alpha}(\tau)\alpha(\tau)] = 0$; recall that the "symbol" refers to an operator expectation value between normalized spin coherent states. This is indeed the case for the symbols of the $su(2)$ generators

$$\mathbf{S} = \frac{n}{2}\left\{\frac{(\alpha+\bar{\alpha})}{1+\alpha\bar{\alpha}}, \frac{i(\alpha-\bar{\alpha})}{1+\alpha\bar{\alpha}}, \frac{(\alpha\bar{\alpha}-1)}{1+\alpha\bar{\alpha}}\right\}, \tag{4.10}$$

and of their powers. The condition $1 + \alpha\bar{\alpha} = 0$ arises only for non real values of τ and the analytic continuation of A_0 is considered. This is done regarding α and $\bar{\alpha}$ given by the classical flow equations (A.31,A.32) for complex values of τ. The $\{\bar{\alpha}, \alpha\}$ couples obtained this way will not, in general, be a complex conjugated pair of variables. Using the conservation of the energy along the evolution $H_0(\bar{\alpha}, \alpha) = \varepsilon_0$, and considering H_0 an rational function of its variables, one can obtain $\alpha(\bar{\alpha})$ defined in the Riemann sheet containing the initial conditions $\alpha_0(\bar{\alpha}_0) = \alpha_0$. This permits to integrate explicitly the equations of motion

$$\mathrm{i}\int_{\bar{\alpha}_0}^{\bar{\alpha}^*} \frac{\partial_{\bar{\alpha}}\partial_\alpha\Omega}{\partial_\alpha H_0}\mathrm{d}\bar{\alpha} = \tau^*, \tag{4.11}$$

where $\bar{\alpha}^*$ is defined such that the pole condition $[\partial_{\bar{\alpha}}\partial_\alpha\Omega(\tau^*)]^{-1/2} = [1 + \bar{\alpha}^*\alpha(\bar{\alpha}^*)] = 0$ is verified. The decay of the Fourier coefficients is dominated by τ_1 which is the solution of the pole condition with the smallest imaginary part. This procedure is applied in section 4.1.3 for computing matrix elements of the LMG model. The critical case for which the classical trajectory is a separatix and the period of the classical motion diverges is treated in chapter 5.

4.1.3 Operator matrix elements for the LMG Model

For the LMG model the Riemann surface $\mathrm{H}_0(\bar{\alpha}, \alpha) = \varepsilon_0$ has two sheets (see Fig. 4.2) and four couples $(\bar{\alpha}, \alpha)$ which are poles of the observables symbols for which $(1 + \bar{\alpha}\alpha) = 0$. The structure of poles in the complex-τ plane is pictured in Fig. 4.3. We observe that the "dynamics" for τ imaginary values is periodic, as can be understood from the top left figure, with closed trajectories in the $\{\mathrm{Re}(\alpha),\mathrm{Re}(\bar{\alpha})\}$ plane. So, there are infinite many poles, periodically repeated, along the imaginary axes and along the $\mathrm{Re}(\tau) = T/2$ line. Since their contribution decreases exponentially with $\mathrm{Im}(\tau)$ we are just going to consider the first 4 poles: two located at $\mathrm{Re}(\tau) = 0$ and two at $\mathrm{Re}(\tau) = T/2$. In fact for $k > 2$ the first two poles already give a very good approximation. In the S_z case, the residue corresponding to each pole can be simply obtained by

$$\mathrm{Res}[\mathrm{S}_z(\tau_p)] = \left.\frac{(1+\bar{\alpha}\alpha)\ \mathrm{S}_z(\bar{\alpha},\alpha)}{\partial_\tau(1+\bar{\alpha}\alpha)}\right|_{\tau=\tau_p} = \pm\frac{\mathrm{i}}{2\sqrt{\gamma_x\gamma_y}}, \tag{4.12}$$

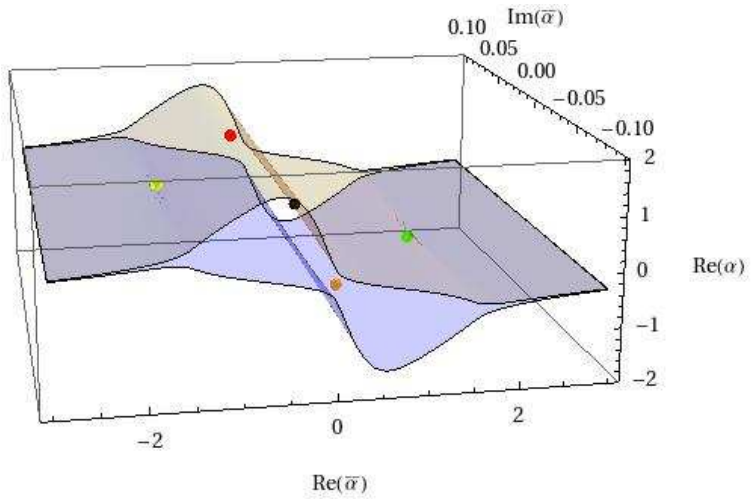

Figure 4.2: Pictorial representation of the Riemann surface $\mathrm{H}_0(\bar{\alpha}, \alpha) = \varepsilon_0$. Colored points represent the couples $(\bar{\alpha}, \alpha)$ for which $(1 + \bar{\alpha}\alpha) = 0$. The black point is the initial condition used to integrate the flow equations. The four-dimensional representation is made three-dimensional by dropping the imaginary part of α.

where the + sign is for "red" and "orange" poles and the − sign for "green" and "yellow" poles (see Fig. 4.3). For other observables we proceed similarly. The matrix elements of S_z in the semiclassical limit can thus be written

$$s^{-1}\langle \eta_m + k|\hat{S}_z|\eta_m\rangle = \frac{\pi}{T\sqrt{\gamma_x\gamma_y}}(e^{\mathrm{i}k\frac{2\pi\tau_1}{T}} - e^{\mathrm{i}k\frac{2\pi\tau_2}{T}})(1 + e^{\mathrm{i}k\pi}) + O(n^{-1}). \tag{4.13}$$

Note that, due to the symmetry of the LMG model, matrix elements of S_z (S_x) for even (odd) k vanish. The comparison between the semiclassical prediction of (4.13) and numerically derived values is given in Fig. (4.4). The semiclassical fits very well the numerical results in the region $-h < \varepsilon < h$, for both S_x and S_z, away from the critical point $\varepsilon_0 = -h$. Note that the fit gets better for increasing values of k meaning that the contribution of subleading poles vanishes exponentially as expected.

Near $\varepsilon_0 = -h$ the agreement with the numerical results is not very good, as expected from the fact that the semiclassical approximation breaks down near this point and Eq. (4.13) is no longer valid. For $\varepsilon_0 < -h$ there are two disjoint classical orbits corresponding to two-fold exponentially degenerate states, each one with a well defined parity. In this case the contributions of both orbits have to be taken into account with their respective parity. Due to the symmetry of the model Eq. (4.13) is still valid for S_z but that no longer true in the S_x case. The fact that the values for S_x alternate in this region is due to the fact that for odd and even m, the states corresponding to $m + k$ (for k odd) are of different nature. A finer analysis is still needed to address this case.

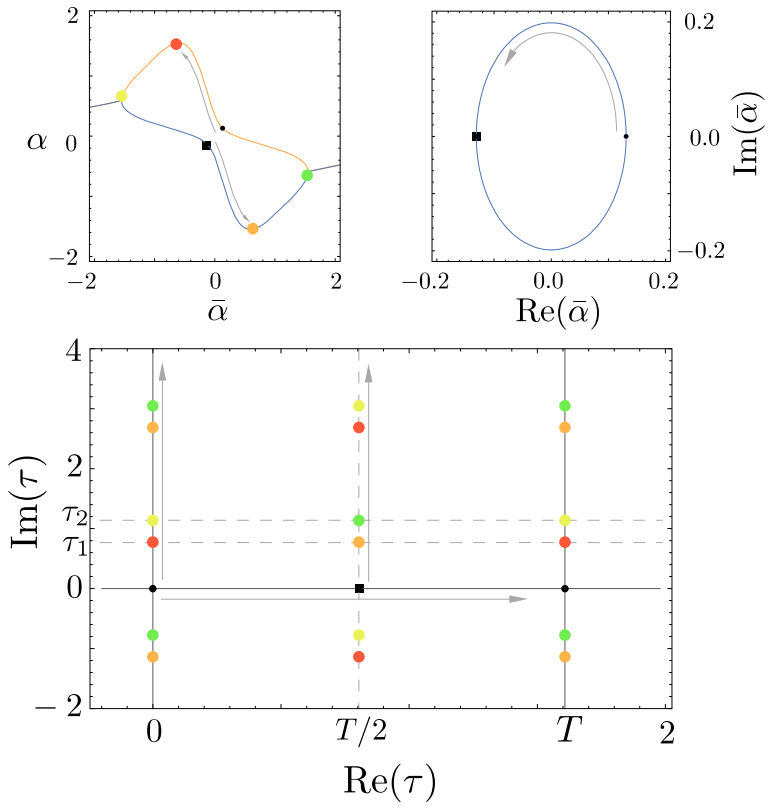

Figure 4.3: Real and Imaginary time Dynamics for the LMG model for $h = 1, \gamma_x = 2, \gamma_y = 1/3, \varepsilon_0 = 0.9$. (Down)- Complex τ plane. The color dots are poles of the observables where $(1 + \bar{\alpha}\alpha) = 0$, the black dot is the initial point of the dynamics and the black square is the opposite point of the evolution arising for $\tau = T/2$. (Up Left)- Imaginary time dynamics. The color dots are the couples $(\mathrm{Re}(\bar{\alpha}), \mathrm{Re}(\alpha))$ for which regular observables have poles. (Up Right)- Real time dynamics.

The decay rate of the matrix elements with k is given in Fig. (4.5), numerical calculations and semiclassical results are in very good agreement. The decay rate $\Gamma = \frac{2\pi}{T}\mathrm{Im}(\tau_1)$ can be computed explicitly, with $T = 2\pi\partial_{\varepsilon_0}\mathcal{N}_0$, $\mathcal{N}_0$ is the integrated density of states and τ_1 is given by Eq. (4.11). Near $\varepsilon = -h$, the decay rate goes to zero, translating the fact that, in an energy region of order n^{-1} around value,the decay is no longer exponential with k.

4.1.4 Conclusion

We have computed, by a semi-classical method, observable matrix elements for collective spin systems. As in the Schrödinger representation, they are in relation with the Fourier coefficients of the observables symbol computed along the classical flow. For energies

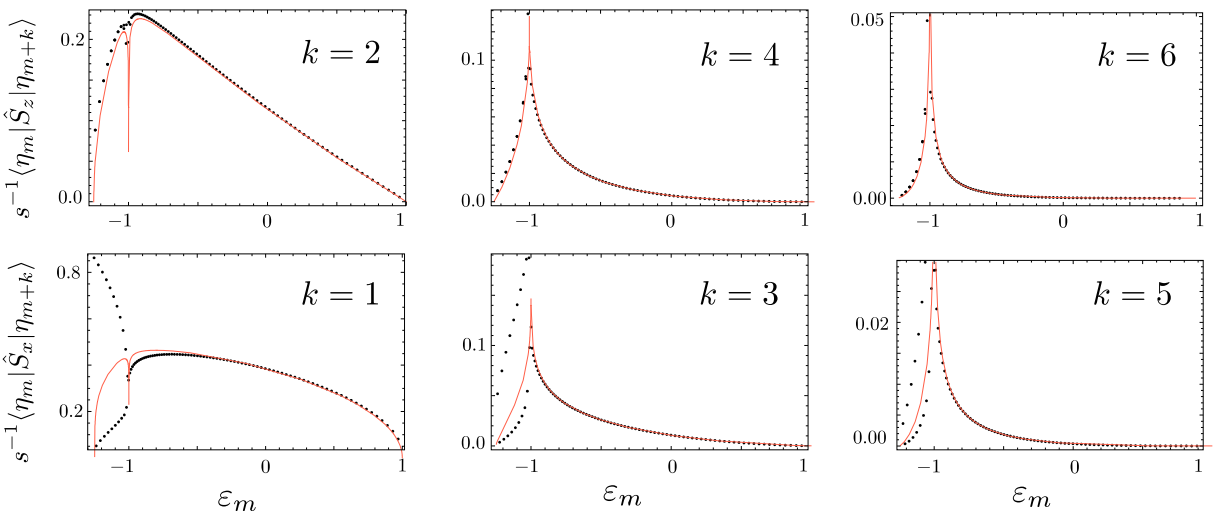

Figure 4.4: Comparison between semiclassical predictions (red curve) and numerical values (black dots) of the matrix elements of S_z and S_x computed between eigenstates of the LMG Hamiltonian for $h = 1, \gamma_x = 2, \gamma_y = 1/3$ and $n = 100$.

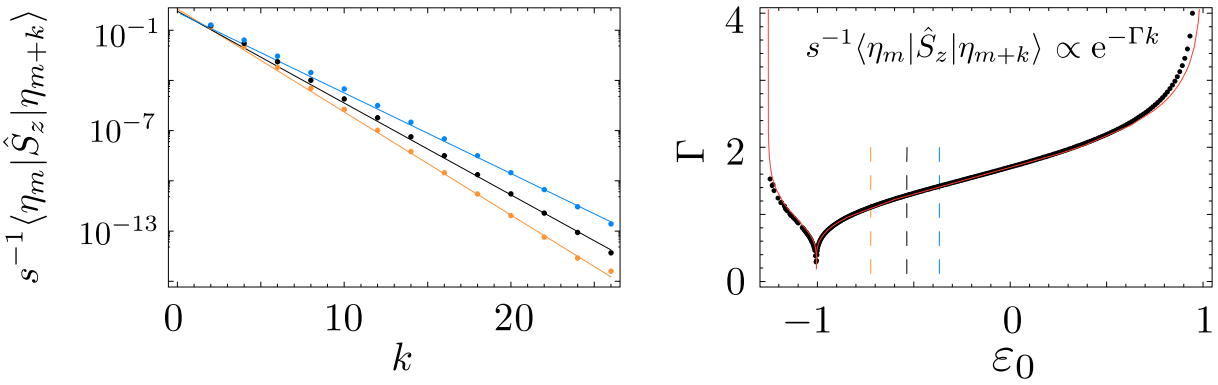

Figure 4.5: (Left) Decay of the matrix elements of S_z for three different energies. The decay rate $\Gamma = \frac{2\pi}{T}\mathrm{Im}(\tau_1)$ fits quite well the numerical values. (Right) Decay rate Γ as a function of the energy computed by the semiclassical method $\Gamma = \frac{2\pi}{T}\mathrm{Im}(\tau_1)$ (red curve) and numerically (black dots).

corresponding to regular classical orbits, the matrix elements vanish exponentially with k (which measures the distance, in terms of label, in the sorted list of energy levels). For spin systems, the matrix elements have been obtained by analyzing the pole structure of the symbols of observables; this was done explicitly for the LMG model and compared with numerically obtained values. Near the spectral critical points, the standard semiclassical approximation breaks down and the decay rate with k vanishes, which is just a manifestation that near these points, the matrix elements decay is no longer exponential

in k. A further analysis, similar to the one presented here, remains to be done to addresse the case of the broken phase region, where two disjoint classical orbits exist.

Chapter 5

Semi-classical Analysis of Spin Systems near Critical Energies

5.1 Introduction

Bohr-Sommerfeld (B-S) quantization formulæ for nonregular values of the energy parameter have been set up in [29, 32] in the case of quantum Hamiltonians in the Schrödinger representation. They differ from the regular case and show a logarithmic accumulation of the spectrum near energies corresponding to hyperbolic fixed points. In this section, the spectral properties of $su(2)$ Hamiltonians near hyperbolic points (HP) of the classical dynamics are studied. A method for obtaining an algebraic relation for the eigenvalues in the vicinity of a HP, in inverse powers of the semiclassical parameter $n = 2s$ (where $2s+1$ is the dimensionality of the $su(2)$ representation), is developped. It is then applied to a LGM-like Hamiltonian, where such critical points are found, either isolated (homoclinic case) or as HP pairs connected by the classical trajectories (heteroclinic case). Therefore, in addition to analyzing an isolated HP case, we also explain how to treat the more general case.

5.2 Quantization near Hyperbolic Points

In this section we use quantities that have been defined in chapter 2. If a HP is present along a classical trajectory, i.e. a saddle point of the energy $\mathcal{H}_0(\bar{\alpha}, \zeta)$ having $\partial_\zeta \mathcal{H}_0 = 0$ for some $\bar{\alpha}_i \in \mathcal{C}_0$, $\mathcal{I}_1$ diverges and the quantization condition (2.40) has to be modified for energies of order n^{-1} around the critical energy $\varepsilon_0 = \varepsilon_c$. Near such points, setting $\bar{\beta} = \bar{\alpha} - \bar{\alpha}_i$, $\mathcal{H}$ can be linearized and brought to the form

$$\tilde{\mathcal{H}}(\bar{\beta}, \zeta) - \varepsilon = \tau_2\, \zeta^2 + \tau_0\, \bar{\beta}^2 + \frac{\tau_{00} - \varepsilon_1}{n} + O(|\bar{\beta}|^3), \tag{5.1}$$

by a simple transformation $\Psi(\bar{\alpha}) = e^{n\, p(\bar{\beta})} \tilde{\Psi}(\bar{\beta})$, where p is a second order polynomial of $\bar{\beta}$. The constants τ_k depend on the parameter of the Hamiltonian around the HP. The solutions of

$$\left[\tilde{\mathcal{H}}(\bar{\beta}, n^{-1}\partial_{\bar{\beta}}) - \varepsilon\right] \tilde{\Psi}(\bar{\beta}) = 0, \tag{5.2}$$

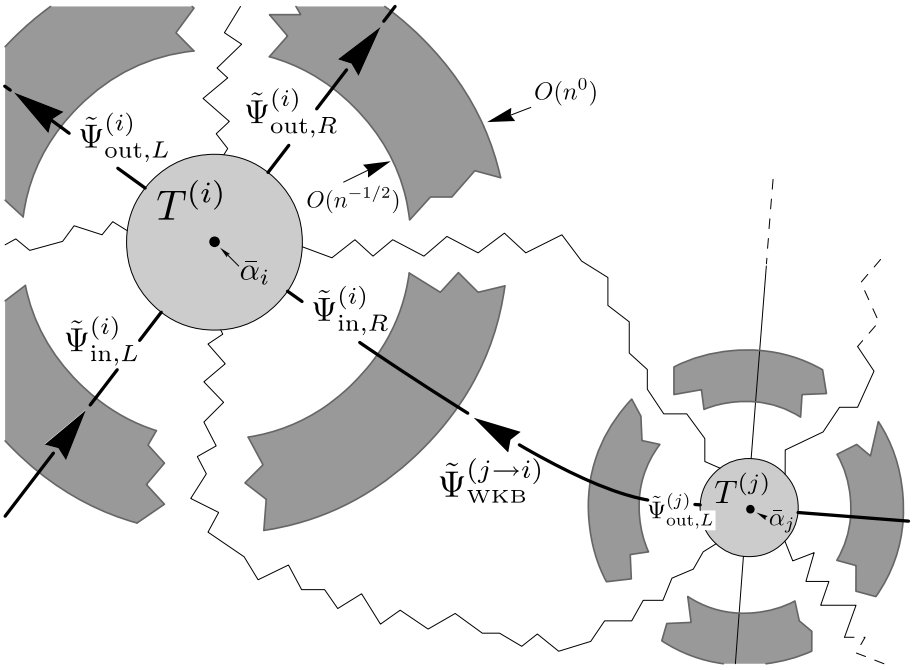

Figure 5.1: Phase space portrait of a classical trajectory $\mathcal{C}_0$ (full lines) describing a critical orbit that passing through two HP $\bar{\alpha}_i$ and $\bar{\alpha}_j$. For $O(n^{-1/2}) < |\bar{\alpha} - \bar{\alpha}_i| < O(n^0)$ both, the linearized solutions around HP point and the WKB solutions, coexist (dark gray region), permitting to identify both asymptotic behaviors. The "in" and "out" solutions are connected via the $T^{(i)}$ matrices. Branch cuts of the WKB solutions are displayed as broken lines.

are given explicitly in the form of Parabolic Cylindrical functions [74]. Let us consider the following linear combinations of these two independent solutions, having a well defined behavior when $|\bar{\beta}|\, n^{1/2} \to \infty$, for $\bar{\beta}$ in a vicinity of $\mathcal{C}_0$ (see Fig. 5.1 for the directions along which each limit is taken),

$$\left.\begin{matrix}\tilde{\Psi}_{\text{out},R}(\bar{\beta}) \\ \tilde{\Psi}_{\text{in},L}(\bar{\beta})\end{matrix}\right\} \;\to\; e^{-\mathrm{i}n\rho^2\bar{\beta}^2}\,\bar{\beta}^{-\frac{1}{2}+\mathrm{i}\eta}\left[1+O(|\bar{\beta}|^{-1}n^{-1/2})\right],$$

$$\left.\begin{matrix}\tilde{\Psi}_{\text{out},L}(\bar{\beta}) \\ \tilde{\Psi}_{\text{in},R}(\bar{\beta})\end{matrix}\right\} \;\to\; e^{\mathrm{i}n\rho^2\bar{\beta}^2}\,\bar{\beta}^{-\frac{1}{2}-\mathrm{i}\eta}\left[1+O(|\bar{\beta}|^{-1}n^{-1/2})\right],$$

where

$$\rho = \left|\frac{\tau_0}{4\tau_2}\right|^{1/4}, \qquad \eta = \frac{\varepsilon_1 - \tau_{00}}{4\rho^2\tau_2}. \tag{5.3}$$

Being solutions of a second order differential equation, these four functions are obviously not independent. The explicit form of the Parabolic Cylindrical functions provides a "con-

nection" between different asymptotic regions

$$\begin{pmatrix} \tilde{\Psi}_{\text{out},L} \\ \tilde{\Psi}_{\text{out},R} \end{pmatrix} = T \begin{pmatrix} \tilde{\Psi}_{\text{in},R} \\ \tilde{\Psi}_{\text{in},L} \end{pmatrix}, \tag{5.4}$$

with

$$T = \begin{pmatrix} 1 & -\bar{c} \\ c & -e^{-2\pi\eta} \end{pmatrix} + O(n^{-1}), \tag{5.5}$$

$$c = \sqrt{\frac{2e^{-\pi\eta}}{\pi}} \cosh(\pi\eta) e^{-\mathrm{i}\left[\eta \log\left(4n\rho^2\right)+\frac{\pi}{2}\right]} \Gamma\left(\mathrm{i}\eta + \frac{1}{2}\right). \tag{5.6}$$

Constraints of the type (5.4) give a set of local relations between the "in" and "out" basis. In the presence of two separate HP labelled by (i) and (j), a set of non-local relations is obtained by identifying the asymptotics of WKB solutions (see Fig. 5.1), leading to

$$\tilde{\Psi}_{\text{out},L} = e^{2\pi i n S(\bar{\alpha}_i, \bar{\alpha}_j)} \tilde{\Psi}_{\text{in},R}, \tag{5.7}$$

where $S(\bar{\alpha}_i, \bar{\alpha}_j)$ is regularized action integral given in Table 5.1, $\nu_j = (\pm \mathrm{i}\eta_j - \frac{1}{2})$ depending on the side R/L and j indexing HP. $\ln(x)$ is defined as having a branch cut along the negative real axes. $\sigma_k = 0, \pm 1$: 0 if the classical orbit does not cut the branch-cut of $\ln(\bar{\alpha} - \bar{\alpha}_k)$ and ± 1 if it cuts it in the up-down or down-up directions respectively.

Summarizing the local and non-local basis relations:

$$\mathbf{\Psi}_{\text{out}} = \mathbf{T}\mathbf{\Psi}_{\text{in}}; \qquad \mathbf{\Psi}_{\text{out}} = \mathbf{\Gamma}\mathbf{\Psi}_{\text{in}}, \tag{5.8}$$

where $\mathbf{\Psi}_{\text{out}}$ and $\mathbf{\Psi}_{\text{in}}$ are column vectors collecting the "in" and "out" solutions for each HP (i), $\mathbf{T}$ and $\mathbf{\Gamma}$ are matrices, the first coupling states with the same (i) and the second coupling sates with (i) and (j) linked by the classical trajectory. Quantization is obtained by imposing the compatibility relation

$$D = \det(\mathbf{T} - \mathbf{\Gamma}) = 0. \tag{5.9}$$

5.3 Examples

We now apply the general method presented above to a particular spin Hamiltonian

$$\hat{H} = \frac{2}{n}\left(hS_z - \frac{\gamma_x S_x^2 + \gamma_y S_y^2}{n} + \mu \frac{S_x^3}{n^2}\right). \tag{5.10}$$

The Lipkin-Meshkov-Glick (LMG) model [17] is obtained from Eq. (5.10) setting $\mu = 0$. The cubic term in Eq. (5.10) is added to provide asymmetric orbits in order to test the

Heteroclinic
$2\pi\mathrm{i}S(\bar{\alpha}_i,\bar{\alpha}_j) = 2\pi\mathrm{i}S_{i,j} + \frac{1}{n}\Big\{\nu_j \ln[(-1)^{\sigma_j}(\bar{\alpha}_i-\bar{\alpha}_j)] - \nu_i \ln[(-1)^{\sigma_i}(\bar{\alpha}_j-\bar{\alpha}_i)] + \sigma_i \mathrm{i}\pi\nu_i - \sigma_j \mathrm{i}\pi\nu_j\Big\};$
$2\pi\mathrm{i}S_{i,j} = \int_{\bar{\alpha}_j}^{\bar{\alpha}_i} \frac{\alpha}{1+\bar{\alpha}\alpha}\mathrm{d}\bar{\alpha} - \frac{1}{n}\int_{\bar{\alpha}_j}^{\bar{\alpha}_i} \partial_{\bar{\alpha}}\left[(\bar{\alpha}-\bar{\alpha}_i)(\bar{\alpha}-\bar{\alpha}_j)G_1\right] \frac{\ln[(-1)^{\sigma_i}(\bar{\alpha}-\bar{\alpha}_i)] - \ln[(-1)^{\sigma_j}(\bar{\alpha}-\bar{\alpha}_j)]}{\bar{\alpha}_i-\bar{\alpha}_j}\mathrm{d}\bar{\alpha};$
Homoclinic
$2\pi\mathrm{i}S(\bar{\alpha}_i,\bar{\alpha}_i) = 2\pi\mathrm{i}S_i + \frac{\mathrm{i}\pi\sigma}{n};$
$2\pi\mathrm{i}S_i = \int_{\bar{\alpha}_j}^{\bar{\alpha}_i} \frac{\alpha}{1+\bar{\alpha}\alpha}\mathrm{d}\bar{\alpha} - \frac{1}{n}\int_{\bar{\alpha}_j}^{\bar{\alpha}_i} \ln[(-1)^{\sigma}(\bar{\alpha}-\bar{\alpha}_i)]\partial_{\bar{\alpha}}\left[(\bar{\alpha}-\bar{\alpha}_i)G_1\right]\mathrm{d}\bar{\alpha};$

Table 5.1: Regularized Action Integrals

quantization relations in the most generic case. For the LMG model a detailed analysis of the phase space and the characterization of the critical points is given in chapter 3, and in [70, 14, 75]. For small values of μ the phase diagram presented in [14] is kept invariant. In particular the system conserves a homoclinic HP at $\alpha = 0$ for $\varepsilon_c = -|h|$ when $\gamma_x > |h| < |\gamma_y|$ and a heteroclinic trajectory joining two HP for $\gamma_x > \gamma_y > |h|$ corresponding to $\varepsilon_c = -\frac{h^2+\gamma_y^2}{2\gamma_y}$. For the homoclinic case, one obtains

$$D = -\frac{\cos\left[\pi n\left(S_L + S_R\right)\right]}{\sqrt{1+e^{-2\pi\eta}}} - \sin\Big\{\arg\left[\Gamma(1/2 - i\eta)\right] + \eta\log\left(4\rho^2 n\right) + \pi n\left(S_R - S_L\right)\Big\}, \quad (5.11)$$

as in the case of the Schrödinger representation [32], where $S_{R/L}$ are given by S_i in Table 5.1 (directions of integration are given in Fig. 5.2). For the heteroclinic case the quantization condition is rather lengthy and will not be given explicitelly. The comparison of the semi-classical quantization conditions with numerical diagonalization of the Hamiltonian using a matricial representation of the spin operators is given in Fig. 5.2. In both cases the agreement between the numerically derived energies and the points where $D = 0$ is remarkable. In the heteroclinic case, the matching becomes less accurate as the modulus of the renormalized energy η increases.

5.4 Matrix Elements

In the semiclassical limit, the normalized matrix elements

$$f_k^A(\varepsilon^{(m)}) = \frac{\langle\Psi_{m+k}|\hat{A}|\Psi_m\rangle}{\sqrt{\langle\Psi_{m+k}|\Psi_{m+k}\rangle\langle\Psi_m|\Psi_m\rangle}}, \quad (5.12)$$

of an observable $\hat{A}$ computed between eigenstates of an Hermitian operator H (with the energies $\varepsilon^{(m)}$ and $\varepsilon^{(m+k)}$), are known (see chapter 4) to be simply given as the amplitude of the k-th Fourier mode of the observable symbol A, evaluated along the classical orbit of energy $\varepsilon^{(m)}$ [72],

$$f_k^A(\varepsilon^{(m)}) = \frac{1}{T}\int_{-T/2}^{T/2} \mathrm{d}t\, \mathrm{e}^{\mathrm{i}k\frac{2\pi}{T}} \mathcal{A}[\bar{\alpha}(t), \zeta(t)], \quad (5.13)$$

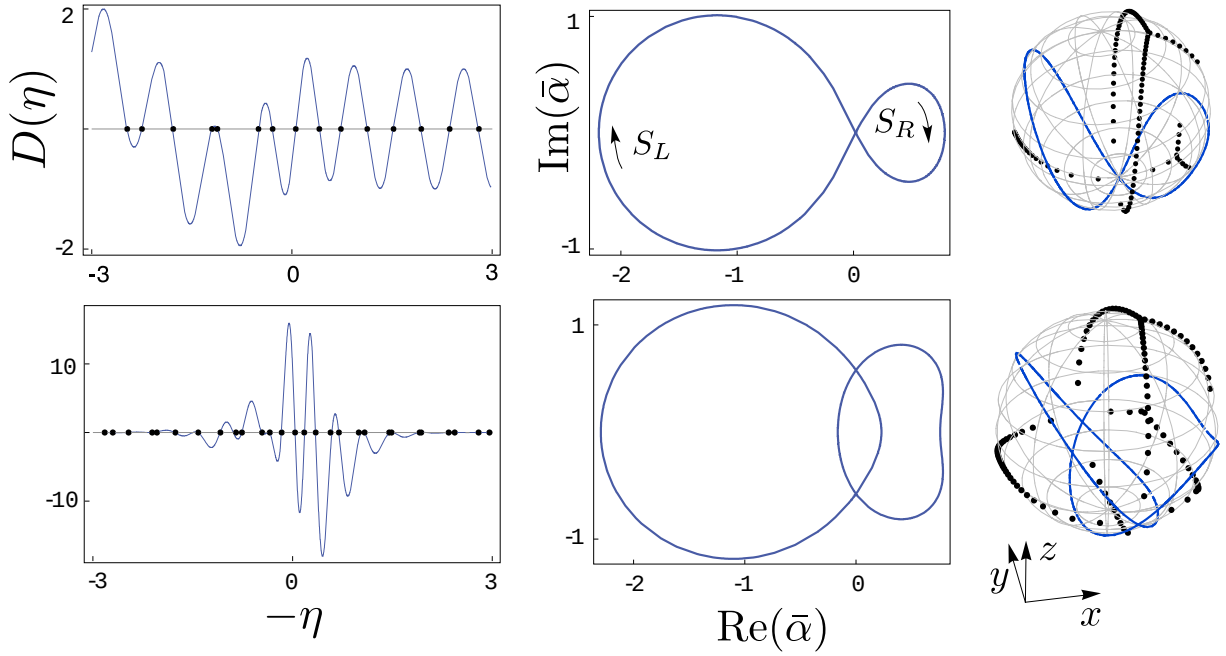

Figure 5.2: Homoclinic Case (Up): $h = 1; \gamma_x = 4; \gamma_y = 1/4; \mu = 5$. Heteroclinic Case (Down): $h = 1; \gamma_x = 5; \gamma_y = 2; \mu = 6$. Left: Comparison between the zeros of D (blue line) and the eigenvalues of (5.10) computed numerically (black dots) for $n = 500$. We define the renormalized energy $\eta = -\frac{h+\varepsilon_1}{2\sqrt{(\gamma_x-h)(h-\gamma_y)}}$; $\eta = \frac{\eta_1+\eta_2}{2} = \frac{-(\lambda+\gamma_y)\sqrt{\gamma_y}}{2\sqrt{(\gamma_x-\gamma_y)\left(\gamma_y^2-h^2\right)}}$ respectively for the homoclinic and heteroclinic cases. Middle: Stereographic projection of the critical classical orbit. Right: Critical orbit on the Riemann-Majorana Sphere; the zeroes of $\Psi(\bar{\alpha})$ (black dots) are plotted for $n = 120$, and condense in the semiclassical limit toward the branch cuts of G_0 [14, 76].

where T is the period of the classical orbit and the flow equations are given by:

$$\partial_t \bar{\alpha}(t) = -\mathrm{i}\,\partial_\zeta \mathcal{H}(\bar{\alpha}, \zeta); \quad \partial_t \zeta(t) = \mathrm{i}\,\partial_{\bar{\alpha}} \mathcal{H}(\bar{\alpha}, \zeta). \tag{5.14}$$

ζ is the variable conjugated to $\bar{\alpha}$, which reads $\zeta = \alpha(1 + \bar{\alpha}\alpha)^{-1}$ for the spin case. This result stands for regular orbits and can be obtained considering the action-angle variables. Since f is the Fourier transform of a analytic function, the matrix elements vanish exponentially with increasing k. This is a generalization of the result early obtained by Heisenberg in the harmonic oscillator case.

For singular orbits, containing an Hyperbolic Point, the period T diverges, and moreover no action-angle variables can be defined. Nevertheless it is still possible to estimate such matrix elements by analyzing local and global properties of the critical eigenstates [77]. Let us use the resolution of the identity in order to write matrix elements as integrals

over Σ_i, a domain of size $O(n^{-1}\ln n)$ around the HP $\bar{\alpha}_i$, and $\Sigma_{i,j}$, a domain of order n^{-1} around $\mathcal{C}_0$. Within these two sets of domains the eigenstates are given, respectively, by special functions and WKB approximation,

$$\begin{aligned}\langle\Psi_{m+k}|\hat{A}|\Psi_m\rangle &= \left[\sum_{(i)\to(j)}\int_{\Sigma_{i,j}} + \sum_{(i)}\int_{\Sigma_i}\right]\frac{\langle\Psi_{m+k}|\alpha\rangle\langle\alpha|\hat{A}|\Psi_m\rangle}{\langle\alpha|\alpha\rangle}\mathrm{d}\mu \\ &= \sum_{(i)\to(j)} g^A_{i\to j}[n(\varepsilon^{(m+k)}-\varepsilon^{(m)})] + \delta_{k,0}\sum_{(i)}\mathcal{A}(\bar{\alpha}_i,\zeta_i)\mu(i).\end{aligned} \tag{5.15}$$

The last equality follows from considering the symbol $\mathcal{A}$ constant on the domain Σ_i; by orthogonality of the eigenstates this term is nonzero only for $k=0$ where it gives the norm of the eigenstate inside the domain, $\mu(i)$. The regular functions

$$g^A_{i\to j}(\omega) = \int_{-\infty}^{\infty}\mathrm{d}t\,\mathcal{A}(t)\mathrm{e}^{\mathrm{i}t\omega} \tag{5.16}$$

are computed using the flow equations on the branch $i\to j$. Since $\mu(i)\propto\ln n$, we obtain at leading order,

$$f^A_{k=0}(\varepsilon^{(m)}) = \frac{\sum_{(i)}\mathcal{A}(\bar{\alpha}_i,\zeta_i)\mu(i)}{\sum_{(i)}\mu(i)}, \tag{5.17}$$

$$f^A_{k\neq 0}(\varepsilon^{(m)}) = \frac{\sum_{(i)\to(j)} g^A_{i\to j}[n(\varepsilon^{(m+k)}-\varepsilon^{(m)})]}{\sum_{(i)}\mu(i)}. \tag{5.18}$$

Diagonal matrix elements (mean values of observables) are thus given as a sum of ponderate weights of the different HP and depend on local properties of eigenstates near this points. On the contrary, non-diagonal elements are given by the global properties of the classical orbit. Since g^A is analytic, the matrix elements will decay exponentially as the energy difference increases; however, near the critical energy, the mean energy spacing is of order $n(\varepsilon^{(m+k)}-\varepsilon^{(m)})\propto k\ln^{-1}n$, meaning that the exponential decay in k becomes slower with increasing n (see Fig. 5.3). For an observable with $\mathcal{A}$ vanishing at the HP, the amplitude of all matrix elements vanishes as $O(\ln^{-1}n)$, for fixed k (Fig. 5.3) . This has a simple semi-classical explanation. In the critical case the volume of the phase-space corresponding to an energy band of order n^{-1} around ε_c is $O(n^{-1})$ for regions of type $\Sigma_{i,j}$ and $O(n^{-1}\ln n)$ for Σ_i. However, for $\mathcal{A}$ vanishing at the HP, the relevant regions to compute the matrix elements are $\Sigma_{i,j}$ which, by Heisenberg inequalities, can carry only a finite number of states $O(n^0)$ and not the total $O(\ln n)$ eigenstates. The only way of conciliating these two facts is to take a quantized observable described by an $O(\ln n)\times O(\ln n)$ matrix whose elements vanish in the classical limit.

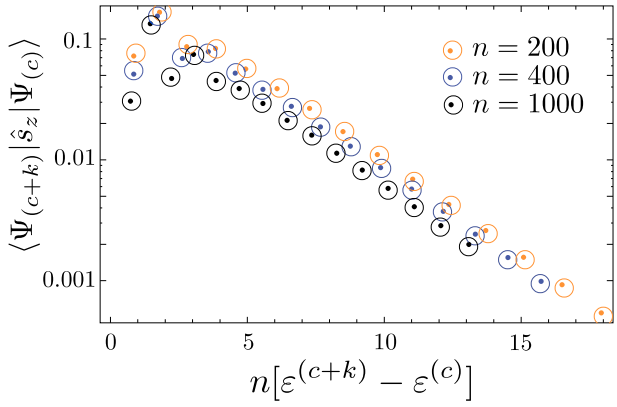

Figure 5.3: Matrix elements of the operator $\hat{s}_z = \frac{\hat{S}_z}{s}$ between two states near the critical energy. $\varepsilon^{(c)}$ is chosen to be the energy closest to the critical classical energy ε_c. The agreement of the numerical data (dots) with the predictions of Eq. (5.18) (circles) gets better for n big. The logarithmic downward shift as n increases is due to the fact that $\mu(i) \sim \ln^{-1} n$.

5.5 Conclusion

We have presented a method for computing semi-classical spectra associated to any number of heteroclinic junctions. Not only the expected average spacing $\sim \ln^{-1} n$ is observed, but an algebraic relation is derived for eigenvalues near the critical energy. The method is fully general and applies to any $su(2)$ Hamiltonian. In order to test it in full generality we have added a cubic term to the standard LMG model, breaking the quadratic underlying symmetry. The agreement with numerics is remarkable, especially considering the fact that the formulas are algebraically quite heavy in the case of two hyperbolic fixed points linked by heteroclininc junctions. We have also computed the matrix elements of observables, and show that their semi-classical behavior is universal, and different from the one in the regular situation. Moreover we have given a physical argument for the logarithmic vanishing of these matrix elements in the classical limit.

Chapter 6

Conclusion of Part I

We have studied collective spin models, with a particular focus on the thermodynamical limit, which is treated here within a semi-classical framework, using the spin coherent state representation. For this kind of models, integrability is related to the fact that they are described, in this representation, with only one degree of freedom. Analyzing the structure of the zeroes of the eigenfunctions, which display a regular but nevertheless rich pattern, we were able to derive analytically the full spectrum of the LMG model and to characterize its zero-temperature phase-diagram. Of particular interest for us, and indeed one of the initial motivation of this study, is the way gaps vanish at the thermodynamical limit, in relation with the behaviour and limitations of the adiabatic quantum computation approach addressed in Part II.

The same type of analysis could in principle be performed for any spin Hamiltonian expressed in terms of single-spin operators. However, for Hamiltonians presenting cubic or quartic interactions there are in general more critical values of the energy, corresponding to hyperbolic points of the classical evolution, where the density of state diverges in the thermodynamic limit. Preliminary investigations of such models show also an interesting "star-like" pattern of the zeroes of the wave functions, which remain to be explained. Characterizing these types of complex structures, arising from higher order interactions, could help to shed some light on the cases with more degrees of freedom, where even for quadratic interactions the patterns are quite complex (see appendix D).

We have also presented a method for computing semi-classical spectra associated to any number of heteroclinic junctions, arising for any $su(2)$ Hamiltonian. We tested it, numerically, for homoclinic and heteroclinic junctions and observed a very good agreement with the analytical predictions.

Observable matrix elements for collective spin systems were also studied, corresponding to both regular and singular semi-classical trajectories. For the regular case we were able to compute them explicitly for the LMG model and compared with numerically obtained values. A complete analysis nevertheless remains to be done, in particular in the broken phase region, where two disjoint classical orbits exist. Near singular energies, we were also able to compute the observables matrix elements, and show that their semi-classical behaviour is universal, and different from the exponential decay observed in the regular situation.

Although many research work have already been done in higher dimensional models, which are in general non-integrable, we think that a similar analysis to the one performed for the $su(2)$ could, at least for the integrable cases, be quite interesting. this may be the case in particular in what concerns the interplay between invariant tori and the manifolds of zeros of the wave function (appendix D).

Another perspective, also presently under investigation, concerns the dynamical properties both for evolutions under fixed and variable Hamiltonian parameters. In particular, for the former, the separatix plays an important role (see chapter 10). We expect to explore further this subject, based on the knowledge of the eigen-stucture presented in this work.

Part II

Adiabatic Quantum Computation

Résumé

Le calcul quantique a connu un grand développement durant ces dernières années, tant du point de vue théorique qu'expérimental. De nouvelles façons d'implementer le calcul quantique ont été proposées, comme une alternative au modèle initial des portes logiques, avec par exemple le calcul quantique adiabatique. Cette dernière proposition permet une interprétation assez physique des processus intervenant au cours du calcul. Dans un algorithme adiabatique, le problème à résoudre est ramené à la recherche de l'état fondamental d'un Hamiltonien, appelé "Hamiltonien du problème". Pour atteindre un tel état, on part d'un Hamiltonien plus simple, dont l'état fondamental est connu et facilement préparable. En agissant sur les paramètres externes du système, on fait alors évoluer le système en interpolant (par exemple de façon linéaire) entre les deux Hamiltoniens, suffisamment lentement pour laisser le système dans l'état fondamental (d'où le qualificatif de calcul "adiabatique"). En effet, la réussite de ce processus nécessite que l'on soit dans un régime (théorème adiabatique) tel que la durée totale reste beaucoup plus grande qu'un temps caractéristique proportionnel à l'inverse du carré du gap minimal (différence entre l'état fondamental et le premier état excité) rencontré pendant le processus.

En général, pendant l'évolution adiabatique, ce gap minimal tend vers zéro avec l'augmentation du nombre de degrés de liberté du système n. Il est donc crucial de déterminer avec plus de précision la dépendance de ce gap avec n. Si celui-ci s'annule exponentiellement, l'algorithme n'est pas efficace car le temps pour résoudre un problème avec n degrés de liberté augmente exponentiellement; si au contraire le gap présente une décroissance algébrique avec n, on considère que l'algorithme peut être efficace.

Dans cette deuxième partie 2 de la thèse, nous avons abordé divers aspects intéressant le calcul quantique adiabatique

Nous avons étudié dans un premier temps un modèle de Hamiltonien initial très particulier, qui permet de dériver une relation contraignant les énergies propres durant tout le processus. Ceci nous a permis de prévoir le comportement du gap simplement à partir de propriétés générales du Hamiltonien final. Nous avons testé cette approche dans un cas simple, lié à un problème de satisfabilité de contraintes (modèle 3-SAT). A partir d'une combinaison de résultats numériques et analytiques, nous concluons que la décroissance du gap avec n est de nature exponentielle.

Nous avons ensuite construit un modèle simple (appelé dans le texte "toy model") permettant de mettre en évidence la relation entre les transitions de phase quantiques et le calcul adiabatique. Le système proposé se ramène à un modèle de spins en interaction, où la représentation symétrique contient l'état fondamental du système. Ce modèle présente,

en fonction des paramètres, différents cas de figures: transitions de phase du premier ordre, avec un gap décroissant de façon exponentielle; transitions de phase du deuxième ordre, où le comportement est alors algébrique, et enfin des cas ou il n'y a pas de transition de phase quantique. Ce modèle met en évidence l'importance du choix du Hamiltonien initial et du chemin adiabatique considéré dans l'espace des paramètres, et peut servir comme un cas d'étude pour des modèles plus réalistes.

Enfin, nous avons étudié la dynamique des populations des états à travers une transition de phase, dans le cas du modèle LMG abordé dans la première partie. Une analyse numérique nous a montré que ces changements de population sont très sensibles à la présence des points exceptionnels dans le spectre. Nous avons proposé un premier modèle phénoménologique qui rend compte de quelques aspects de cette dynamique de populations. Nous avons ensuite développé un modèle quantique (d'interaction entre états propres instantanés) qui rend mieux compte du phénomène. En particulier la portée de ces interactions augmente à l'approche des points exceptionnels. Nous avons également analysé ce dernier phénomène dans le cadre semi-classique. Cette étude met également en évidence les défauts d'une description simple en terme de transitions de type Landau-Zener.

Chapter 7

Introduction

7.1 Classical and Quantum Computation

The basis of the modern computer science theory were set in the thirties, more than a decade before the rise of modern electronic computing machines. In particular, abstract devices (following a simple set of rules) where proposed by Alan Turing to simulate, in the line of the physicists thought experiments, the logic of any computer algorithm. Among these devices, the "Universal Turing Machine" play a particular role, in that they are formally able to simulate any other Tuting machines. A new reach scientific field arose, with connections to deep mathematics, like with the so-called Church-Turing thesis and the notion of effectively computable functions by recursion, in connection with Turing machine (abstract) implementation. Other important concepts were developped in parallel, like those of complexity measures. The computational complexity of a given problem is measured in terms of the physical resources (time, space, energy) invested in solving it. Different classes of complexity are defined based on how the quantity of resources grow as a function of the initial input size n (number of bits of the input). Following this idea, tractable (easy) problems can be solved with polynomial cost and intractable (hard) problems can only be solved with exponential cost. More precisely the class P contains all the computational decision problems that can be solved with polynomial cost and class NP the contains all those computational decision problems whose proposed solution can be verified with polynomial cost. Within NP class, the "NP-complete" stands for the class of problems that, if solved efficiently, could be used to solve all NP problems with a polynomial cost.

The idea of the quantum computer, i.e. a system that can process information by explicitely using quantum phenomena such as superposition and entanglement, was proposed in the early 1980's independently by Benioff and Feynman. Benioff thought of a quantum Turing machine [78, 79] that would use the reversible (unitary) time evolution of quantum mechanics as a way to do computation without dissipating any energy. Feynman had quite a different motivation and proposed a computer based on the laws of quantum physics as a natural and efficient way to simulate the dynamics of quantum systems[80], whose encoding in a classical computer/memory grows exponentially with the number of degrees

of freedom. Following the first proposal, by Deutsch [81], in 1985, of a quantum algorithm that could outperform the efficiency of a (deterministic) classical one, Shor showed in 1994 that it was possible to factorize integers efficiently using a quantum algorithm [82, 83]. This result has very important consequences, as it means that it is in theory possible to challenge the privacy of most current electronic communications. Shor's work sparked the attention of both theorists and experimentalists to the idea of the quantum computer and the race to build its respective hardware. Since then, a few other interesting quantum algorithms have emerged and some important experimental steps were achieved, but so far the quantum computer is still a machine that exists only in research laboratories, in an embryonary form [84].

The first quantum algorithms were constructed based on the so called circuit model where the information is treated, in analogy with classical computers, by a sequential set of unitary operations (gates). Different models for quantum computing exist today differing from the quantum circuit model. All of them have been demonstrated to be computationally equivalent to the circuit model, i.e. any computational problem that can be solved by the circuit model can be solved by these other models with only a polynomial overhead in computational resources. Among them are the measurement-based model, where the computation is performed using only non-unitary measurements on a well chosen initial entangled state; the topological models, in which the information is encoded in particular quantum states whose robustness (against errors and/or decoherence) has a topological origin; and finally quantum adiabatic models, that to some respect correspond more directly to physical (experimental) implementations, and therefore provide more intuitive physical picture of quantum computation.

7.2 Adiabatic Quantum Computation

Adiabatic Quantum Computation (AQC) has been proposed in 2001 by Farhi et al. [85] as an alternative way to perform quantum computation. It is based on the quantum adiabatic theorem [86] which states that a system initially in the eigenspace corresponding to a given energy level, and subject to a sufficiently slow varying time dependent Hamiltonian will remain in the corresponding eigenspace as long as there is no energy level crossing in the course of the evolution. In particular, if the system is prepared in the ground state, it will remain in the ground state of the instantaneous Hamiltonian. This approach has been proved to be equivalent to the standard model of quantum computation[87, 88], which is based on circuits of unitary gates. The time T necessary to perform the AQC is such that it satisfies the adiabatic theorem, limiting the probability of jumping to the first excited

state, which translates into the condition:

$$T >> \hbar \frac{|\partial_s H(s)|_{min}}{\Delta^2_{min}}, \tag{7.1}$$

where s is a parametrization of the time such that $t\,(s=0)=0$ and $t\,(s=1)=T$ (roughly, we have $s = t/T$), and where Δ_{min} is the minimum value, taken along the adiabatic evolution, of the energy gap between the ground and the first excited states. Therefore the time scaling with n (and so the computational efficiency) will be mainly determined by the behavior of the energy gap between the two lowest energy states, and is rather long whenever this scaling is exponentially small. In most cases of interest, the system will undergo a quantum phase transition (QPT), almost closing the gap along the Hamiltonian path. Therefore, the time scaling with the number n of quantum bits , and consequently the computational efficiency, will be dominated by the behavior of the energy gap at the QPT. The time will then increase exponentially with n in first order QPT, and algebraically (i.e. polynomially) in second order ones.

Up to now only exponential decreasing gaps were proved to exist for some adiabatic protocols trying to solve NP-complete problems [87, 89, 90, 91, 92] and some results, namely for the 3-SAT problem are rather inconclusive [85, 93, 94]. For the unsorted data base search a AQC algorithm was found that reproduce the gain of the Grover's algorithm for standard quantum computation [95]. Even if no new improvements in algorithm design were obtained up to now using this approach, an advantage pointed out by [96] is the robustness of this protocol against quantum errors.

Chapter 8

Projector-like Hamiltonian

The adiabatic approach to quantum computation depends crucially on the nature of the intermediate quantum phase transition that is met when solving hard problems, and in particular to the way the minimal gap scales with the system size. In this section we first try to address this problem, from a rather modest point of view, using a simple model characterised by a highly symmetrical initial Hamiltonian. In that case, we are able to determine the scaling of the gap based on very general properties of the final (so-called "problem") Hamiltonian. In the first section, a general formula for the gap scaling is derived, and it is applied to some generic examples in the second section. A similar work was developed independently by Znidaric and Horvat in [92].

8.1 Sum Rule

We consider an n qubits system having an Hilbert space is of dimension 2^n. States belonging to the computational basis are written as $|k\rangle = |x_0, x_1, ...x_{n-1}\rangle$ where $x_i = 0, 1$ is the i-th digit of the binary decomposition of $k = 0, ..., 2^n - 1$. The action of the Pauli operator σ_z in this computational basis is such that $\sigma_z^{(i)}|k\rangle = (-1)^{x_i}|k\rangle$.

A simple choice for H_0 is given by a projection operator

$$H_0 \;=\; \mathbb{I} - |\Rightarrow\rangle\langle\Rightarrow| . \tag{8.1}$$

with

$$|\Rightarrow\rangle = \bigotimes_{i=0}^{n-1} \left(\frac{|0\rangle + |1\rangle}{\sqrt{2}} \right) = \frac{1}{2^{n/2}} \sum_{k=0}^{2^n-1} |k\rangle, \tag{8.2}$$

as a single ground state (having equal probability along all the different possible basis kets $|k\rangle$) , and $2^n - 1$ degenerate excited states [95, 92]: Concerning the Hamiltonian H_P encoding the classical problem, we choose a cost function that has to be minimized to obtain the solution. We assign to each computational basis ket $|k\rangle$ an "energy cost"

$\varepsilon_{a(k)}$, where $a(k) \in \{0, 1, ..., g-1\}$ is a function of k labeling g different energies, and the degeneracy of each energy ε_a being noted n_a. H_P writes :

$$H_P = \sum_{k=0}^{2^n-1} \varepsilon_{a(k)} |k\rangle\langle k|. \tag{8.3}$$

Due to the simple (symmetrical) form of H_0, the result of the AQC process will only depend on the set of energy costs and degeneracies.

For a physical system, the total energy range $\varepsilon_{g-1} - \varepsilon_0$ should roughly scale as the number of degrees of freedom n; however we chose here to rescale the Hamiltonians such that the true (physical) extensive operators are n H_P and n H_0. This choice is made for the sake of simplicity, and this polynomial rescaling will not affect the exponential/algebraic nature of the gaps.

The evolution is, as usual, taken to be a linear interpolation of the two Hamiltonians

$$H(s) = (1-s)H_0 + sH_P. \tag{8.4}$$

with $s \in [0, 1]$.

We now use the symmetry of the initial Hamiltonian to reduce the dimensionality of the Hilbert space relevant to the adiabatic evolution. Consider the operator which permutes the state $|k\rangle$ and $|k'\rangle$

$$\mathbb{P}_{k,k'} = (\mathbb{I} - |k\rangle\langle k| - |k'\rangle\langle k'|) + |k\rangle\langle k'| + |k'\rangle\langle k|, \tag{8.5}$$

verifying $\mathbb{P}_{k,k'}^2 = \mathbb{I}$, $\mathbb{P}_{k,k'}^\dagger = \mathbb{P}_{k,k'}$ and thus having eigenvalues ± 1.

It is straightforward to verify that $[H_0, \mathbb{P}_{k,k'}] = 0$ for all pairs k, k'. Similarly $[H_p, \mathbb{P}_{k,k'}] = 0$ providing that $a(k) = a(k')$. There are $\sum_{a=0}^{g-1} \frac{1}{2} n_a(n_a - 1)$ permutations which fulfill this condition. For such pairs $[H(s), \mathbb{P}_{k,k'}] = 0$ for all s, implying that the evolution does not couple sectors with different eigenvalues of the $\mathbb{P}_{k,k'}$.

Since $\mathbb{P}_{k,k'}| \Rightarrow\rangle = | \Rightarrow\rangle$, H_0 reduces to the identity for all sectors with at least one negative eigenvalue under the permutation operations. The Hamiltonian restricted to these sectors is diagonal in the computational basis, for all values of s, yielding to a trivial evolution. The only sector undertaking a non-trivial evolution is symmetrical under all permitted permutations, and is spanned by the orthonormal vectors

$$|a\rangle_S = \frac{1}{\sqrt{n_a}} \sum_{k:a(k)=a} |k\rangle, \tag{8.6}$$

with $a \in 0, 1, .., g-1$. The Hamiltonian (8.4) restricted to this subspace writes

$$H_S(s) = \sum_{a=0}^{g-1}[(1-s)+s\,\varepsilon_a]|a\rangle_S\langle a|_S - \sum_{a,c=0}^{g-1}(1-s)\frac{\sqrt{n_c n_a}}{2^n}|c\rangle_S\langle a|_S. \quad (8.7)$$

Let $|\eta(s)\rangle = \sum_a \eta_a(s)|a\rangle_S$ be an eigenvector of $H_S(s)$ corresponding to the η-th excited energy $\lambda_\eta(s)$, we have then

$$[(1-s)+s\,\varepsilon_b]\eta_b(s) - (1-s)\frac{\sqrt{n_b}}{2^n}\sum_a \sqrt{n_a}\eta_a(s) = \lambda_\eta(s)\eta_b(s). \quad (8.8)$$

Simple manipulations of the above equation lead to a sum rule for the eigenenergies

$$\sum_{c=0}^{g-1}\frac{(1-s)\rho_c}{(1-s)+s\varepsilon_c-\lambda_\eta(s)} = 1, \quad (8.9)$$

where $\rho_c = \frac{n_c}{2^n}$ is the normalized fraction of the excited c-th energies ($\sum_{c=0}^{g-1}\rho_c = 1$). Note that the l.h.s. terms of Eq. (8.9) have poles at $(1-s)+s\,\varepsilon_a$; since by continuity λ cannot cross these poles, we conclude that the energies are bounded : $s\,\varepsilon_\eta < \lambda_\eta(s) - (1-s) < s\,\varepsilon_{\eta+1}$ for $s \in]0,1[$.

We now particularize the analysis to obtain the minimal gap, arising during the evolution, between the ground an the first excited states. By the above argument, the two lower energies are separated by the line $(1-s)+s\varepsilon_0$. At the critical point the value of the gap passes by a minimal value $\delta = \lambda - (1-s) - s\varepsilon_0$. This quantity is considered to be much smaller that the separation $s(\varepsilon_1 - \varepsilon_0)$ that scales roughly as g^{-1}. This is indeed the case in cases were the gap vanishes exponentially; the following approximation is not valid if δ is of order g^{-1}. Developing Eq. (8.9) up to the first order in δ and solving the second order equation, we obtain

$$\delta_\pm = \frac{(s-1)s\mu_{-1} - s^2}{2(s-1)\mu_{-2}} \pm \frac{1}{2}\Delta(s), \quad (8.10)$$

where

$$\Delta(s) = \sqrt{\frac{s^2\,(4\mu_{-2}\rho_0(s-1)^2 + (s-(s-1)\mu_{-1})^{\,2})}{(s-1)^2\mu_{-2}^2}}, \quad (8.11)$$

$\Delta(s)$ approximates the difference $\lambda_1(s) - \lambda_0(s)$ and

$$\mu_i = \sum_{\eta=1}^{g}(\varepsilon_\eta - \varepsilon_0)^i\,\rho_\eta. \quad (8.12)$$

The critical value of s for which the gap is minimal is obtained by setting $\partial_s \Delta(s_{crit}) = 0$. If μ_{-1} and μ_{-2} are finite in the limit $g \to \infty$ and ρ_0 is small, the minimal gap and the critical value of s simplify to

$$\Delta_{min} = \frac{2\mu_{-1}}{\mu_{-1}+1}\sqrt{\frac{\rho_0}{\mu_{-2}}}, \tag{8.13}$$

$$s_{crit} = \frac{\mu_{-1}}{\mu_{-1}+1}. \tag{8.14}$$

The hypothesis that the μ_i's have a good thermodynamic limit ($n \to \infty$) has to be verified for the particular problems. Eq. (8.13) is the main result of this section. The approximations involved and the accuracy of its predictions will now be tested numerically on some examples. A similar relation was derived independently in [92]. Other studies of adiabatic evolution where a projector-like H_0 is used where also performed [89], were, in particular, the optimal time needed to perform successfully the adiabatic algorithm is proved to grow as $\sqrt{2^n}$ if the degeneracy of the ground state n_0 is of order one in n.

8.2 Examples

8.2.1 A very simple test : Homogeneous magnetic field

Consider a classical problem whose solution is given by the ground state of the Hamiltonian

$$H_P = \frac{1}{n}\sum_{i=1}^{n} \sigma_z^{(i)}. \tag{8.15}$$

Note that there is no interaction between the n different two level systems; indeed this Hamiltonian describe an ensemble of non-interacting spin 1/2 subject to a constant magnetic field. The solution is trivial, minimizing the energy of each system separately. It is easy to obtain, by inspection, the eigen-energies of Eq. (8.15) and their degeneracies

$$\varepsilon_c = \frac{2k-n}{n}, \tag{8.16}$$

$$\rho_c = 2^{-n}\left(\begin{array}{c} n \\ k \end{array}\right). \tag{8.17}$$

The energy spectrum, for the symmetric sector, is shown in Fig. 8.1 (left and center). Using Stirling's approximation one obtains, for $n \to \infty$, $\mu_{-1} = \mu_{-2} = 1$ and Eq. (8.13) then simplifies to $\Delta = 2^{-n/2}$. Numerical confirmation of this scaling is shown if Fig. 8.1 (right). The minimal gap scales exponentially for this algorithm, meaning that the starting H_0 is not appropriated to "solve" this simple problem. But this permits however to test the accuracy of the approximations done in the previous section for the case of an exponentially closing gap.

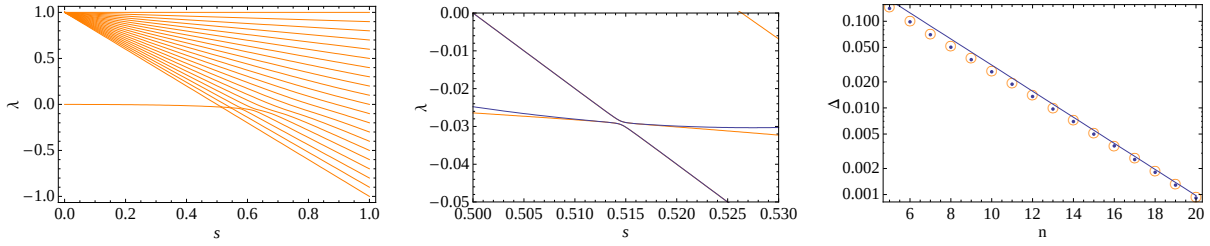

Figure 8.1: (Left) Energy spectrum as a function of s for $n = 20$, in the homogeneous magnetic field example. (Center) Detail of the minimal gap between the ground and the first exited states: numerical (orange), approximation by Eq. (8.10) (blue). (Right) Gap scaling with n: numerical (orange circles); Δ given by Eq. (8.10) computed for s_{crit} given in Eq. (8.10), μ_{-1} and μ_{-1} are computed numerically (blue dots); Scaling $\Delta \propto 2^{-n/2}$ (blue line).

8.2.2 3-SAT problem

The Boolean satisfiability problem (SAT) is a decision problem whose instance is a Boolean expression written using only AND, OR and NOT variables. The 3-satisfiability (3-SAT) problem is a special case belonging to the NP-Complete class; it is given in terms of n Boolean variables $x_1, ..., x_n$ and m clauses of 3 literals, for example:

$$(x_1 \vee x_4 \vee \bar{x_9}) \wedge (x_2 \vee x_3 \vee \bar{x_9}) \wedge ..., \tag{8.18}$$

where $\bar{x}$ denotes the negation of the Boolean variable x. The problem is to discover if, given a set of m clauses, the problem has a solution. Each clause C can be specified by the set $\{\{x_1(C), x_2(C), x_3(C)\}, \{s_1(C), s_2(C), s_3(C)\}\}$, where $x_i(C) = 1, ..., n$ specifies the variables involved and $s_i(C) \in \{-1, +1\}$ specifies whether they appear negated (-1).

Consider the Hamiltonian (or cost function)

$$H_P = \frac{1}{m} \sum_{C=1}^{m} \left(\frac{1 + s_1(C)\sigma_z^{x_1(C)}}{2} \right) \left(\frac{1 + s_2(C)\sigma_z^{x_2(C)}}{2} \right) \left(\frac{1 + s_3(C)\sigma_z^{x_3(C)}}{2} \right). \tag{8.19}$$

which is diagonal in the computational basis $|x_1, ..., x_n\rangle$, with eigenvalues m_v/m where m_v is the number of violated clauses. This Hamiltonian admits a zero eigenvalue if there exists at least one Boolean assigment that satisfies the classical problem.

If the adiabatic algorithm is performed, with a sufficiently long evolution time, the final state will be a symmetrical superposition of all the solutions minimizing the number of violated clauses, with ε_0 as the final energy of such states and ρ_0 their normalized fraction. The particular classical problem has a solution if ε_0 is zero.

The classical 3-SAT problem shows a SAT - NonSAT phase transition in the limit $n \to \infty$ as the control variable $\alpha = m/n$ equals $\alpha_c = 4.3$ [97], [98], where the fraction of

assignments that satisfy a typical problem goes from a finite value to zero as $n \to \infty$.

In order to use the above sum rule, derived in the previous section, we need to study how the quantities μ_i and ρ_0 behave when n increases. This behaviour has to be averaged over different possible sets of clauses. Since analytic expressions are not available for this problem, we study these quantities numerically, the results being displayed in Fig. 8.2. ρ_0 presents a clear exponential decay for $\alpha = 5$; for $\alpha = 4$ our numerical results are inconclusive but we know [97] from the existence of the SAT - NonSAT phase that it should at least decay less than exponentially. The μ_i do not present an exponential dependency on n so even if the gap is not exponential we expect Eq. (8.13) to give a good prediction. Even if μ_{-1}, μ_{-2} oscillate with n, their non exponential behaviour dictates that the gap depends mainly on the ρ_0 dependency with n.

Fig. 8.3 shows the average gap has a function of n for different values of α. As expected, we find an exponential decreasing gap for $\alpha = 5$, and the predictions of Eq. (8.13) are verified. We also computed an approximate gap by plugging in the formula the numerically obtained mean values of ρ_0 and μ_i, which leads to an overestimation. For $\alpha = 3, 4$ the decreasing should be non-exponential by the previous arguments; this is clear for $\alpha = 3$, but inconclusive in the case $\alpha = 4$, at least based on our numerical results.

8.3 Conclusion

Using a projector-like Hamiltonian as the starting Hamiltonian for a AQC algorithm permits to derive an algebraic relation (Eq. (8.9)) that eigen-energies have to respect along the evolution. This relation, when particularized for the ground and first excited state, leads to an approximated formula for the minimal gap arising during the adiabatic evolution as a function of some general features of the classical problem, ρ_0 and μ_i. This expression permits to conclude that if ρ_0 goes to zero much faster than μ_i the behaviour of the gap is mainly given by $\rho_0^{1/2}$. Based on the numerical computation of ρ_0 and μ_i, we conclude that this is indeed the case for the 3-SAT problem and so no exponential speed-up should be observed in this case, at least while starting from a fully symmetrical Hamiltonian H_0.

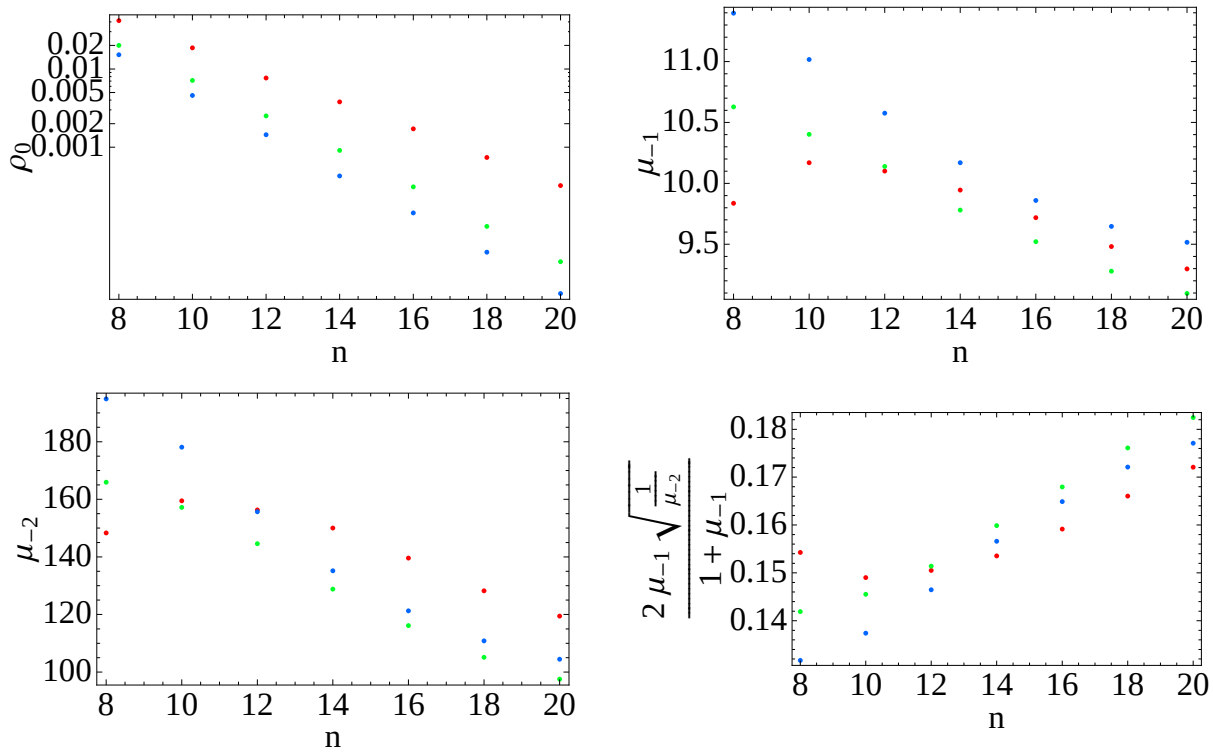

Figure 8.2: Numerical data for the 3SAT problem, averaged over 500 random realizations, $\alpha = 3, 4, 5$ (red, green, blue).

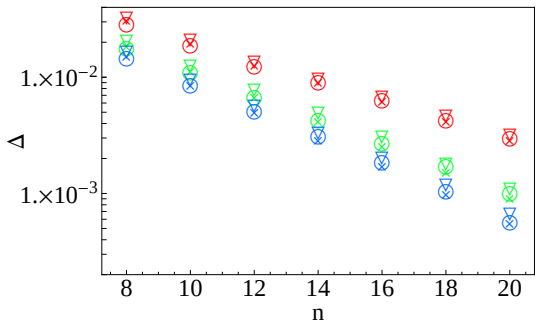

Figure 8.3: Minimal gap for the 3SAT averaged over 500 random problems, $\alpha = 3, 4, 5$ (red, green, blue). Numerical values (circles), average gap using formula Eq. (8.13) (cross), gap computed from the average ρ_0 and μ_i values (triangles)

Chapter 9

A Toy Model for Adiabatic Quantum Computation

9.1 The Adiabatic Algorithm

9.1.1 General Remarks

Let us first discuss the general properties of the Hamiltonians considered in this chapter. We scale all Hamiltonians such that they have a bounded spectrum. Even if for a typical physical system one expects the energy to be proportional to n, this is just a linear scaling and can be later taken into account in the total computational time for a more realistic physical system.

Given a classical computational problem one should first map its solution(s) onto a ground state of an Hamiltonian denoted H_P. We assume that the final measurement (output of the computation) is performed in the computational basis, and so, that the final Hamiltonian is diagonal in this basis. Once H_P is defined, one can ask for an optimal initial Hamiltonian H_0 and an optimal path $H(s)$ in the parameters space (that maximizes the energy gap).

We only consider Hamiltonian paths of the simple form $H(s) = (1-s)H_0 + sH_P$. This choice is motivated by the following arguments. First it is clear that any Hamiltonian path of interest will be such that $[\partial_s H(s), H(s)] \neq 0$. Indeed suppose that for a path $H(s)$ there exist an interval of values of $s \in [s_0, s_1]$ such that we have $[\partial_s H(s), H(s)] = 0$, implying that Hamiltonians within that interval commute with each others. In this situation two cases may occur: either there is one or more level crossings between the ground state and the first excited state and, in that case, the adiabatic condition is no longer valid; or the ground state experiences no level crossing (so its correspondent eigenvectors remains the same) and the evolution amounts to a rescaling of the energies which could be performed "instantaneously" without breaking the adiabatic condition, because all the non-diagonal matrix elements of $\partial_s H(s)$ vanish. In this case the evolution between s_0 and s_1 needs not to be done adiabatically. In the following we suppose that all Hamiltonian paths do not have such "commuting" intervals and so we end up with a path such that

$[\partial_s H(s), H(s)] \neq 0, \ \forall s \in [0,1]$, which is the nontrivial part of the protocol.

It should be clear that in most interesting cases the system will undergo a Quantum Phase Transitions (QPT) along the Hamiltonian path (see for example [99, 100]) . Indeed the complexity of a classical computational problem translates into an increasing of the computational time with n. In the framework of the adiabatic theorem, this implies that there exists at least one value of s such that a gap closes (with increasing n) during the adiabatic evolution. Passing a vanishing gap corresponds to QPT in physical terms. In the vicinity of a QPT the system is described by its universality class which depends on the relevant couplings of the Hamiltonian. The family of Hamiltonians with the same relevant couplings presents the same behavior at the QPT and so share the same complexity when considered as adiabatic algorithms.

The relation with QPT suggests that a given algorithm (path) should not fundamentally depend on "small details" of this path but rather on some relevant features near the QPT. Indeed, since the smallest gap arises at the QPT point (and vanishes with n), if we deform the Hamiltonian path maintaining the QPT point unchanged, the computational complexity will still be dominated by the vicinity of the QPT point. This is why a simple interpolation scheme ($H(s) = (1-s)H_0 + sH_P$) can, a priori, be used. In that case, given H_P, the choice of the path is then reduced to the choice of H_0. Note however, as cited above (ref. [101]), that subtle choice of functions of the adiabatic parameter s with respect to time can lead to substantial speedup. The effect of choosing paths other then linear interpolations was also studied in [102].

9.1.2 The Algorithm

The output of the adiabatic computation is the ground state of the final Hamiltonian H_P. We build such a Hamiltonian by attributing to each possible classical configuration x_i, between the $N = 2^n$ possible ones, a real value ε_i (energy) that measures how well the problem is satisfied by the string of bits x_i. If x_i is a solution of the problem we set $\varepsilon_i = 0$, otherwise ε_i takes a non zero value, usually based on the problem statement (for example for the 3-SAT problem, ε_i is the number of clauses violated by the string x_i). The problem Hamiltonian reads

$$H(s=1) = H_P = \sum_i \varepsilon_i |i\rangle\langle i|, \tag{9.1}$$

where $|i\rangle$ runs over the $N = 2^n$ states in the computation basis which we take to be the tensor product of the individual eigenstates of σ_z for a two level system. If the physical system remains in its ground state, the final output corresponds to the minimization of

the energy ε_i as a function of i. For sake of simplicity we take H_0 to be diagonal in the x basis. Concerning the s parameter, we assume through this chapter that it is a simple affine function of the time such that $s(0) = 0$ and $s(T) = 1$. As said above, some authors have proposed to speed up the adiabatic evolution far from the QPT point leading to an efficient gain for the total computational time (see for example the work or Roland and Cerf on the Grover algorithm case [101]).

9.2 The Model

In most of the previously published works on AQC, two different prescriptions of the initial and final Hamiltonians were used. The most common is an additive Hamiltonian made of interaction terms involving few qubits (pairs and triplets). Indeed this type of problems is usually given by a set of local constrains (concerning few variables e.g. 3 for the 3-SAT problem). This additive prescription can also be used for H_0 providing that in that case the ground state can be easily prepared. The other type of Hamiltonians are projector-like ($H^2 \sim H$) [89, 92, 101], as treated also in the precedind chapter. A H_P of this type corresponds to an oracle-based problem which has two possible values of the energy: a (possibly degenerate) ground state energy whose states are the problem solutions and an excited energy for non solutions.

We are interested in studying different types of adiabatic evolutions which differ in terms of the gap scaling. For that purpose we chose a fixed initial Hamiltonian H_0 and we study a range of H_P with different gap scaling properties. Since H_0 should be easy to implement and diagonal in the x direction, the most natural choice is a simple (normalized) magnetic field interaction along the x direction:

$$H_0 = \frac{\mathbb{I}}{2} - \frac{1}{n} S_x, \tag{9.2}$$

where $S_x = \frac{1}{2}\sum_{k=1}^{n} \sigma_x^{(k)}$. We aim to present a simplified model of adiabatic computation by using an Hamiltonian $H(s)$ which is solvable, while displaying some of the features which will eventually be found in the more realistic case, namely the spectrum diagonal in the z basis for $H(s = 1)$, and a quantum phase transition at some intermediate value s_c. We choose a hermitian operator h_p with k spin interaction terms of the form of the following tensor product

$$h_p \;=\; \otimes_{i=1}^{n}(\mathbb{I}^i + p\sigma_z^i), \tag{9.3}$$

where i denotes the qubit. It is clearly a sum of k-spin interaction terms (k ranging from 1 to n), whose strength depends on p. Introducing the total spin $S_z = \frac{1}{2}\sum_{i=1}^{n} \sigma_z^i$, and using

the identity $e^{\alpha\sigma_z} = \cosh(\alpha) + \sinh(\alpha)\sigma_z$, h_p can be written as

$$h_p = (1-p^2)^{-\frac{n}{2}} e^{2\tanh^{-1}(p)S_z}. \tag{9.4}$$

Finally, introducing $\alpha = n\tanh^{-1}(p)$, we rescale h_p into H_P in the following form

$$H(1) = H_P(\alpha) = \frac{e^{\alpha\mathbb{I}} - e^{2\frac{\alpha}{n}S_z}}{2\sinh(\alpha)}. \tag{9.5}$$

Note that the n factor in the definition of α is introduced to obtain an Hamiltonian H_P such that nH_P is an extensive operator.

The ground state of this Hamiltonian is $|w\rangle = \otimes_{k=1}^{n}|0\rangle$ which has zero energy. The mth excited states correspond to a state with m 1s having a binomial degeneracy $\frac{n!}{(n-m)!n!}$ for any finite value of α and whose energy depends on α (see below). For $\alpha \to \infty$ the Hamiltonian is proportional to a projection operator:

$$H_P(\infty) = (\mathbb{I} - |w\rangle\langle w|), \tag{9.6}$$

and all the excited states have energy equal to one. The final Hamiltonian obtained this way is the Grover-like unsorted data base searching considered in [92, 87] and [101]. The limit $\alpha \to 0$ decouples the qubits and $H(s)$ can be written as a sum of independent single qubit Hamiltonians:

$$H(s, \alpha \to 0) = \frac{1}{n}\sum_{k=1}^{n}(1-s)\frac{\mathbb{I} - \sigma_x^{(k)}}{2} + s\frac{\mathbb{I} - \sigma_z^{(k)}}{2}, \tag{9.7}$$

which corresponds to a trivially separable problem that can be solved by parallelizing single qubit problems.

Note that, although the above H_p ground state has a particular simple form, the properties described below would apply to any Hamiltonian obtained from $H(s)$ under unitary transformations. Suppose a given problem has a solution corresponding to the ground state $|w(J)\rangle = \otimes_{k=1}^{n}|J_k\rangle$, where $J_k \in \{0,1\}$, and the same energies and degeneracies as the H_P described above. In this case by performing the unitary transformation:

$$U = \bigotimes_k (\sigma_x^{(k)})^{J_k} \tag{9.8}$$

to $H(s)$, H_0 remains invariant and the ground state of H_P is changed to $|w(J)\rangle$. Since U is unitary the gap scaling nature and the energy spectrum stay invariant. So, upon studying the particular form of H_P (9.5), we have access to the gap behavior of problems which can have the whole set of possible 2^n ground states i.e. solutions. The advantage of $H_P(\alpha)$ as

a representant of this class is that it is symmetric under qubit permutation and so it can be written as a function of the total spin $S_a = \frac{1}{2}\sum_k \sigma_a^{(k)}$ for $a = x, y, z$. Moreover since H_0 and $H_P(\alpha)$ commute with $S^2 = \sum_a S_a^2$ and the ground state of H_P has maximal value for the total spin $j = \frac{n}{2}$, the whole evolution will take place in this maximal spin sector spanned by the Dicke basis: $\{|\frac{n}{2}, i\rangle\}_{i=-\frac{n}{2}}^{\frac{n}{2}}$, where the two quantum numbers stand for the value of the total spin ($j = \frac{n}{2}$) and the spin projection along the z axes. All the other spin sectors can be disregarded because they are not coupled by the adiabatic evolution [86].

9.2.1 Density of states

As explained above the complexity of the adiabatic evolution is related to what happens near the QPT; it is nevertheless interesting to describe the spectral properties of $H(s)$ for the extremal values of s (equal to zero and one). The density of states as a function of the energy for $s = 0$ and $s = 1$ can be given analytically for large n. For $s = 0$, considering the binomial degeneracy of each level, the density of states writes:

$$\mathcal{N}_{s=0}(\omega)d\omega = \frac{2n}{\pi} e^{-2n(\omega-\frac{1}{2})^2} d\omega, \tag{9.9}$$

where $\mathcal{N}_s(\omega)d\omega$ is the total number of levels between ω and $\omega + d\omega$. For the case $s = 1$ one starts by remarking that the energies ω_m in the maximal spin sector are given by:

$$\omega_m(s=1) = \frac{e^{\alpha} - e^{\alpha(2\frac{m}{n}-1)}}{2\sinh\alpha}, \tag{9.10}$$

where m is the level labeling $m = 0, ..., n$. For large n one can invert this relation and obtain the energy density for the maximal spin sector:

$$\mathcal{N}_{s=1,S=\frac{n}{2}}(\omega)d\omega = \frac{1}{\alpha\left(1 - 2\omega + \coth\alpha\right)} d\omega, \tag{9.11}$$

To get the density of states as a function of the energy for the total spectrum one has to consider the binomial degeneracy of each level:

$$\mathcal{N}_{s=1}(\omega)d\omega = \frac{2n}{\pi} \frac{e^{-2n(\frac{\alpha+\ln(e^{\alpha}-2\omega\sinh\alpha)}{2\alpha} - \frac{1}{2})^2}}{\alpha\left(1 - 2\omega + \coth\alpha\right)} d\omega. \tag{9.12}$$

The behavior of the density of states at $s = 1$ as a function of n and α is shown in Fig. 9.1. Remark that for $\alpha = 0$ one recovers the Gaussian centered at $\omega = \frac{1}{2}$ resulting from the binomial degeneracy of the separable problem. For increasing α, the density of states is more peaked toward the value $\omega = 1$ which characterizes the projector-like Hamiltonian.

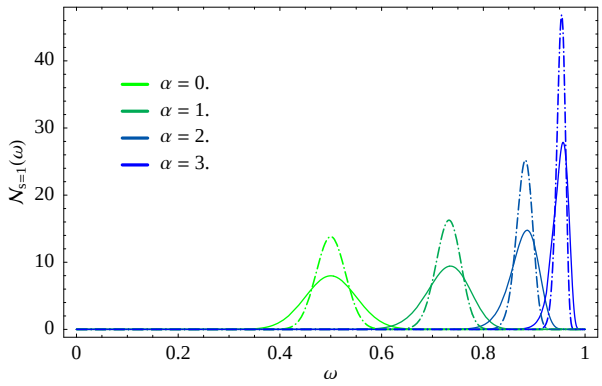

Figure 9.1: Density of states as a function of the energy for $s = 1$ for different values of α. The solid lines correspond $n = 100$ and dashed lines to $n = 300$, plotted for $\alpha \in \{0, 1, 2, 3\}$. The maximum of the curves shift to higher values of ω for increasing α.

9.3 Mean Field Approach

Since each qubit interacts in an equivalent way with all the other qubits, we expect that, in the thermodynamic limit, a mean field approach will give access to the exact ground state energy and signal quantum phase transitions whenever they occur. This is done by injecting the separable ansatz state:

$$|\Psi(\theta,\phi)\rangle = \otimes_{i=1}^{n}\left[\cos\left(\frac{\theta}{2}\right)|0\rangle + \sin\left(\frac{\theta}{2}\right)e^{i\phi}|1\rangle\right], \tag{9.13}$$

and minimizing the energy in order to determine the free parameters θ and ϕ. Doing so we can see that a first order quantum phase transition occurs for some value of $s = s_c(\alpha)(\approx 2.598)$ providing that $\alpha > \frac{3\sqrt{3}}{2}$. Fig.9.2 shows the mean value of the observable $s_x = \frac{S_x}{n}$ which presents a discontinuity along the first order quantum phase transition line in the $\alpha - s$ plane. This line ends with a second order point $(\alpha, s) = (\frac{3\sqrt{3}}{2}, \frac{2}{2+3\sqrt{6}e^{\frac{3}{2}}\sinh\left(\frac{3\sqrt{3}}{2}\right)^{-1}})$ where the values of observables are continuous non analytic functions of α and s. For $\alpha > \frac{3\sqrt{3}}{2}$, a discontinuity of $\langle S_x\rangle$ is related to the abrupt change of the ground state component with respect to the fully polarized states in the x ($|\Rightarrow\rangle = \otimes_{i=1}^{n}\left(\frac{1}{\sqrt{2}}(|0\rangle + |1\rangle)\right)$) and z directions ($|\Uparrow\rangle = \otimes_{i=1}^{n}|0\rangle$).

9.4 Numerical Analysis

9.4.1 Energy Spectrum

As predicted by the mean field approach the value of the ground state energy tends to a maximum around $s = s_c(\alpha)$ and approaches the mean field ground state energy for

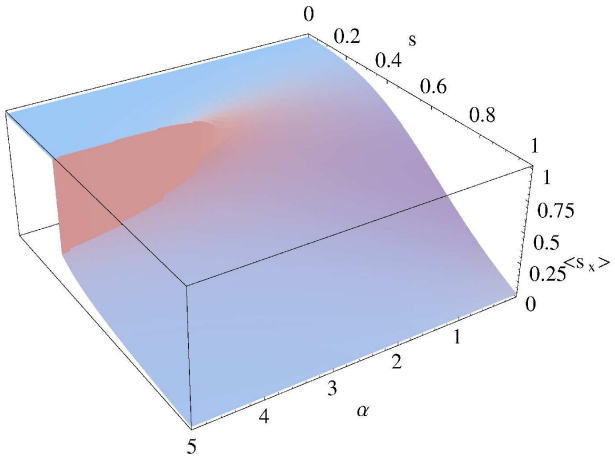

Figure 9.2: Mean value of $s_x = \frac{S_x}{n}$ plotted in the $\alpha - s$ plane.

increasing n. At the critical point there is an energy level anti-crossing and the gap vanishes as n increases. Fig. 9.3 shows the energy spectrum (in the symmetric sector) as a function of s for different values of the α parameter and n.

9.4.2 Analysis of the Two States of Lower Energy

For the cases where a phase transition exists ($\alpha > \alpha_c = \frac{3\sqrt{3}}{2}$) we now analyze the behavior of the two less energetic states, in particular their projections along $|\Rightarrow\rangle$ and $|\Uparrow\rangle$. Fig.9.4 presents a zoom of the ground state anti-crossing (at $s = s_c$) with the first excited state anteceded by some anti-crossings between more energetic states. As n increases this cascade of anti-crossings gets closer to the QPT point. Fig.9.5 shows the projections of the ground state and the first excited state along the fully polarized states $|\Rightarrow\rangle$ and $|\Uparrow\rangle$. We observe four different regions limited by the values of s where $|\langle\Rightarrow|\psi_{0/1}\rangle|^2$ or $|\langle\Uparrow|\psi_{0/1}\rangle|^2$ change abruptly. In the region $0 > s > s_1$ there are several level anti-crossings between excited states but they do not affect significantly the first two states of the spectrum (Fig.9.4); we have $|\psi_0\rangle \simeq |\Rightarrow\rangle$ (Fig.9.5) and $|\psi_1\rangle \simeq |\frac{n}{2}, \frac{n-1}{2}\rangle_x$ up to a very good approximation. At s_1 the first excited state suffers an anti-crossing with the second one and its projection along $|\Uparrow\rangle$ increases drastically but remains different from one. Fig.9.6 shows the projections onto the Dicke basis of the ground state immediately after the anti-crossing and of the first excited state immediately before the anti-crossing ($s = s_c$). At $s = s_c$ the transfer of components between the ground state and the first excited state is clearly manifested. For $s > s_c$ the ground state increases slowly its projection along $|\Rightarrow\rangle$ and at s_2 the first excited state experiments another anti-crossing (Fig.9.4), increasing drastically his projection along $|j = \frac{n}{2}, m = \frac{n}{2} - 1\rangle$. For $s > s_2$ there are no anti-crossings and the states increase slowly their projection along the ground and first-excited states: $|\Uparrow\rangle$ and $|j = \frac{n}{2}, m = \frac{n}{2} - 1\rangle$.

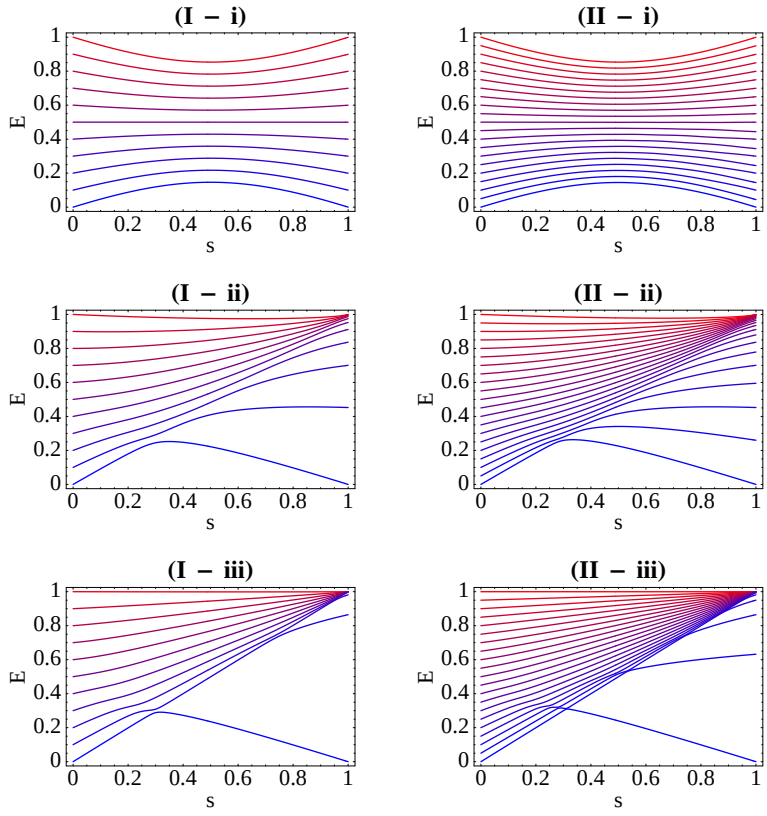

Figure 9.3: Energy levels as a function of s computed for different values of n and α. The series I presents the energy levels for $n = 10$ and $\alpha \in \{0, 3, 10\}$ respectively for $\{i, ii, iii\}$. The series II presents the energy levels for $n = 20$, the values of α are labeled as before.

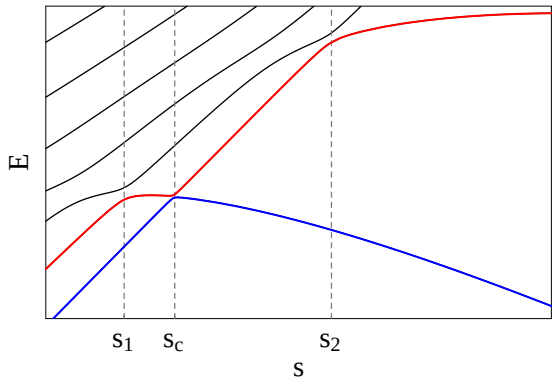

Figure 9.4: Different regions where the ground state (lower curve, blue) and the first excited state (red) undergo level anti-crossings, plotted for $n = 30$ and $\alpha = 5$.

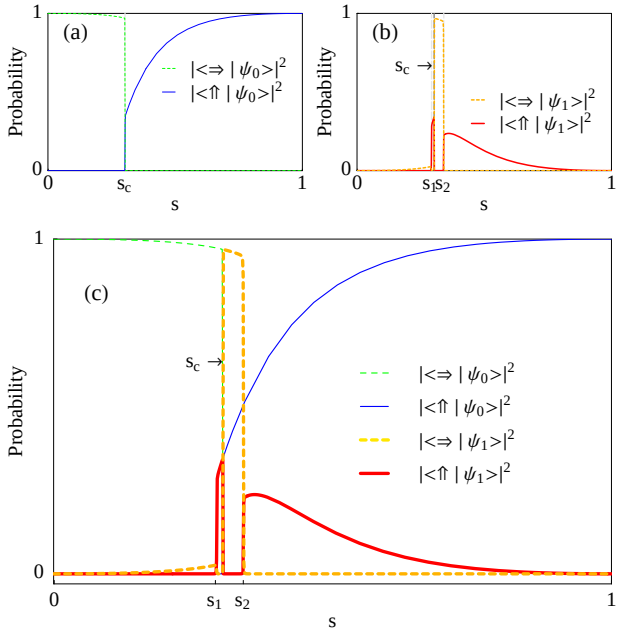

Figure 9.5: Square of the modulus of the inner product of the two lowest levels with the states $|\Rightarrow\rangle$ and $|\Uparrow\rangle$ which are the ground state of $H(s)$ for $s = 0$ and $s = 1$ respectively. Here plotted for $n = 50$ and $\alpha = 5$. (a) and (b) present respectively the evolution of the ground and first excited states projections along the Hamiltonian path. (c) combines (a) and (b), and clearly displays the exchange between these two states at $s = s_c$.

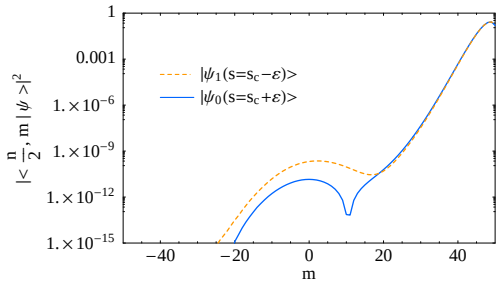

Figure 9.6: Square modulus of the projections of the ground state immediately after the anti-crossing and of the first excited state immediately before the anti-crossing along the Dicke basis, plotted for $n = 100$ and $\alpha = 5$. Note that the a logarithmic scale is used.

9.5 Beyond the Mean Field Approximation

In order to characterize further the system let us now look at the gap scaling (with n) near the QPT and the ground state entanglement content as measured by the concurrence [103]. To study the quantum fluctuations around the mean field solution we can for instance apply

a method described in [59] which uses the Holstein-Primakoff mapping from a given spin sector characterized by the value of S^2 and the algebra of boson operators, obtaining a interacting boson Hamiltonian which can be expanded in powers of $\frac{1}{n}$. Using this method one is able to compute the ground state concurrence in the $\alpha - s$ plane and to predict the gap behavior based on the universality class of the model.

9.5.1 Holdstein-Primakov Mapping - Scaling of the Gap

The Holdstein-Primakov (H-P) transformation maps the $su(2)$ generators into non-linear functions of boson operators a and $a^\dagger$ (with $[a, a^\dagger] = 1$) preserving their commutation relations,

$$S_z = \frac{n}{2} - a^\dagger a, \tag{9.14}$$

$$S_+ = \sqrt{n - a^\dagger a}\; a, \tag{9.15}$$

$$S_- = a^\dagger \sqrt{n - a^\dagger a}. \tag{9.16}$$

This representation is well suited to capture the low energy physics of the spin-collective models, by developing the above expressions in powers of n^{-1}. The mean field approximation can be performed using this approach shifting $a \to \sqrt{n}\mu + a$ where μ is a complex parameter. The mean field energy is obtained developing the Hamiltonian in inverse powers of n and considering the leading order term which is independent of a and $a^\dagger$. μ is then computed in order to minimize the mean field energy. It can be easily interpreted by computing the mean values of the spin operators at leading order,

$$\left\langle \vec{S} \right\rangle = \left\{ \frac{(\mu + \bar{\mu})\sqrt{1 - \bar{\mu}\mu}}{2}, \frac{(\mu - \bar{\mu})\sqrt{1 - \bar{\mu}\mu}}{2\mathrm{i}}, \frac{1}{2} - \bar{\mu}\mu \right\}. \tag{9.17}$$

This relations permit to make the parallel with the angles ϕ and θ considered for the ansatz state employed in the mean field approach.

In order to study corrections to the mean field approximation we have to consider further terms in the expansion of the Hamiltonian. The next to leading term of order n^{-1} gives a quadratic bosonic Hamiltonian

$$H = n^{-1} \left[\frac{\bar{\delta}_1}{2} a^\dagger a^\dagger + \frac{\delta_1}{2} aa + \delta_0\, a^\dagger a \right] + O(n^{-2}), \tag{9.18}$$

with

$$\delta_0 = \frac{(s-1)\mu\left(3\mu^2 - 4\right)}{4\left(1 - \mu^2\right)^{3/2}} - s\alpha\left(2\alpha\mu^2 - 1\right)\mathrm{csch}(\alpha)e^{\alpha - 2\alpha\mu^2}, \tag{9.19}$$

$$\delta_1 = \bar{\delta}_1 = \frac{(s-1)\mu\left(\mu^2 - 2\right)}{4\left(1 - \mu^2\right)^{3/2}} - 2s\alpha^2\mu^2\mathrm{csch}(\alpha)e^{\alpha - 2\alpha\mu^2}. \tag{9.20}$$

where the minimal energy conditions lead to a real value of μ satisfying: $e^{2\alpha\mu^2}(s-1)\,(2\mu^2-1) = 2e^{\alpha}s\alpha\mu\sqrt{1-\mu^2}\mathrm{csch}(\alpha)$. This Hamiltonian can be diagonalized by a simple Bogolioubov transformation $a \to a\cosh(\Theta/2) + a^\dagger \sinh(\Theta/2)$ yielding

$$H_\Theta = n^{-1}\omega a^\dagger a + O(n^{-2}), \tag{9.21}$$

by a suitable choice of the parameter Θ. The low energy excitation gap is thus given by $\Delta = n^{-1}\omega = n^{-1}\sqrt{\delta_0^2 - \bar{\delta}_1\delta_1}$. However, for the second order QPT point, the Bogolioubov transformation is singular and the Hamiltonian cannot be written in the form (9.21). In order to see why that is the case we present a simple argument that helps to clarify this point. Consider the following transformation

$$\tilde{H}_1 = R_1(-\bar{\xi}_1)HR_1(\bar{\xi}_1) = n^{-1}\left[\Delta a^\dagger a + \frac{\delta_1}{2}aa\right] + O(n^{-2}) \tag{9.22}$$

with $R_1(\bar{\xi}) = \mathrm{e}^{\frac{1}{2}\bar{\xi}a^\dagger a^\dagger}$ and $\bar{\xi}_1 = \frac{\Delta-\delta_0}{\delta_1}$. Even if $R_1(\bar{\xi})$ is not unitary, the transformation conserves the spectrum of the operator H. In the case $\Delta \neq 0$ we can apply another simple transformation $R_2(\xi) = \mathrm{e}^{\frac{1}{2}\xi aa}$ to fully diagonalize the Hamiltonian obtaining, as before,

$$\tilde{H}_2 = R_2(-\xi_2)HR_2(\xi_2) = n^{-1}\left[\omega a^\dagger a\right] + O(n^{-2}) \tag{9.23}$$

with $\xi_2 = -\frac{\delta_1}{2\omega}$. If $\Delta = 0$, $\tilde{H}_1$ commutes with R_2 and thus can not be brought into the form (9.23); moreover in this case the spectrum of the $\tilde{H}_1$ is proportional to the spectrum of the operator aa which is continuous, yielding to zero energy excitation. However for finite values of n the excitation gap is non-zero translating the fact that higher order terms in the n^{-1} expansion of the Hamiltonian must to be taken into account. The expansion of the Hamiltonian up to order n^{-2} can then be then brought to the form

$$\tilde{H} = -\frac{n^{-1}}{4m}\,aa + n^{-2}4\lambda\; a^\dagger a^\dagger a^\dagger a^\dagger + ..., \tag{9.24}$$

using a sequential series of transformations $R_k = \mathrm{e}^{-\xi_k\, n^{k/2}\, b_1 \ldots b_k}$, where $b_1 ... b_k$ stands for a string of $b_i = a^\dagger, a$ of maximal length 4. For this model the expression of m and λ can be obtained analytically but their expression is quite involved, here we give only their numerical values $m \simeq 1.455; \lambda \simeq 0.700$. The Hamiltonian given in Eq. (9.24) can also be transformed, by the same kind of simple operations, to the one of a quartic oscillator

$$\tilde{H} = n^{-1}\frac{p^2}{2m} + n^{-2}\lambda x^4 + ..., \tag{9.25}$$

where $[x, p] = \mathrm{i}$. The other terms of equation (9.24) and (9.25) are higher powers of n^{-1} and/or of the creation and annihilation operators and give subleading corrections on the gap behavior. In the Schrödinger representation, it is easy to see, by simply rescaling the

x variable, that the gap of the Hamiltonian Eq. (9.24) is given by $\Delta = \Delta_0 m^{-2/3}\lambda^{1/3}n^{-4/3}$, where $\Delta_0 \simeq 1.726$ is the gap of the quartic oscillator (9.25) with $m = \lambda = n = 1$.

Fig.9.7 shows the scaling of the minimun energy gap, obtained along the path $H(s)$, with n. For $\alpha < \frac{3\sqrt{3}}{2}$ the gap is proportional to $\frac{1}{n}$. This arises because of our normalization choice of the total Hamiltonian. Had we chosen a normalization in which the energy was a extensive quantity (which can be obtained by multiplying the total Hamiltonian by n) and the gap would be constant in the large n limit. This result is simply derived from the standard Holstein-Primakoff method. At the second order transition point ($\alpha = \frac{3\sqrt{3}}{2}$) the numerical computation displays a clear slope crossover toward a still algebraic exponent $\Delta \sim n^{-\nu}$ (Fig.9.7). Numerically we find ν to be close to $\frac{4}{3}$ as predicted by the simple argument given above, which is the value found previously in [59] for an also fully connected spin system but where the Hamiltonian was limited to two-body interactions. Fig. 9.8 displays the convergence of the prefactor to the one predicted by the mapping to the quartic potential. In the region where the first order QPT occurs $\alpha > \frac{3\sqrt{3}}{2}$ the gap vanishes exponentially with n. This is a general behavior for first order QPT. The gap obtained

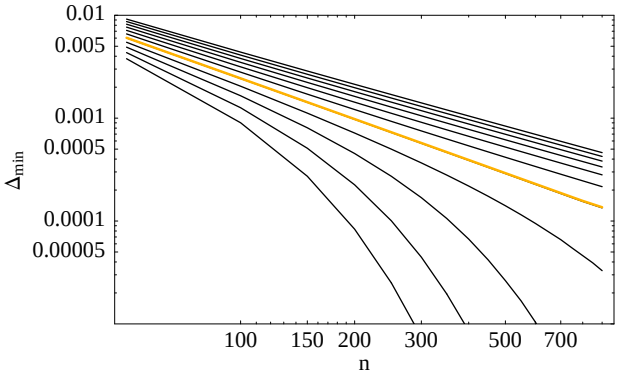

Figure 9.7: Scaling of the energy gap at the QPT point with n for different values of the α parameter. The curves range from $\alpha = 0$ to $\alpha = 3$. One observes a clear crossover at the critical value $\alpha_c = \frac{3\sqrt{3}}{2}$ (yellow) with a ν value close to $\frac{4}{3}$.

by the H-P mapping gives the energy of the "linearized" excitations around the mean field solution, in particular it does not take into account non-local aspects of the phase space, this is important in the case of degenerate mean-field minimum where, even if the local excitations have finite values, the true gap of the system depends on non-local properties of the Hamiltonian and is exponentially decreasing with n.

9.5.2 Concurrence

We measure the entanglement contend of the ground state by computing the concurrence of the $(n-2)$-qubit traced density matrix. The entanglement is encoded in the finite size

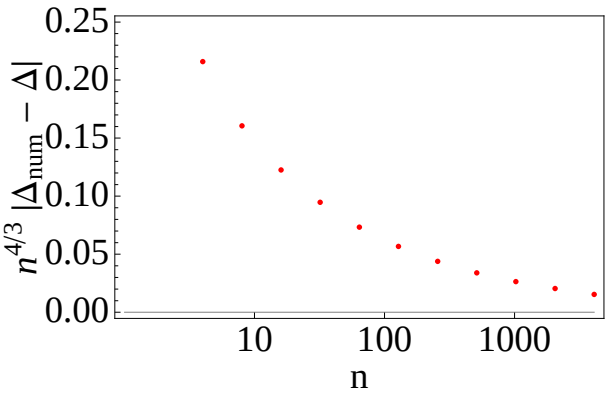

Figure 9.8: Convergence of the numerical computed gap $\Delta_{\rm num}$, at the second order QPT point, to the one of an anharmonic oscillator with a pure quartic potential given by $\Delta = \Delta_0 m^{-2/3}\lambda^{1/3}n^{-4/3}$.

corrections so the quantity to study is the rescaled concurrence $C_R = (N-1)C$ which is usually non trivial in the thermodynamic limit near a QPT. This quantity can be computed, for the symmetric spin sector, as a function of the mean values of the spin operators S_i, S_i^2, $i = x, y, z$, [104]. In the present case the real nature of the density matrix leads to the simple expression: $C_R = 1 - \frac{4\langle S_y^2\rangle}{n}$: see [105]. Fig.9.9 displays the concurrence computed in the $\alpha - s$ plane. Note that along the first order line the concurrence is discontinuous in s, a feature that, to our knowledge, was not observed for other models. At the second order transition point this quantity presents a cusp like form as in the simple LGM model [19] ; the numerical analysis of the singularity strongly suggests that, as in the LGM model, the rescaled concurrence behaves as $1 - C_R \sim n^{-\mu}$ with $\mu = \frac{1}{3}$.

9.5.3 Entropy

Entropy of entanglement is a measure of the nonseparability of pure quantum states of a bipartite system $(A+B)$. It is obtained considering the density matrix of one of the subparts after having traced out the degrees of freedom of the other $\rho_A = \mathrm{Tr}_B(|\Psi_{A+B}\rangle\langle\Psi_{A+B}|)$, and it coincides with von Neuwman entropy for a density matrix $E = -\mathrm{Tr}_A(\rho_A \ln \rho_A)$.

In the present case we consider the entropy of entanglement between two subsystems of spins 1/2 of sizes n_A and n_B $(n_A + n_B = n)$. In order to compute this quantity we follow [54] and write the spin operators of the symmetric sector as the sum of operators of the two subsystems

$$S_i = S_i^{(A)} + S_i^{(B)}, \quad i = x, y, z. \tag{9.26}$$

where spin (A) and (B) are obtained by summing, respectively, $n_A = \epsilon n$ and $n_B = (1-\epsilon)n$ spins 1/2.

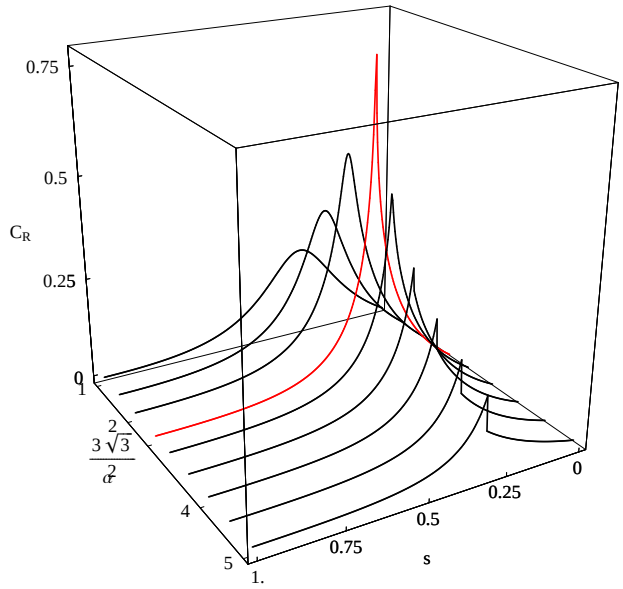

Figure 9.9: Reduced concurrence in the thermodynamic limit obtained, by tracing over $n-2$ arbitrary qubits, as a function of α and s. For $\alpha > \alpha_c$ the concurrence presents a discontinuity which increases with α.

Appling the H-P mapping to both (A) and (B) spins, using two sets boson operators $\{a, a^\dagger\}$ and $\{b, b^\dagger\}$, yields to a two boson Hamiltonian. The mean field step follows, as before, shifting the operators by a constant factor

$$a \to \sqrt{n_A}\mu_A + a, \tag{9.27}$$

$$b \to \sqrt{n_A}\mu_A + b. \tag{9.28}$$

The mean field energy should be minimized in order to μ_a and μ_b. Moreover, since we are interested in the symmetric sector we should set $\mu_a = \mu_b = \mu$. Performing the H-P mapping and developing the Hamiltonian in inverse powers of n one obtains, at leading order, a quadratic boson Hamiltonian

$$H = \sum_{i,j} t_i\, \omega_{i,j}\, t_j \tag{9.29}$$

with $t_i \in \{a, a^\dagger, b, b^\dagger\}$, fully diagonalizable by a Bogoulibov Transformation $c = \sum_i w_{c,i} t_i$; $d = \sum_i w_{d,i} t_i$. In the Bogouliubov transformed basis the ground state density matrix writes simply $|0_c, 0_d\rangle\langle 0_c, 0_d| = \mathrm{e}^{\mathrm{i}R}\ |0_a, 0_b\rangle\langle 0_a, 0_b|\ \mathrm{e}^{-\mathrm{i}R}$. Since the Hamiltonian is quadratic the R operator is a quadratic Hermitian operator in the initial boson operators a and b. In order to compute the trace we write $|0_a, 0_b\rangle\langle 0_a, 0_b| = \lim_{\beta\to\infty} Z(\beta)^{-1}\mathrm{e}^{-\beta a^\dagger a}$ where $Z(\beta) = \frac{e^\beta}{e^\beta - 1}$

is the partition function of the Harmonic oscillator. The density matrix for the A subpart writes as

$$\rho_A = \lim_{\beta\to\infty} Z(\beta)^{-1}\ \mathrm{Tr}_B(\mathrm{e}^{\mathrm{i}R}\mathrm{e}^{-\beta a^\dagger a}\mathrm{e}^{-\mathrm{i}R}). \tag{9.30}$$

Note that all operators involved in the trace are quadratic implying that the resultant density matrix is also an exponential of a quadratic form of a and $a^\dagger$: $\rho_A = \mathrm{e}^{\kappa_2 a^\dagger a^\dagger + \bar{\kappa}_2 a^\dagger a^\dagger + \kappa_1 a^\dagger a + \kappa_0}$. By Wick's theorem this quantity is fully characterized by its first moments:

$$\langle O\rangle \quad = \quad \mathrm{Tr}_A(\rho_A O) = \langle 0_c, 0_d|O|0_c, 0_d\rangle, \tag{9.31}$$

with $O \in \{a^\dagger a^\dagger, a^\dagger a, aa\}$ and the fact that $\langle 1\rangle = 1$. Diagonalizing the quadratic form and computing the trace on its diagonal basis one obtains

$$S = u\coth^{-1}(u) + \log\left(\frac{1}{2}\sqrt{u^2-1}\right), \tag{9.32}$$

with $u = \sqrt{(2\langle a^\dagger a\rangle + 1)^2 - 4\langle a^\dagger a^\dagger\rangle^2}$, where we used the fact that for this particular case $\langle a^\dagger a^\dagger\rangle = \langle aa\rangle$. Fig. 9.5.3 displays the entropy at the thermodynamic limit as a function of s for different values of the α parameter for $n_A = n_B = 1/2$. As for the concurrence this quantity presents a discontinuity along the first order QPT line. At the second order QPT point the entropy diverges logarithmically as its was also found in [54] for the LMG model.

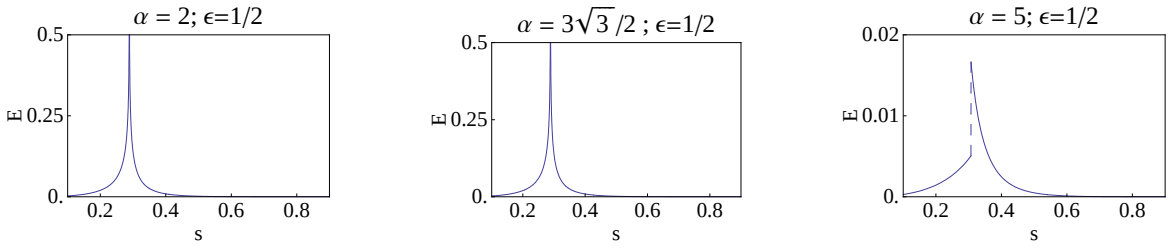

Figure 9.10: Entropy in the thermodynamic limit obtained, by tracing over $n/2$ arbitrary qubits ($\epsilon = 1/2$), as a function of α and s. For $\alpha > \alpha_c$ the entropy presents a discontinuity which increases with α.

9.6 Conclusion

In this chapter we discuss in detail an Hamiltonian evolution which should be viewed as a toy model for adiabatic computation. Indeed the phenomenological properties of this

system correspond to what is usually expected in more realistic implementations: a Hamiltonian based on spin-spin interactions, a final Hamiltonian ($s = 1$) diagonal in the computational basis and a non trivial behavior for some intermediate values of s corresponding to a QPT. An interesting feature of our model is that it is build on a two dimensional parameter space which allows to trigger the Hamiltonian path form a trivial one (without QPT) to a regime where a first order QPT occurs, separated by a second order phase transition. The above phase space may serve as a template for more realistic cases. Given a classical computation problem the precise H_P formulation and the choice of the initial Hamiltonian H_0 should result from an optimization process. A qualitative knowledge of the phase space is required for that analysis (in terms of the topology of the first and second order phase transition manifolds). In particular an heuristic point of view would lead to looking (in the phase space) for second order QPT to built an optimum Hamiltonian path.

Chapter 10

Dynamical Properties Accross a Quantum Phase Transitions in the Lipkin-Meshkov-Glick Model

As already discussed above, it is of high interest, in the context of Adiabatic Quantum Computation, to better understand the complex dynamics of a quantum system subject to a time-dependant Hamimtonian, when driven accross a quantum phase transition. We present here such a study in the Lipkin-Meshkov-Glick model with one variable parameter. We first display numerical results on the dynamical evolution accross the LMG quantum phase transition, which clearly shows a pronounced effect of the spectral avoided level crossings. We then derive a phenomenological (classical) transition model, which already shows some closeness to the numerical results. Finally, we show how a simplified quantum transition model can be built which strongly improve the classical approach, and shed light on the physical processes involved in the whole LMG quantum evolution. From our results, we argue that the commonly used description in term of Landau-Zener transitions is not appropriate for our model.

10.1 Introduction

Under a continuous change of the Hamiltonian parameters, a quantum system, initially in its ground state, can undergo transitions to excited states. This point was already studied in the early days of quantum mechanics, with the celebrated analysis of the two level case by Landau[106] and Zener [107]. Here we first display some numerical results on the dynamical evolution accross the LMG quantum phase transition with two very different pattern whenever the critical point is reached from one side and another of the QPT. We then write down a phenomenological (classical) transition model, which already shows some closeness to the numerical results. Finally, we show how a simplified quantum transition model can be built which strongly improve the classical approach, and shed light on the physical processes involved in the whole LMG quantum evolution This question is clearly of interest in the Adiabatic Quantum Computation context. We shall describe below how the two parts of the standard LMG model will contribute to H_0 and H_P, and

enter separately in the definition of the time-dependant Hamiltonian $H(t)$,

$$H(t) = (1 - \frac{t}{T})H_0 + \frac{t}{T}H_P \tag{10.1}$$

with t the physical time, and T the total evolution time. In the following, we shall use $s = t/T$, with $s \in [0, 1]$.

One faces here the interesting, although expected, picture that it is not the ground state itself (for $s = 1$) that characterizes the problem complexity, but the nature of the process, in parameter space (for $s < 1$). This should be related to the already noticed strong relationship between AQC and Quantum Annealing problems, well studied in the past years in the field of complex system (e.g. spin glasses) [108].

It is therefore of high interest to study, in the transition region, the dynamical and spectral properties in the lower part of the spectrum. In particular, one should not only focus on the first excited eigenstate coming close to the ground state, but in fact to a whole set of excited levels. This is in particular expected whenever the ground state nature is drastically changing, since its new decomposition is mainly weighted by the states for which avoided crossings appear along the adiabatic process. So the state dynamical evolution has to be thought as a complex transition cascade, rather than independant Landau-Zener (LZ) processes. Therefore, despite its great success in other systems, the LZ theory, in particular its ability to calculate the transitions between quantum states, may not be used in the present AQC case, or be severely corrected [109, 110, 111, 112]. It should be stressed in addition that LZ theory is intrinsically non-adiabatic, which suggest, for the AQC slow evolution processes, to go back to more standard adiabatic analyses[86].

To get a better understanding of these processes, we propose here to study the dynamical properties accross the quantum phase transition in the Lipkin-Meshkov-Glick model, a simple (solvable) model which exhibits some of the expected features of AQC hamiltonians, and whose spectral properties have been studied into large details in the first part of the present manuscript.

The LMG model describes a set of N spins $\frac{1}{2}$ mutually interacting through a XY-like Hamiltonian and coupled to an external transverse magnetic field h. This Hamiltonian H can thus be expressed in terms of the total spin operators $S_\alpha = \sum_{i=1}^{N} \sigma_\alpha^i/2$ where the σ_α's are the Pauli matrices:

$$H = -\frac{1}{N}\left(\gamma_x S_x^2 + \gamma_y S_y^2\right) - h\, S_z, \tag{10.2}$$

In the following, we only consider the maximum spin sector $S = N/2$, with N even and $N + 1$ levels. Although many different methods have been used to study its excitation properties, the richness of the full spectrum has only be revealed quite recently by means of numerical diagonalizations [11, 70], and then, at the thermodynamic limit, in an analytical form [14] (see chapter 3). Of interest here is the determination of the so-called "exceptional points" in the density of states, where the density of states is singular and the

level separation vanish with N. These points gather, as N tends to ∞, on a curve which we call here the "critical gap curve" (CGC).

Here, for sake of simplicity, we set $\gamma_y = 0$; it is clear that, up to a global reparametrization, the Hamiltonian only depends on the ratio between γ_x and h. To express this Hamiltonian in the form given by equation (10.1), we write $\gamma_x = s$, $h = 1 - s$, which leads to $H_0 = -S_z$ and $H_P = -S_x^2/N$

The energy levels as a function of s are displayed in figure 10.1 for $N = 20$. At the thermodynamic limit, this system undergoes a second order quantum phase transition for $s = 1/2$, whose effect is already visible with $N = 20$, in terms of levels pinching. The locus of avoided crossing levels appears very close to a straight line (exact CGC for infinite N) starting at the QPT for $s = 0.5$, and $E/N = -0.5$, and reaching $E = 0$ for $s = 1$.

In later plots, we shall use the (normalized to one) integrated density of states x, in the range $[0, 1]$, instead of the energy. The CGC still has a simple expression, $x_c(s)$, which reads

$$x_c(s) = 1 - \frac{4}{\pi} \cot^{-1}\left(\frac{\sqrt{s} + \sqrt{2s-1}}{\sqrt{1-s}}\right) - \frac{2}{\pi s}\sqrt{(1-s)(2s-1)} \tag{10.3}$$

for $s \in [0.5, 1]$

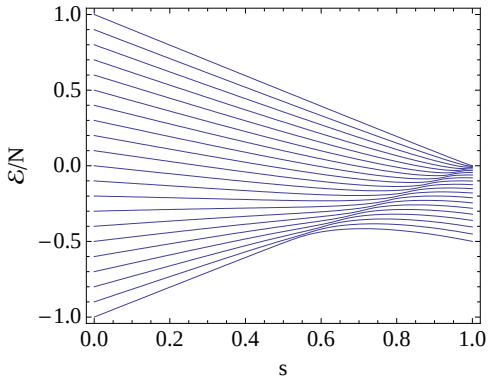

Figure 10.1: Spectrum of the "s"-dependant Lipkin-Meshkov-Glick model for $N = 20$, with 21 levels.

In the following, we first display some numerical results on the dynamical evolution accross the LMG quantum phase transition, with two very different pattern whenever the critical point is reached from one side and another of the QPT. We then write down a phenomenological (classical) transition model, which already shows some closeness to the numerical results. Finally, we show how a simplified quantum transition model can be built which strongly improves the classical approach, and shed light on the physical processes involved in the whole LMG quantum evolution

10.2 Dynamical evolution : numerical results

10.2.1 Forward evolution

We numerically solve the dynamical (arbitrarily called "forward") evolution, proceeding as follows. The initial state is the ground state corresponding to the $s = 0$ Hamiltonian. The total evolution time T is a multiple of a fixed time interval ΔT, during which the Hamiltonian parameters are kept fixed and the quantum evolution is computed by mean of a standard second order discretization method. The final state, after ΔT, serves as the intial state for the next step, with (slightly) varied Hamiltonian parameters. Therefore, the larger the T value, the smaller the effective Hamiltonian variations from one step to the next, and therefore the closer to an adiabatic evolution. Another parameter is N, the system size. Increasing N decreases the gaps, which eases the transitions to excited states. Computations are done here with $N = 50$ and three T values, corresponding qualitatively to fast ($T = 1$), medium ($T = 50$) and slow ($T = 100$) evolutions.

The levels occupancy, as a function of s, are displayed in Figure 10.2 (upper plots). Also shown is the CGC curve, in order to track the role of the gap closing phenomenon in the quantum evolution.

As can be clearly seen, a common feature of these evolutions is that the system almost remains in its ground state before reaching the quantum phase transition region.

Then, not only do the quicker evolutions drive the system to excited states transitions, but this evolution is clearly controlled by the position of the avoided crossings, as marked by the critical gap curve.

As expected, for slower evolutions (larger T), the ground state is not completly depleted, its population oscillates with time (as seen on the figure) and eventually stabilizes (see for example Ref. [113]).

10.2.2 Backward Evolution

The above observation that the whole spectrum influences the overall quantum state evolution, together with the fact that the LMG spectrum is far from being symmetrical (see figure 10.1), leads to expect a qualitatively different time evolution whenever the system is driven backward, which reads

$$H_{inv}(s) = sH_0 + (1 - s)H_P \tag{10.4}$$

The levels occupancy, displayed in Figure 10.2 (lower plots), indeed shows a very different pattern. A first explanation arises quite naturally : in the forward case, the system encounters the minimal energy gaps in an ordered sequence that allows the current wave

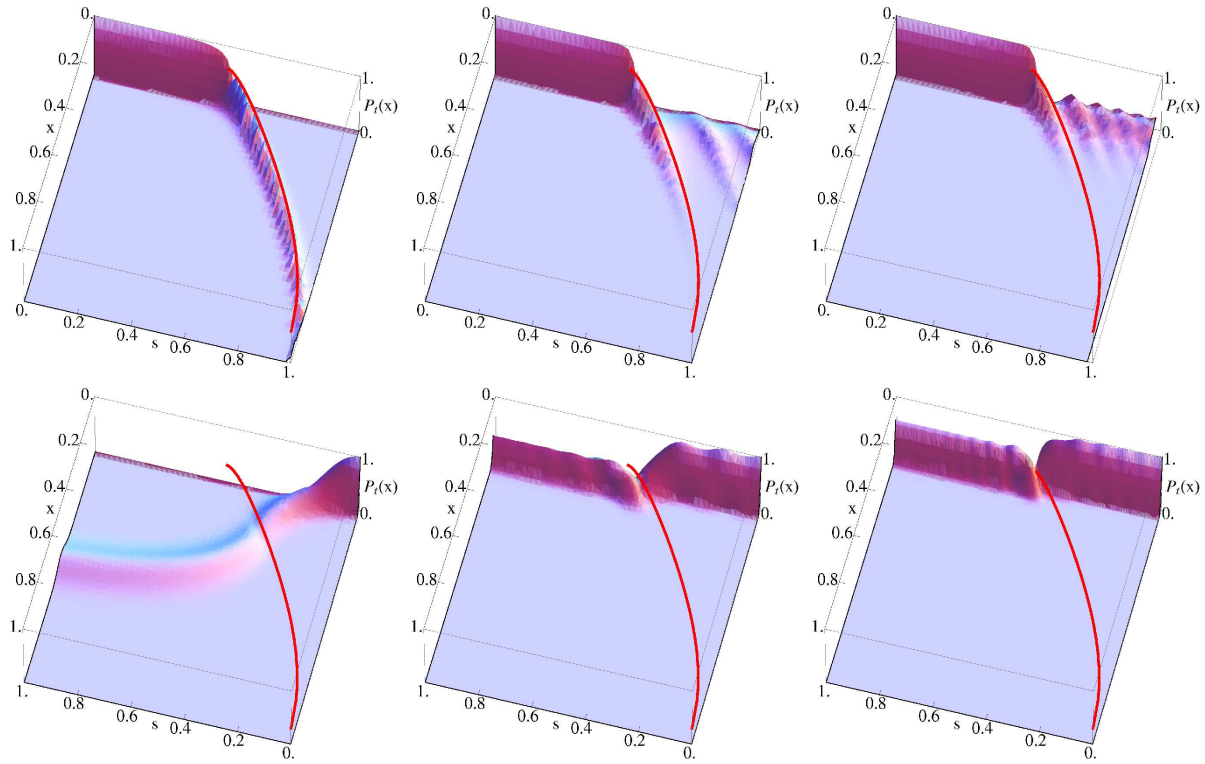

Figure 10.2: Forward and backward evolution of the level populations for a system of size $N = 50$ for different the total evolution times T. The red line is the analytical CGC curve(see text). The three upper figures correspond to forward evolution : left, fast evolution ($T = 1$); middle, intermediate speed ($T = 50$); right, slower evolution ($T = 100$). The three lower figures correspond to the backward evolution, with the same speed (T values) as the plots above

function to spread in the spectrum, with a high probability to change its eigenstate decomposition along the avoided crossings. In the latter (backward) case, once the system encounters the first small gap, and possibly leaves the ground state, it never meets again avoided crossings situations, and therefore do not proceed significantly to higher energies.

In addition, the levels population displays other qualitative features which can be explained by looking to the spectrum. In the right part of the spectrum (Figure 10.1), which is first visited in the backward evolution, the gaps are smaller with respect to those in the left part. As a consequence, for the same T value, transitions to excited states are more probable, and start occuring even before crossing the quantum phase transition (Figure 10.2 (lower left)).

Note finally (Figure 10.2) that the states population is slightly less peaked (it displays a sudden small *anti-bump*) when the CGC curve is crossed. This is again a manifestation

of the enhanced transition probability along this curve.

10.3 A phenomenological model for the quantum evolution

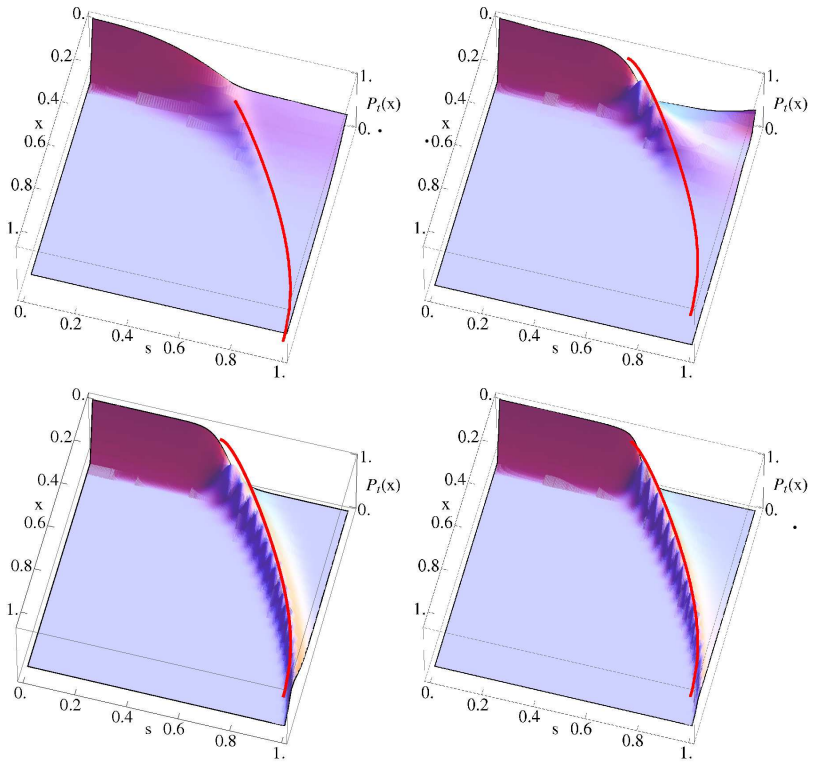

Figure 10.3: Levels population in the forward evolution case for a 20 level system and $T = 10$. Phenomenological rate equation ($T\ b = 0.01$) (up left), effective quantum chain with constant matrix element (up right), effective chain with improved matrix elements (down left), full numerical evolution (down right).

We shall be interested, in this chapter and the next one, in computing approximate values for the evolution of the probability distribution among the different states.

We call $\{|\eta_i(s)\rangle\}$ the instantaneous eigenbasis of the s-dependant Hamiltonian, $H(s)|\eta_i(s)\rangle = \epsilon_i(s)|\eta_i)(s)\rangle$, and write the current state$|\Phi(s)\rangle$, in this basis : $|\Phi(s)\rangle = \sum_i a_i(s)|\eta_i(s)\rangle$. We aim to compute the probability $P_i(s) = |\langle\eta_i(s)|\Phi(s)\rangle|^2$ for the system to be in the i-th instantaneous eigenstate at time s. We shall first suppose that transitions only occur, at the same rate, from an instantaneous eigenstate $|\langle\eta_i\rangle$ toward states $|\langle\eta_{i+1}\rangle$ and $|\langle\eta_{i-1}\rangle$. The

transition rate matrix Γ inherits a tridiagonal form, but with nevertheless $s-$dependant elements. This leads to the following differential equation for the probability

$$\begin{aligned} \dot{P}_i(s) &= \Gamma_{i+1,i}(s)P_{i+1}(s) + \Gamma_{i-1,i}(s)P_{i-1}(s) \\ &\quad -(\Gamma_{i,i+1}(s) + \Gamma_{i,i-1}(s))P_i(s) \end{aligned} \tag{10.5}$$

We choose a form for the rates $\Gamma_{i,i\pm1}(s)$ which follows a generic adiabatic prescription

$$\Gamma_{i,j}(s) = \frac{T\ b}{(\Delta^{i,j}(s))^2} \tag{10.6}$$

where $\Delta^{i,j}(s)$ is the instantaneous gap between levels i and j, calculated from the spectrum, T is the evolution time and b a (ajustable) coupling parameter .

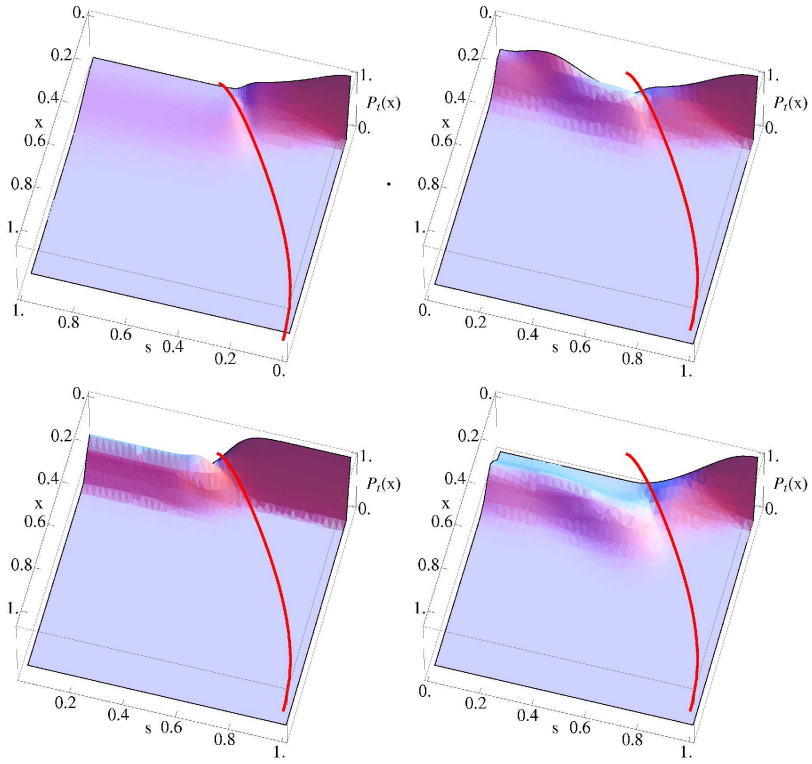

Figure 10.4: Levels population in the backward evolution case for a 20 level system and $T = 10$. Phenomenological rate equation ($T\ b = 0.01$) (upper left), effective quantum chain with constant matrix element (upper right), effective chain with improved matrix elements (lower left), full numerical evolution (lower right).

Numerical solutions of the master equation (10.5) are displayed in Figure 10.4 (up left). This (very) simple model fairly reproduces some features of the computed evolutions.

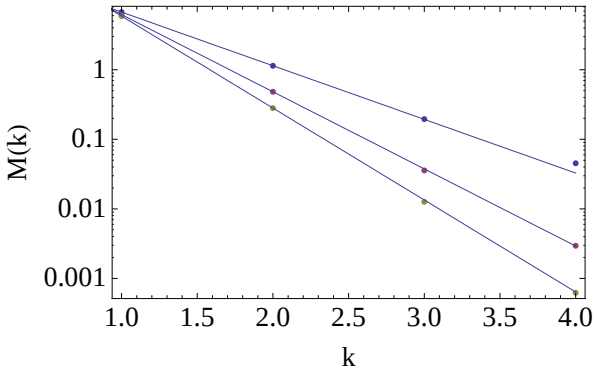

Figure 10.5: Logarithmic plot of $|\langle\eta_m(s)|\partial_s H(s)|\eta_n(s)\rangle|$ (with $n = 3$ and $m > n$) as a function of the levels distance $m - n$ and for different s (from lower to upper curves: $s = 0.75$, $s = 0.85$ and $s = 0.90$), together with linear fits

Indeed, for the forward evolution, we find the sequential transition driven by the CGC curve while for the backward evolution, a sudden transition to excited states and a subsequent saturation effect (after crossing the CGC) are recovered.

However, in the backward case for instance, this simple model fails in decribing correctly the lowest levels occupations. Indeed, the ground state remains here the most populated state during the evolution, a feature which is clearly not found in the full numerical simulations.

At this point an important remark must be done. In this phenomelogical model, we choose a transition rate (10.6) which depends on the inverse of the square of the energy gaps. This choice of an "adiabatic"-like transition rate is, in a certain sense, arbitrary. Another possible choice would have been to take $\Gamma_{i,j}(s) \propto \exp\{-b(\Delta^{i,j}(s))^2\}$ (with $b \geq 0$), which mimics the Landau-Zener transition rate. We tried to plug this type of behaviour in the rate equation, but could not find any reasonable agreement with the numerical results. This suggests that, for the present model, a generic Landau-Zener-like description is not appropriate.

10.4 Simplified quantum model for the adiabatic evolution

In order to better describe the full dynamical process, we need to improve the previous approach, and incorporate quantum effects more precisely, as follows. If the evolving quantum state is written in the instantaneous basis of $H(s)$, with the gauge choice $\langle\dot{\eta}_n(s)|\eta_n(s)\rangle = 0$, the $a_m(s)$ coefficients satisfy the equation

$$\partial_s a_m(s) = -i\epsilon_m(s)a_m(s) - \sum_{n\neq m} \frac{\langle \eta_m(s)|\partial_s H(s)|\eta_n(s)\rangle}{\Delta^{n,m}(s)} a_n(s) \tag{10.7}$$

where, as above, $\Delta^{n,m}(s)$ is the instantaneous gap between levels n and m. Note that solving equation (10.7) requires the knowledge of both the time-dependant eigenvalues and the matrix elements $\langle \eta_m(s)|\partial_s H(s)|\eta_n(s)\rangle$.

Let us further simplify this equation by using the numerically derived gaps and use an approximate form for the matrix elements. In addition, we limit the transitions from level n to neighbouring levels $n+1$ and level $n-1$, leading to an effective 1d quantum chain model. This is justified , far from the CGC curve, as can be seen in figure 10.5, where these matrix elements clearly display an exponentially decaying form with distance in the effective chain.

We then use two forms for the matrix elements. In the simplest case, we take them equal for any inter-level transition and constant with s. This already improves the previous phemenological approach, as can be seen in figure 10.3 (up-right). To further improve our model, we numerically compute the matrix elements in equation (10.7). We find that in general, for a given level n, $\langle \eta_n(s)|\partial_s H(s)|\eta_{n+1}(s)\rangle$ have a maximum near the CGC curve and then show a fast decrease. We fit this s-dependance with a Gaussian form, centered at the critical point. In addition we find that these matrix elements have *maximal* values, as a function of n, which can be well approximated by a logarithmic behaviour. We therefore write them as $\langle \eta_n(s)|\partial_s H(s)|\eta_{n+1}(s)\rangle = (a + b\log n)\exp\left(-\gamma(s - s_0(n))^2\right)$, where a, b and γ are fitted parameters and $s_0(n)$, the s value where the gap between levels n and $n+1$ is minimum, is very closely approximated from the analytic expression of the CGC curve.

The numerical simulation with this latter approximation is shown in figure 10.3 (down left). It shows a clear improvement with respect to the phenomenological approach (10.5), and even to the above constant matrix element approximation, in particular after crossing the CGC line, where the depleted population of the lowest levels is better reproduced.

Backward evolution, treated with the same approximations, are presented in figure 10.4, with similar trends as in the forward case.

Let us stress that the qualitative form of the computed evolution does not depends critically on the s dependence of the matrix elements. Analogous results are obtained within a vast range of γ coefficients and even with a different functional dependence, as long as the approximating function remains well peaked around the critical point. This confirms that the CGC drives the main feature of the dynamics; on the other hand, the absolute value of the matrix elements determine the "fine details" of the evolution, such as the ratio of the population levels.

A final remark concerns one important basic assumption of the above approaches (both phenomenological and quantum), that this system is well approximated by an effective chain with only nearest neighbour transitions between levels. This is true only *far from*

the CGC curve; near the critical point, long "distance" transitions occur. This point has been analysed in a semi-classical framework, and will be presented elsewhere [75].

10.5 Conclusion

We have studied time dependant dynamics of the Lipkin-Meshkov-Glick model driven across its Quantum Phase Transition Point. The dynamics of the quantum evolution, not restricted to the lowest level occupancy, is determined by the spectral critical gap curve, where the energy gaps vanish at the thermodynamic limit. In order to compare with the full numerical solution, we have developped simplified models for the transitions during the evolution.

First, we use a phenomenological rate equation approach, with adiabatic-like transition rates, which already recovers the role of the CGC curve in driving the main quantum evolution. But this approach misses some important features of the quantum evolution.

We then improve our description by building a quantum model, which treats the inter-level jumps as the consequence of an effective interaction between the instantaneous levels of the "s"-dependant Hamiltonian, restricted to nearest-neighbour level interactions. In a first step, this interaction is only varied following the values of the "s"-dependant gaps, which already compares better with the full numerical solution. We then further improve this effective chain model by including an approximate form for the rate of change of the Hamiltonian averaged over neighbouring levels. In that case, the main features of the quantum evolution are recovered.

Future investigations should focus on a finer description of the quantum evolution near the critical curve. In particular, long range interactions between instantaneous levels, which come close in energy near that curve, have to be taken into account.

Chapter 11

Conclusion of Part II

The aim of this part of the manuscript is to address some questions of interest for adiabatic quantum computation, in particular with respect to the characterization of the quantum phase transition expected to occur during the process. We have chosen to study simple models for that purpose, with as much as possible of analytical treatment, in order to investigate some essential features of this adiabatic model for quantum computation.

First, using a projector-like Hamiltonian as the starting Hamiltonian for a AQC algorithm, we have derived a quite general algebraic relation for the eigen-energies, leading in particular to a simple expression for the minimal gap between the ground and first excited states. This gap is given as a function of simple quantities characterizing the classical problem to be solved. We have then studied an implementation of the classical 3-SAT problem in such an adiabatic algorithm, using numerically computed quantities for the classical problem and conclude that, for this particular initial Hamiltonian, and whenever the classical case is "hard", the minimal gap vanishes exponentially with the system size.

Secondly, we discuss in details an Hamiltonian evolution which should be viewed as a toy model for adiabatic computation. According to the value of one adjustable parameter, this model displays the interesting feature of having two regimes characterized by the occurrence, or not, of a first order QPT, separated by a second order phase transition point. As said above, these singularities, and the way the gap scales with the system size, are of prime importance as far as the AQC efficiency is concerned. This model shows the importance of the phase space path followed in an AQC algorithm and suggests, from a heuristic point of view, to look for the vicinity of a second order quantum phase transition to built an optimal adiabatic path.

We have finally studied the time dependant dynamics of the LMG model driven across its quantum phase transition point. Numerical simulations using different adiabatic times show the important role of the critical gap curve, where the energy gaps vanish at the thermodynamic limit. In order to compare with the full numerical solution, we have developed simplified models for the transitions during the evolution, which treats the inter-level jumps as a consequence of an effective interaction between the instantaneous eigenstates. This allowed us to reproduce the qualitative features of the exact dynamics and, near the critical region, to put in evidence the role of the range of levels interaction.

Future investigations should focus on a finer description of the quantum evolution near

the critical curve. In particular, long range interactions between instantaneous eigenstates, which come close in energy near that curve, have to be properly taken into account. We expect to incorporate in this description the knowledge of exact expressions for the observables matrix elements, along the lines developed in the first part of this work.

Part III

Appendices

Appendix A
Details of the Semiclassical Expansion

A.1 Identities and n^{-1} Expansions

A.1.1 Development of $\mathcal{H}$

Let us consider the expression

$$\mathcal{H}[\bar{\alpha}, n^{-1}\partial_{\bar{\alpha}} + G(\bar{\alpha})] = \mathcal{L}_{[G]}\mathcal{H}[\bar{\alpha}, G(\bar{\alpha})] \tag{A.1}$$

where the symbol $\mathcal{H}$ is given by Eq. (2.21). We are going to obtain an expression for the operator $\mathcal{L}_{[G]}$ in powers of n^{-1}. In fact, since the symbol $\mathcal{H}(\bar{\alpha}, \zeta)$ has a series development in ζ, we have only to consider the development of

$$\left(n^{-1}\partial_{\bar{\alpha}} + G(\bar{\alpha})\right)^i = \mathcal{L}_{[G]}G(\bar{\alpha})^i, \tag{A.2}$$

From this it is easy to compute that

$$\mathcal{L}_{[G]} = \left[1 + \frac{\frac{1}{2}G'(\bar{\alpha})\partial_\zeta^2}{n} + \frac{\frac{1}{8}G'(\bar{\alpha})^2\partial_\zeta^4 + \frac{1}{6}G''(\bar{\alpha})\partial_\zeta^3}{n^2} + O(n^{-3})\right], \tag{A.3}$$

the explicit expression of the operator $\mathcal{L}$ can be calculated following the identity

$$\left(n^{-1}\partial_{\bar{\alpha}} + G(\bar{\alpha})\right)^i = \partial_\lambda^i\big|_{\lambda=0}\, e^{\lambda[n^{-1}\partial_{\bar{\alpha}} + G(\bar{\alpha})]} = \partial_\lambda^i\big|_{\lambda=0}\, e^{\int_0^\lambda G(\bar{\alpha} + n^{-1}x)\mathrm{d}x}, \tag{A.4}$$

where the right-hand side of the above expression permits an explicit development in n^{-1}, the final form of Eq. (A.3) follows after some algebraic manipulations.

Considering the expansions for G and $\mathcal{H}$ (2.31) and the explicit development of $\mathcal{L}$ (A.3) we have that

$$\begin{aligned}\mathcal{H}_k\left[\bar{\alpha}, G(\bar{\alpha}) + n^{-1}\partial_{\bar{\alpha}}\right] &= \left[1 + \frac{\partial_{\bar{\alpha}}G(\bar{\alpha})}{2n}\partial_\zeta^2 + ...\right]\mathcal{H}_k\left[\bar{\alpha}, G_0(\bar{\alpha}) + \frac{1}{n}G_1(\bar{\alpha}) + ...\right] \\ &= \mathcal{H}_k\left[\bar{\alpha}, G_0(\bar{\alpha})\right] + \frac{1}{n}\left\{G_1(\bar{\alpha})\partial_\zeta\mathcal{H}_k\left[\bar{\alpha}, G_0(\bar{\alpha})\right] + \frac{1}{2}\partial_{\bar{\alpha}}G_0(\bar{\alpha})\partial_\zeta^2\mathcal{H}_k\left[\bar{\alpha}, G_0(\bar{\alpha})\right]\right\} + O(n^{-2}).\end{aligned} \tag{A.5}$$

The explicit equations for G_0 and G_1 follow by identifying the coefficients of the different powers of n^{-1} in the Ricatti-like equation (2.30) with ε given in Eq. (2.31), leading to Eq. (2.32) and (2.33).

A.1.2 Relations between $\mathcal{H}$ and H

We first remark that by definition of the symbol H (2.20) and the coherent states inner product (2.18),

$$\mathrm{H}(\bar{\alpha},\alpha) = \mathcal{H}[\bar{\alpha}, n^{-1}\partial_{\bar{\alpha}} + \zeta(\bar{\alpha},\alpha)] = \mathcal{L}_{[\zeta]}\mathcal{H}[\bar{\alpha},\zeta(\bar{\alpha},\alpha)], \tag{A.6}$$

where we setted $\zeta(\bar{\alpha},\alpha) = \partial_{\bar{\alpha}}\Omega(\bar{\alpha},\alpha)$. The last equality follows from the results of the previous section. Note that $\bar{\alpha}$ and α are seen here like independent variables, i.e. we are considering the analytic continuation of the expression in both variables. By means of these, we can invert the operatorial relation (A.6),

$$\mathcal{H}[\bar{\beta},\zeta] = \mathcal{L}^{-1}_{[\zeta]}\mathrm{H}(\bar{\alpha},\alpha) \tag{A.7}$$

where we performed the change of variables $\bar{\beta} = \bar{\alpha}$ and $\zeta = \partial_{\bar{\alpha}}\Omega(\bar{\alpha},\alpha)$. $\mathcal{L}$ can be perturbatively inverted in powers of n^{-1} yielding

$$\mathcal{L}^{-1}_{[\zeta]} = 1 - \frac{\partial_{\bar{\alpha}}\zeta(\bar{\alpha},\alpha)\partial^2_\zeta}{2n} + O(n^{-2}). \tag{A.8}$$

Gathering this results with the one of the last section one obtains

$$\mathcal{H}[\bar{\beta}, n^{-1}\partial_{\bar{\beta}} + G(\bar{\beta})] = \mathcal{F}_{[G]}\mathrm{H}(\bar{\alpha},\alpha), \tag{A.9}$$

where

$$\mathcal{F}_{[G]} = 1 + \frac{\left[\partial_{\bar{\beta}}G(\bar{\beta}) - \partial_{\bar{\alpha}}\zeta(\bar{\alpha},\alpha)\right]\partial^2_\zeta}{2n} + O(n^{-2}), \tag{A.10}$$

computed at $\zeta = G(\bar{\beta})$.

If one considers the expansions of G and H given in Eq. (2.31) and the previous expansion one gets

$$\begin{aligned}\mathcal{H}[\bar{\beta}, n^{-1}\partial_{\bar{\beta}} + G(\bar{\beta})] &= \mathrm{H}_0(\bar{\alpha},\alpha) + \\ &+ \frac{1}{n}\left\{G_1(\bar{\beta})\partial_\zeta \mathrm{H}_0(\bar{\alpha},\alpha) + \mathrm{H}_1(\bar{\alpha},\alpha) + \frac{1}{2}\partial^2_\zeta \mathrm{H}_0(\bar{\alpha},\alpha)\left[\partial_{\bar{\beta}}G_0(\bar{\beta}) - \partial_{\bar{\alpha}}\zeta(\bar{\alpha},\alpha)\right]\right\} \\ &+ O(n^{-2}),\end{aligned} \tag{A.11}$$

also computed at $\zeta = G(\bar{\beta})$ and $\bar{\beta} = \bar{\alpha}$ and $\zeta = \partial_{\bar{\alpha}}\Omega(\bar{\alpha},\alpha)$. Using Eq. (2.30), Eq. (2.32) and (2.33) can, equivalently be given using the symbol H,

$$\varepsilon_0 = \mathrm{H}_0(\bar{\alpha},\alpha), \tag{A.12}$$

$$\begin{aligned}G_1(\bar{\beta}) &= -\frac{1}{2}\frac{d}{d\bar{\beta}}\log\left[\partial_\zeta \mathrm{H}_0(\bar{\alpha},\alpha)\right] + \\ &+ \frac{\varepsilon_1 - \mathrm{H}_1(\bar{\alpha},\alpha) + \frac{1}{2}\partial_\beta\partial_\zeta \mathrm{H}_0(\bar{\alpha},\alpha) + \frac{1}{2}\partial_{\bar{\alpha}}\zeta(\bar{\alpha},\alpha)\partial^2_\zeta \mathrm{H}_0(\bar{\alpha},\alpha)}{\partial_\zeta \mathrm{H}_0(\bar{\alpha},\alpha)}.\end{aligned} \tag{A.13}$$

A.2 Fluctuations around the Classical Trajectory

A.2.1 Saddle-Point Approximation

Expanding $S_{m,l}(\bar{\alpha},\alpha)$ in Eq. (4.2), using the fact that the leading order energies for the two states l and m have the same value ε_0 and the definition of $\bar{\alpha}_0$ of section 4.1.1, one gets

$$S_{m,l}(\bar{\alpha},\alpha) = \mathcal{S}_0 + n^{-1}\mathcal{S}_1 + O(n^{-2}), \tag{A.14}$$

where

$$\mathcal{S}_0 = \int_{\bar{\alpha}_0(\varepsilon_0)}^{\bar{\alpha}} G_0(\bar{\alpha}')\mathrm{d}\bar{\alpha}' + \int_{\alpha_0(\varepsilon_0)}^{\alpha} \bar{G}_0(\alpha')\mathrm{d}\alpha' - \Omega(\bar{\alpha},\alpha), \tag{A.15}$$

$$\begin{aligned}\mathcal{S}_1 = {} & \int_{\bar{\alpha}_0(\varepsilon_0)}^{\bar{\alpha}} G_1^{(l)}(\bar{\alpha}')\mathrm{d}\bar{\alpha}' + \int_{\alpha_0(\varepsilon_0)}^{\alpha} \bar{G}_1^{(m)}(\alpha')\mathrm{d}\alpha' - \\ & -\varepsilon_1^{(l)}\partial_\varepsilon\bar{\alpha}_0(\varepsilon_0)G_0[\bar{\alpha}_0(\varepsilon_0)] - \varepsilon_1^{(m)}\partial_\varepsilon\alpha_0(\varepsilon_0)\bar{G}_0[\alpha_0(\varepsilon_0)].\end{aligned} \tag{A.16}$$

The integral of Eq. (4.1) can now be written on the form

$$B = \int \frac{\mathrm{d}\bar{\alpha}\mathrm{d}\alpha}{2\pi\mathrm{i}}\, e^{n\mathcal{S}_0} F(\bar{\alpha},\alpha) \tag{A.17}$$

where F accounts all the non exponential growing terms as $n \to \infty$. Consider the change of variables

$$\bar{\alpha} = \bar{\alpha}(\phi) + \frac{\mathrm{i}\ell}{2\alpha'(\phi)}; \qquad \alpha = \alpha(\phi) - \frac{\mathrm{i}\ell}{2\bar{\alpha}'(\phi)}; \tag{A.18}$$

where $\alpha(\phi)$ is some parametrization of the classical trajectory. In the new variables, after integrating quadratic corrections in ℓ, we obtain

$$B = e^{n\mathcal{S}_0^*} \int \frac{\mathrm{d}\phi\mathrm{d}\ell}{2\pi}\, e^{\frac{n}{2}(\partial_\ell^2\mathcal{S}_0)\ell^2} F[\bar{\alpha}(\phi),\alpha(\phi)] \tag{A.19}$$

$$= e^{n\mathcal{S}_0^*} \int \mathrm{d}\phi\, \sqrt{\mathcal{M}}\, F[\bar{\alpha}(\phi),\alpha(\phi)], \tag{A.20}$$

with

$$\mathcal{M} = \frac{2\alpha'(\phi)^2\bar{\alpha}'(\phi)^2\partial_\alpha \mathrm{H}_0(\bar{\alpha},\alpha)\partial_{\bar{\alpha}}\mathrm{H}_0(\bar{\alpha},\alpha)}{-\pi\left[\alpha'(\phi)\partial_\alpha\mathrm{H}_0(\bar{\alpha},\alpha) - \bar{\alpha}'(\phi)\partial_{\bar{\alpha}}\mathrm{H}_0(\bar{\alpha},\alpha)\right]^2\partial_\alpha\partial_{\bar{\alpha}}\Omega(\bar{\alpha},\alpha)}. \tag{A.21}$$

$\mathcal{S}_0^* = -\Omega[\bar{\alpha}_0(\epsilon_0),\alpha_0(\epsilon_0)]$ is the value of $\mathcal{S}_0$ along the classical path where $\bar{\alpha}_0(\varepsilon_0)$ fixes the normalization of the states of energy ε_0.

$\mathcal{S}_1$ over the Classical Trajectory

Consider the two first terms of Eq.(A.16), with G_1 given by (A.13), one gets after some algebraic manipulations,

$$\int_{\bar\alpha_0(\varepsilon_0)}^{\bar\alpha} G_1^{(l)}(\bar\alpha')d\bar\alpha' + \int_{\alpha_0(\varepsilon_0)}^{\alpha} \bar G_1^{(m)}(\alpha')d\alpha' = -\frac{1}{2}\log\left(\frac{\partial_\alpha \mathrm{H}_0(\bar\alpha,\alpha)\partial_{\bar\alpha}\mathrm{H}_0(\bar\alpha,\alpha)}{\partial_{\bar\alpha}\partial_\alpha\Omega(\bar\alpha,\alpha)}\right)\Bigg|_{\phi_0}^{\phi} + \varepsilon_1^{(l)}\int_{\phi_0}^{\phi}\mathrm{d}\phi\,\bar\alpha'(\phi)\frac{\partial_\alpha\partial_{\bar\alpha}\Omega(\bar\alpha,\alpha)}{\partial_\alpha \mathrm{H}_0(\bar\alpha,\alpha)} + \varepsilon_1^{(m)}\int_{\phi_0}^{\phi}\mathrm{d}\phi\,\alpha'(\phi)\frac{\partial_\alpha\partial_{\bar\alpha}\Omega(\bar\alpha,\alpha)}{\partial_{\bar\alpha}\mathrm{H}_0(\bar\alpha,\alpha)}, \quad (A.22)$$

using the change of variables of section A.1.2 and the fact that the energy is constant along the classical trajectory $\frac{d}{d\phi}\mathrm{H}_0(\bar\alpha,\alpha)=0$. The last two terms, computed over the classical orbit, give simply

$$-\varepsilon_1^{(l)}\partial_\varepsilon\bar\alpha_0(\varepsilon_0)G_0[\bar\alpha_0(\varepsilon_0)] - \varepsilon_1^{(m)}\partial_\varepsilon\alpha_0(\varepsilon_0)\bar G_0[\alpha_0(\varepsilon_0)] = -\varepsilon_1^{(l)}\partial_\varepsilon\bar\alpha_0(\varepsilon_0)\partial_{\bar\alpha}\Omega(\bar\alpha_0,\alpha_0) - \varepsilon_1^{(m)}\partial_\varepsilon\alpha_0(\varepsilon_0)\partial_\alpha\Omega(\bar\alpha_0,\alpha_0). \quad (A.23)$$

Matrix Elements at Leading Order

Gathering the results of the two last sections, Eq. (4.1) writes

$$\langle\eta_m|\hat A|\eta_l\rangle \;=\; C\times e^{\Phi_{m,l}}\oint \mathrm{d}\phi\; v(\phi)\,\mathrm{e}^{\theta_{m,l}(\phi)}\;\mathcal{F}_{[G]}\mathrm{A}(\bar\alpha,\alpha)\big|_{\alpha(\phi)}\,. \quad (A.24)$$

where $\mathcal{F}_{[G]}\mathrm{A}(\bar\alpha,\alpha)\big|_{\alpha(\phi)} = \mathrm{A}[\bar\alpha(\phi),(\phi)] + O(n^{-1})$ and

$$C = c\,e^{-n\,\Omega(\bar\alpha_0,\alpha_0)}\sqrt{\frac{1}{2\pi}\frac{\partial_\alpha \mathrm{H}_0(\bar\alpha_0,\alpha_0)\partial_{\bar\alpha}\mathrm{H}_0(\bar\alpha_0,\alpha_0)}{\partial_{\bar\alpha}\partial_\alpha\Omega(\bar\alpha_0,\alpha_0)}} + O(n^{-1}), \quad (A.25)$$

$$\Phi_{l,m} = -\varepsilon_1^{(l)}\partial_\varepsilon\bar\alpha_0(\varepsilon_0)\partial_{\bar\alpha}\Omega(\bar\alpha_0,\alpha_0) - \varepsilon_1^{(m)}\partial_\varepsilon\alpha_0(\varepsilon_0)\partial_\alpha\Omega(\bar\alpha_0,\alpha_0) + O(n^{-1}), \quad (A.26)$$

$$v(\phi) = \frac{2\alpha'(\phi)\bar\alpha'(\phi)\;\partial_\alpha\partial_{\bar\alpha}\Omega(\bar\alpha,\alpha)}{\sqrt{\left[\bar\alpha'(\phi)\partial_{\bar\alpha}\mathrm{H}_0(\bar\alpha,\alpha) - \alpha'(\phi)\partial_\alpha\mathrm{H}_0(\bar\alpha,\alpha)\right]^2}} + O(n^{-1}), \quad (A.27)$$

$$\theta_{l,m}(\phi) = \int_{\phi_0}^{\phi}\frac{\partial_\alpha\partial_{\bar\alpha}\Omega(\bar\alpha,\alpha)\left[\varepsilon_1^{(m)}\partial_\alpha\mathrm{H}_0(\bar\alpha,\alpha)\alpha'(\phi) + \varepsilon_1^{(l)}\partial_{\bar\alpha}\mathrm{H}_0(\bar\alpha,\alpha)\bar\alpha'(\phi)\right]}{\partial_{\bar\alpha}\mathrm{H}_0(\bar\alpha,\alpha)\partial_\alpha\mathrm{H}_0(\bar\alpha,\alpha)}\mathrm{d}\phi + O(n^{-1}), \quad (A.28)$$

with c defined such that $\mathrm{d}\mu(\bar\alpha,\alpha) = c\,\partial_\alpha\partial_{\bar\alpha}\Omega(\bar\alpha,\alpha)\frac{\mathrm{dRe}(\alpha)\;\mathrm{dIm}(\alpha)}{\pi}$, for the spin case $c=n+1$. Note that the result is independent of the parametrization of the classical orbit.

A.2.2 Classical Dynamics

Consider the Classical Mechanics [114] given by the symplectic 2-form

$$\omega = i\,\partial_\alpha \partial_{\bar{\alpha}} \Omega(\bar{\alpha}, \alpha)\, \mathrm{d}\alpha \wedge \mathrm{d}\bar{\alpha}. \tag{A.29}$$

The equation of flow $\mathbf{g}_t$, with initial conditions $\mathbf{z}_0 = (\alpha_0, \bar{\alpha}_0)$, is given by

$$\frac{\mathrm{d}}{\mathrm{d}t}\mathbf{g}_t(\mathbf{z}_0) = \mathbf{I}(\mathrm{dH}) \tag{A.30}$$

where H is the classical Hamiltonian, d stands for the external derivative and $\mathbf{I}$ is a isomorphism between 1-forms u and 1-vectors v defined as $\omega(v, \mathbf{I}u) = u(v)$ (in a coordinate system $\omega_{ij} v^i (\mathbf{I}u)^j = u_k v^k$). In coordinates we have

$$\frac{\mathrm{d}}{\mathrm{d}\tau}\alpha(\tau) = \mathrm{i}\frac{\partial_{\bar{\alpha}} \mathrm{H}\,(\bar{\alpha}, \alpha)}{\partial_\alpha \partial_{\bar{\alpha}} \Omega(\bar{\alpha}, \alpha)}, \tag{A.31}$$

$$\frac{\mathrm{d}}{\mathrm{d}\tau}\bar{\alpha}(\tau) = -\mathrm{i}\frac{\partial_{\alpha} \mathrm{H}\,(\bar{\alpha}, \alpha)}{\partial_\alpha \partial_{\bar{\alpha}} \Omega(\bar{\alpha}, \alpha)}. \tag{A.32}$$

In the case of the semi-classical limit spin system, where $\partial_{\bar{\alpha}} \partial_\alpha \Omega(\bar{\alpha}, \alpha) = (1 + \bar{\alpha}\alpha)^{-2}$, the equations describe the motion of a particle in a sphere S^2 submeted to the potential H, and the coordinates $\{\bar{\alpha}, \alpha\}$ are obtained by stereographic projection.

A.2.3 Action-Angle Coordinates

The classical evolution in the action-angle variables are defined such that the evolution in this basis writes trivially,

$$\frac{\mathrm{d}}{\mathrm{d}\tau} I = 0, \tag{A.33}$$

$$\frac{\mathrm{d}}{\mathrm{d}\tau}\varphi(\tau) = w(I), \tag{A.34}$$

where $w(I)$ is the frequency of the motion, the 2-form writes then

$$\omega = \mathrm{d}I \wedge \mathrm{d}\varphi. \tag{A.35}$$

For an integrable system, away from critical trajectories, it is allways possible to define such variables and they can be given explicitly as [114]

$$I = \frac{1}{2\pi}\oint_{\mathcal{C}} \mathrm{i}\zeta(\bar{\alpha}, \alpha) d\bar{\alpha} = \frac{1}{2\pi}\int_\Sigma \omega \tag{A.36}$$

where $\mathcal{C}$ is the classical trajectory defined by $\mathrm{H}_0(\bar{\alpha}, \alpha = \varepsilon_0$, Σ is the area inside it. $\zeta(\bar{\alpha}, \alpha) = \partial_{\bar{\alpha}} \Omega(\bar{\alpha}, \alpha)$,defined as in section A.1.2, is the variable conjugated to $\bar{\alpha}$: $\omega = \mathrm{i}\ \mathrm{d}[\zeta(\bar{\alpha}, \alpha)\ \mathrm{d}\bar{\alpha}]$. The period of an orbit of energy ε_0 is defined by

$$T(I) = \frac{2\pi}{w(I)} = \frac{2\pi}{\partial_I \varepsilon}. \tag{A.37}$$

A.3 Mapping the LMG model onto an equivalent one-dimensional model

The density of states calculation given in this paper relies on the fact that the roots of the Majorana polynomial lie on well-defined curves in the complex plane. This result stems from the well-known wave function nodes oscillation theorem for one-dimensional systems, which arise here via a mapping of the LMG model onto the problem of a particle in a one-dimensional potential (see [16] for a review), which we summarize here. A one-to-one relation exists between the energy spectrum of the spin system and the low-lying quantum states of such a particle.

We aim to rewrite the equation for the eigenstate $\Psi(\alpha)$ as a Schrödinger equation for a particle moving in a one-dimensional potential. The procedure consists in three steps, given first for the case $\gamma_y < 0$.

1. We change H into an equivalent form such that the roots of the Majorana polynomials (nodes of the wavefunction) which are aligned on the $\mathcal{C}_1$ curve are sent onto the unit circle. This is achieved through the following unitary transformation: $\tilde{H} = \mathrm{e}^{\mathrm{i}\frac{\pi}{2}S_x} H \mathrm{e}^{-\mathrm{i}\frac{\pi}{2}S_x}$

2. The unit circle being parametrized by an angle θ, we write $\Phi(\theta) = \mathrm{e}^{-\mathrm{i}s\theta}\Psi(\mathrm{e}^{\mathrm{i}\theta})$ for $\theta \in [0, 2\pi[$.

3. Finally, we define a new function $\phi(x)$, which satisfies a one-dimensional Schödinger equation, and such that part of its spectrum is put in one-to-one correspondance with the original spin spectrum. This is achieved by setting $\Phi(\theta) = \mathrm{e}^{f[x(\theta)]}\phi[x(\theta)]$ where $f(x)$ and $x(\theta)$ are chosen to suppress the first-order derivative in the initial Eq. (3.4) for $\Psi(\alpha)$ and to set the "mass" term equal to s. The resulting Schrödinger-like equation for $\phi(x)$, describing a particle in a one-dimensional periodic potential, reads:
$$-\frac{1}{2s}\partial_x^2\phi(x) + V(x)\phi(x) = E\phi(x). \tag{A.38}$$

Following this procedure, one obtains the effective potential

$$\begin{aligned} V(x) &= \frac{1}{2\gamma_y - 2\gamma_x\ \mathrm{sn}(B|\gamma_x/\gamma_y)^2}\Big\{h(2s+1)\,(\gamma_x-\gamma_y)\,\mathrm{sn}(B|\gamma_x/\gamma_y) - \\ &\quad \left[h^2 s + (s+1)\gamma_x\gamma_y\right]\mathrm{cn}(B|\gamma_x/\gamma_y)^2\Big\}, \end{aligned} \tag{A.39}$$

with

$$B = \sqrt{-\gamma_y}\ x + K\left(\frac{\gamma_x}{\gamma_y}\right). \tag{A.40}$$

Note that V is periodic with period $L = \frac{4}{\sqrt{-\gamma_y}} K\left(\frac{\gamma_x}{\gamma_y}\right)$.

The mapping onto a one-dimensional potential and the celebrated node oscillation theorem allows one to sort the eigenstates of increasing energy according to their number of nodes. Clearly, a $\phi(x)$ node leads to a $\Psi(\alpha)$ node for the corresponding LMG eigenstate. The first $(2s+1)$ eigenstates of this Hamiltonian $\tilde{H}$ correspond to the eigenstates of the LMG Hamiltonian with the same energy. Note that, since we focus in this paper onto the $(s+1)$-dimensional "even m" sector, this leads eventually to a node number inceasing by steps of 2 for each new eigenstate.

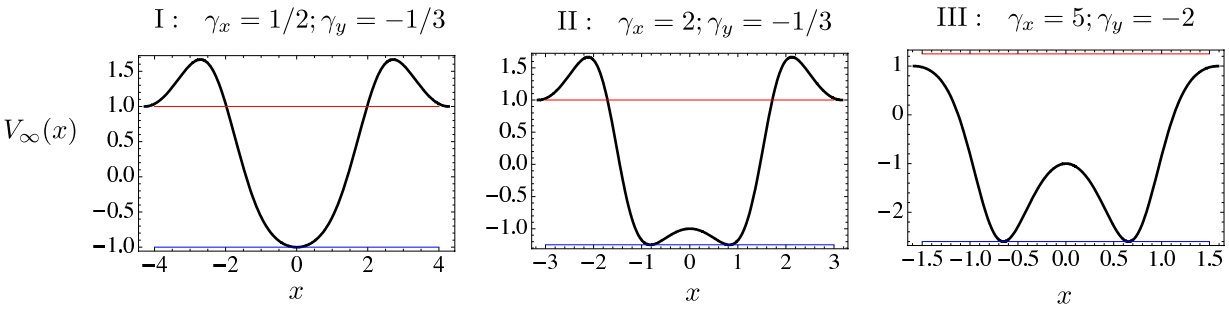

Figure A.1: Effective one-dimensional potential in the thermodynamic limit $V_\infty(x) = \lim_{s\to\infty} \frac{V(x)}{s}$ for $\gamma_y < 0$ and $h = 1$. Blue and red lines are respectively the lower and upper bounds of the spin system spectrum $\varepsilon_0 = \frac{E}{s}$.

Typical potentials are shown in Fig. A.1, with parameters associated to regions I, II and III of the LMG phase diagram. The LMG spectrum corresponds to the energies lying between the lower (blue) and the upper (red) lines. The qualitative differences between the three regions appears clearly here. Indeed, in region I the particle moves in a single-well potential whereas it is in a double-well potential in region II. In region III, a higher "allowed" energy region appears, with the extended (unbounded) states above the potential barrier. Crossing the latter corresponds to the upper density of states singularity discussed in the text. Note however that the extended or bounded nature of the eigenstates for this equivalent one-dimensional system does not have a direct translation into the nature of the corresponding eigenstates in the LMG problem.

Similar transformations can be achieved for positive γ_y but, in this case, one must consider $\tilde{H} = -\mathrm{e}^{\mathrm{i}\frac{\pi}{2}S_y} H \mathrm{e}^{-\mathrm{i}\frac{\pi}{2}S_y}$. Note the occurence of the minus sign which maps the high-energy states of the LMG model onto the low-energy states of the particle-problem (and reciprocally). Following steps (2) and (3), one obtains the potential:

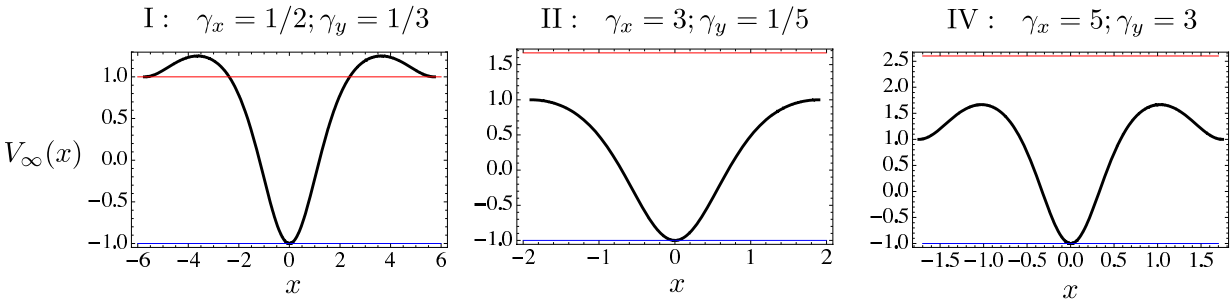

Figure A.2: Effective one-dimensional potential in the thermodynamic limit $V_\infty(x) = \lim_{s\to\infty} \frac{V(x)}{s}$ for $\gamma_y > 0$ and $h = 1$. Blue and red lines correspond respectively to the upper and lower bounds of the energy $\varepsilon_0 = \frac{E}{s}$ in the LMG problem.

$$V(x) = \frac{1}{2\gamma_y \mathrm{cn}[C\ |\gamma_y/(\gamma_y-\gamma_x)]^2 - 2\gamma_x}\Big\{h(2s+1)\,(\gamma_x-\gamma_y)\,\mathrm{cn}[C\ |\gamma_y/(\gamma_y-\gamma_x)] - \left(h^2 s + (s+1)\gamma_x\gamma_y\right)\mathrm{sn}[C\ |\gamma_y/(\gamma_y-\gamma_x)]^2\Big\},$$

with

$$C = \sqrt{\gamma_x - \gamma_y}\ x. \tag{A.41}$$

Here, V is periodic with period $L = \frac{4}{\sqrt{\gamma_x-\gamma_y}} K\left(\frac{\gamma_y}{\gamma_y-\gamma_x}\right)$. The effective potentials are displayed on Fig. A.2 for zones I, II and IV, where some care must now be taken for the correspondence with the LMG model. The upper levels (close to the upper red line) correspond to the lower levels in the LMG case.

Appendix B

Central spin model with homogeneous couplings

B.1 Introduction

The spin-boson and central-spin models are universal models describing a two-level system interacting weakly with an environmental bath composed respectively of bosonic or spin-1/2 degrees of freedom. These models are therefore of prime interest in the context of decoherence processes.

Recent developments, for instance in solid state physics, permit to manipulate and control individual two-level systems; however, the correlations of the spin with many degrees of freedom of the surrounding environment lead to finite lifetime of quantum superpositions, bringing pure states into mixed ones. The central-spin model has been used to describe noise sources in this solid state spin nanodevices arising from the hyperfine interaction with nuclear spins; a lot of efforts has been devoted to model spin bath systems (see for example [115])..

In 1991 Mermin proposed a simplified version of the central-spin model where all the spins of the bath interact symmetrically with the central one and have the same frequency [116], the so called monochromatic bath. In the literature some variations of this model were also studied under the denomination of finite Jaynes-Cummings [117] or spin-star model [118]. Moreover this model can be also viewed as a special case of the Gaudin model, which describes 1/2-spins interacting via isotropic Heisenberg couplings, in the case where coupling constants are taken to be homogeneous [119]. Although both monochromatic and polychromatic baths bring about a localization transition, in the two-level system, there nevertheless present some fundamental differences [120].

Even if it was originally introduced in order to study the ground state properties of a localization due to environment coupling [116, 120], most works on Mermin-like models consider dynamical properties of the system. The interaction of a central spin with a bath of environmental spins presents often a strong non-Markovian behavior, leading the usual derivations of Markovian quantum master equations known, e.g., from atomic physics and quantum optics, to fail. These simplified models allow sometimes formal or exact analytical solution permitting to explore non-Markovian environments [121, 118]. Variations of this

model also comprise two or more central spins in a bath of interacting spins [122], where the entanglement between central spins can also be studied.

In this section we present a method, very similar to the one used for the spin collective models in part 1 one this manuscript, to study eigenstates of a big spin S coupled to a few-level system. We apply the method to the Mermin model. The results obtained in this section are still preliminary, and we hope in the future to be able to study the dynamics of such systems.

B.2 Collective spin interacting with a few-level system

Consider a system where a spin S is coupled to a finite dimensional system taken to be a spin s. We are interested in the limit were s is small (typically $s = 1/2, 1, ...$) and $S \to \infty$. The system's Hamiltonian takes the form

$$H = H_s + H_S + H_{s+S} \tag{B.1}$$

where H_s and H_S are Hamiltonians of the s and S spin respectively and H_{s+S} is the coupling Hamiltonian. The Hilbert space of such system is spanned by the basis $\{|S, M\rangle \otimes |s, m\rangle = |M, m\rangle\}$ with $-S < M < S$ and $-s < m < s$. Therefore, a general state $|\mathbf{\Psi}\rangle = \sum_{M,m} c_{M,m}|S, M\rangle \otimes |s, m\rangle$ of the joint s-S system in the coherent S-states is given by

$$\langle\alpha|\mathbf{\Psi}\rangle = \sum_m \Psi_m(\bar{\alpha})|s, m\rangle \tag{B.2}$$

where

$$\Psi_m(\bar{\alpha}) = \sum_M c_{M,m}\langle\alpha|S, M\rangle = C\prod_{k=1}^{d}\left(\bar{\alpha} - \bar{\alpha}_k^{(m)}\right) \tag{B.3}$$

is a polynomial of maximal order $n = 2S$. In this basis, the time independent Schrödinger equation writes

$$\mathbb{H}\left(\bar{\alpha}, n^{-1}\partial_{\bar{\alpha}}\right)\mathbf{\Psi}(\bar{\alpha}) = \varepsilon\mathbf{\Psi}(\bar{\alpha}) \tag{B.4}$$

where $\mathbf{\Psi}(\bar{\alpha})$ is a column vector with entries $\Psi_m(\bar{\alpha})$ for $-s < m < s$, and $\mathbb{H}$ is a matricial differential operator.

The order of the linear differential equation for $\mathbf{\Psi}$ (B.4) is given by the powers of the S operators appearing in the Hamiltonian. Particularizing a $\Psi_m(\bar{\alpha})$, and eliminating the other components, this equation can be transformed into a higher order linear differential

equation for $\Psi_m(\bar{\alpha})$. However, in general, the resulting equation cannot be written in a Schrodinger-like form, and this procedure generates a generalized eigenvalue problem

$$\mathcal{L}\left(\varepsilon, \bar{\alpha}, n^{-1}\partial_{\bar{\alpha}}\right)\Psi_m(\bar{\alpha}) = 0 \tag{B.5}$$

where $\mathcal{L}$ is a differential operator depending, in general, non-linearly on the energy. In the following we shall indeed follow this procedure of specifying one of the m values, and we will drop the m label of Ψ.

Written in the form (B.5), the system can be considered as a generalized one dimensional problem and thus is completely integrable. However in the limit $S, s \to \infty$ the system has two classical degrees of freedom, presenting in general a chaotic behavior [123].

Focusing on the pairs $\{\varepsilon,\ \Psi_\varepsilon(\bar{\alpha})\}$, with s finite, solutions can nevertheless be given explicitly in the form of closed algebraic relations as in the LMG model. But for practical purposes the best way of studying this problem for large but finite values of n is to diagonalize numerically the Hamiltonian in its matricial form. One way of obtaining explicit solutions is, as in the LGM case, to consider the logarithmic derivative of Ψ_ε

$$G_\varepsilon(\bar{\alpha}) = n^{-1}\partial_{\bar{\alpha}}\Psi_\varepsilon(\bar{\alpha}) = n^{-1}\sum_{k=1}^{n}\frac{1}{\bar{\alpha}-\bar{\alpha}_k}, \tag{B.6}$$

that satisfies a Riccati-like equation corresponding to the operator $\mathcal{L}$. Considering the equation near the pole $\bar{\alpha}_k$ of G and setting the residue to zero, we obtain a set of n coupled equations determining all the $\bar{\alpha}_k$'s. This coupled set of non-linear equations admits $(2S+1)(2s+1)$ solutions given by sets of $\{\bar{\alpha}_k\}_{k=1}^n$. The energy ε of each solution can be obtained by considering the next to leading order term in the expansion around $\bar{\alpha}_k$.

The mean field approximation is obtained upon considering a separable state ansatz $\boldsymbol{\Psi}(\bar{\alpha}) = \boldsymbol{\eta}\,(1+\bar{\alpha}\alpha)^{2S}$ where $\boldsymbol{\eta}$ is an array of $2s+1$ complex numbers. Inserting this ansatz state in Eq.(B.4) results in a matricial equation for the $\boldsymbol{\eta}$ vector. The mean field energies $\varepsilon_m(\bar{\alpha}, \alpha)$ are the eigenvalues of the matrix obtained by this procedure. In the complex $\bar{\alpha}$-plane we obtain a set of $2s+1$ sheets. Each sheet correspond to a energy band in the $n \to \infty$ limit. Equivalently we could obtain the same result by inserting the ansatz $\Psi(\bar{\alpha}) = (1+\bar{\alpha}\alpha)^n$ in Eq.(B.5).

The large n limit is obtained by the general WKB approximation: assuming the expansions

$$G = G_0 + n^{-1}G_1 + ..., \qquad \varepsilon = \varepsilon_0 + n^{-1}\varepsilon_1 + ... \tag{B.7}$$

the Riccati-like equation decouples in powers of n^{-1} and the standard WKB procedure can be applied to obtain the spectrum and the associated eigenfunctions.

B.3 Application to the Mermin Model

B.3.1 The Mermin Model

In order to illustrate the general procedure described in the previous section, we study now the Mermin Model [116, 117, 120] with ($s = 1/2$), given by the Hamiltonian

$$H = \frac{\omega_z}{2}\sigma_z + \Omega\frac{S_z}{n} + \gamma_x\sigma_x\frac{S_x}{n} \tag{B.8}$$

where $\sigma_i = 2\hat{s}_i$, $i = x, y, z$ are the Pauli matrices. The coefficients of the S-spin operators are rescaled by $1/n$, the so-called weak-coupling regime. With this definitions, this model presents a non-trivial phase diagram as $S \to \infty$ for finite values of the coupling constants.

In the S-spin coherent states with $s = 1/2$, the state is given by a "vector" of two polynomials of degree n

$$\mathbf{\Psi}(\bar{\alpha}) = \begin{pmatrix} \Psi_+(\bar{\alpha}) \\ \Psi_-(\bar{\alpha}) \end{pmatrix} \tag{B.9}$$

and the Hamiltonian is given by the matrix differential operator Eq.(B.4)

$$\mathbb{H} = \begin{pmatrix} \frac{\omega-\Omega}{2} + \Omega\bar{\alpha}\frac{\partial_{\bar{\alpha}}}{n} & \frac{\gamma\bar{\alpha}}{2} - \frac{\gamma\left(\bar{\alpha}^2-1\right)}{2}\frac{\partial_{\bar{\alpha}}}{n} \\ \frac{\gamma\bar{\alpha}}{2} - \frac{\gamma\left(\bar{\alpha}^2-1\right)}{2}\frac{\partial_{\bar{\alpha}}}{n} & -\frac{\omega}{2} - \frac{\Omega}{2} + \Omega\bar{\alpha}\frac{\partial_{\bar{\alpha}}}{n} \end{pmatrix}. \tag{B.10}$$

B.3.2 Generalized eigenvalue equation - Equations for the zeros

Eliminating Ψ_- we obtain a closed generalized eigenvalue equation for Ψ_+

$$\left[\frac{p_2(\bar{\alpha})}{n^2}\partial_{\bar{\alpha}}^2 + \frac{p_1(\bar{\alpha})}{n}\partial_{\bar{\alpha}} + p_0(\bar{\alpha})\right]\Psi_+(\bar{\alpha}) = 0 \tag{B.11}$$

where the p_i's are polynomials of $\bar{\alpha}$ that depend on ε; explicit expressions are rather lengthy and will not be given explicitly. The corresponding Riccati equation for G (Eq. (B.6)) is given by

$$p_2(\bar{\alpha})\left[G(\bar{\alpha})^2 + \frac{1}{n}\partial_{\bar{\alpha}}G(\bar{\alpha})\right] + p_1(\bar{\alpha})G(\bar{\alpha}) + p_0(\bar{\alpha}) = 0. \tag{B.12}$$

Writing $G(\bar{\alpha})$ as a sum over simple poles (last equality of Eq. (B.6)), expanding around the pole $\bar{\alpha}_k$ and equating the residue to zero, we get a set of n coupled equations

$$\frac{n}{2}p_1(\bar{\alpha}_k) + p_2(\bar{\alpha}_k)\sum_{i\neq k}(\bar{\alpha}_k - \bar{\alpha}_i)^{-1} = 0 \tag{B.13}$$

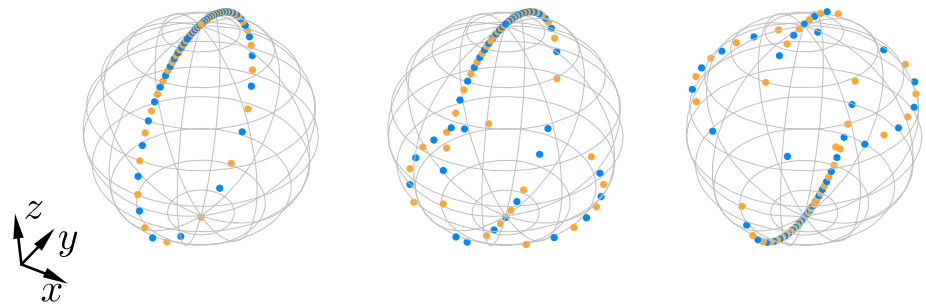

Figure B.1: Inverse stereographic projection of a set $\{\bar{\alpha}_k\}_{k=1}^{n}$ for Ψ_+ (orange) and Ψ_- (blue) for the k-th excited state of the Mermin Hamiltonian. ($n = 40$, $\Omega = 2, \omega = 0.1, \gamma = 1$, from left to right: $k = 1, 20, 60$.)

The missing equation relating the $\bar{\alpha}_k$'s and the energy ε can be obtained by evaluating Eq.(B.12) away from a pole (for example at $\bar{\alpha} = 0$ assuming $\bar{\alpha}_k \neq 0$ for all k). Figure (B.1) represents an example of such set of $\bar{\alpha}_k$'s. We have assumed here that the $\bar{\alpha}_k$'s are all different, which is true in general. Note however that, for some specific values of the coupling constants, G can have poles with residues bigger than 1, a case that we do not consider here.

B.3.3 Mean Field Energy and the Large S Limit

Applying the above described method to the mean field energy $\varepsilon(\bar{\alpha}, \alpha)$, with $s = 1/2$, two energy sheets are obtained

$$\varepsilon_{\pm} = -\frac{\Omega(1 - \alpha\bar{\alpha}) \pm \sqrt{\gamma^2 (\alpha + \bar{\alpha})^2 + \omega^2 (\alpha\bar{\alpha} + 1)^2}}{2\alpha\bar{\alpha} + 2} \tag{B.14}$$

To each such sheet, it corresponds an energy band in the spectrum. The extremal energies of each band can be obtained by analyzing these surfaces (see Fig. B.3). It is also possible to identify hyperbolic points, which lead to singular behavior in the density of states. In addition, and in constrast to the LMG case, we now face cases where energy bands intersect (for example in Fig. B.3-(3), around $\varepsilon = 0$). The mean field results are summarized in the phase diagram of the model, Fig. B.2, presenting four regions with qualitatively different spectra.

Observable expectation values, for eigenstates, are presented in Fig. B.4. Due to the symmetry of the model the mean values of σ_x and σ_y are both zero for all eigenstates. For a single spin 1/2, the radius of the Bloch sphere for a pure state is $r^2 =< \boldsymbol{\sigma} >^2 = 1$ and $r = 0$ for maximal entangled states. The entanglement between the small s and the big S spin can thus be simply read in the value of σ_z: un-entangled states have $< \sigma_z >= \pm 1$. Note also that, in this simplified model, the two energy bands are symmetrical with respect the

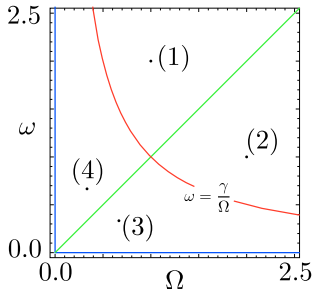

Figure B.2: Phase Diagram for the Mermin Hamiltonian model (for $\gamma = 1$). Due to symmetry, only the first quadrant needs to be analyzed. The four labels indicate the precise parameter values that are considered in the examples treated in Fig. B.3, and Fig. B.4.

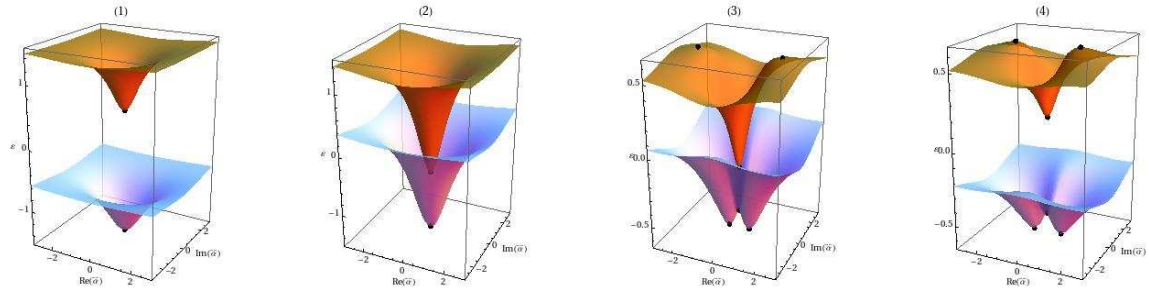

Figure B.3: Mean field energy sheets in the complex $\bar{\alpha}$ for the representative cases of Fig. B.2.

middle of the spectrum; corresponding eigenstates are the "plus" or "minus" occurrence for $e^{i\pi(S_z+S)}\sigma_z|\Psi\rangle = \pm|\Psi\rangle$; for a general $s-S$ system, this symmetry will be absent. Using a method similar to the one used for the LMG model, it is possible to compute analytically all the quantities presented in Fig. B.4; this analysis will be done in the future. We just briefly describe the different zones:
Zone (1) - The spectrum extrema for the two energy bands correspond to separable states at the thermodynamic limit. No singularities arise within the spectrum.
Zone (2) - Similar to zone (1), but with energy band interpenetration.
Zone (3) - There are critical energies within the spectrum corresponding to hyperbolic points showed in Fig. B.3; moreover this region presents a energy band interpenetration. The ground and the most excited states correspond to entangled states of the $s-S$ system.
Zone (4) -Similar to zone (3) but without energy band interpenetration.

The model presents a QPT line given by $\omega = \frac{\gamma^2}{\Omega}$, where the ground state mean value of σ_z presents a singular behaviour (Fig. B.5), passing from a region where the $s-S$ system is not entangled at the thermodynamic limit to a region where the ground state is

non-separable.

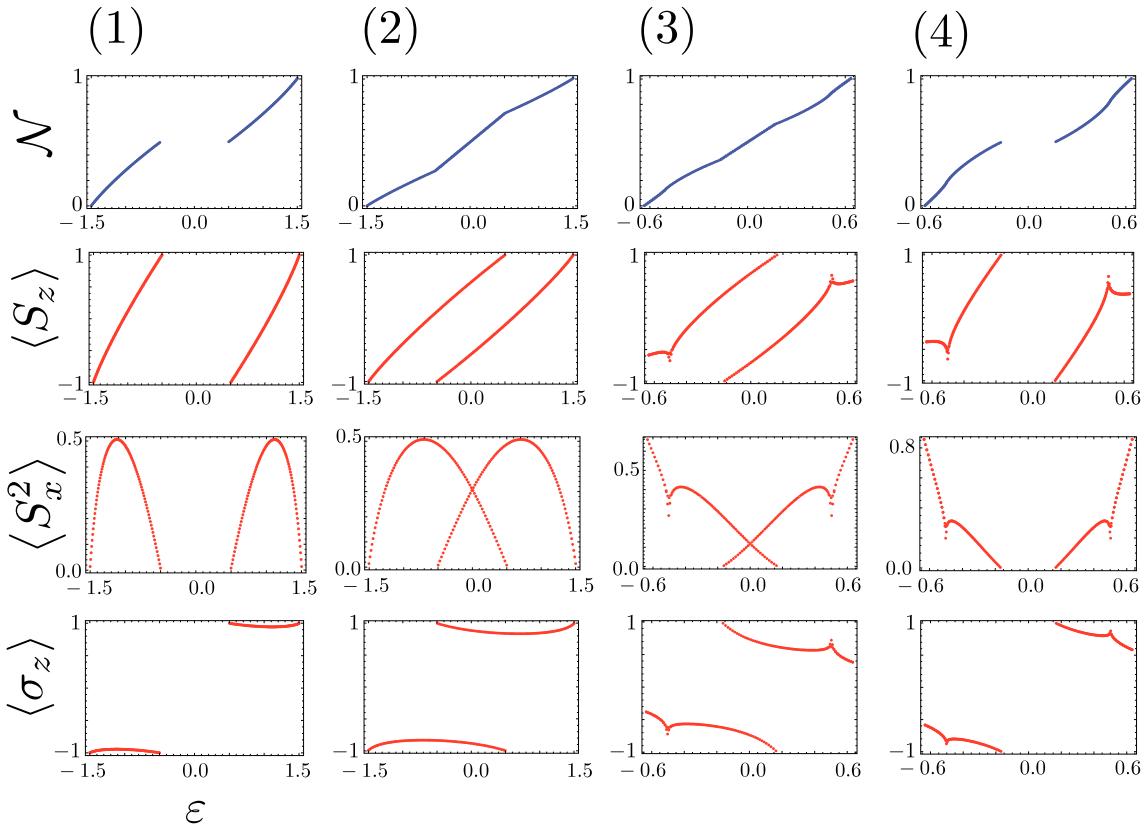

Figure B.4: Integrated density of states $\mathcal{N}$ and mean values of the observables (S_z, S_x and σ_z), computed numerically for the eigenstates of the Mermin model as a function of the energy, for the representative cases of Fig. B.2 ($n = 50$).

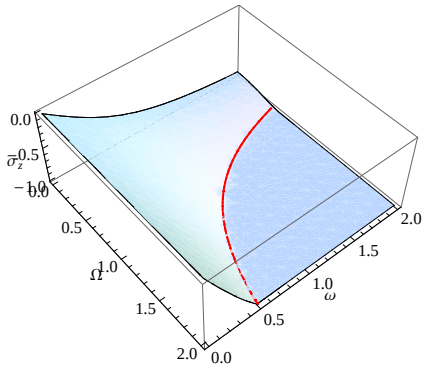

Figure B.5: Ground State expectation value of σ_z.

B.3.4 Conclusion

We present a method which allows us to treat a few-level system coupled to a spin S in the limit $S \to \infty$. It is an extension of the spin coherent states, and the WKB approximation, developed for collective spins in the first part of this manuscript, and gives the spectrum and the eigenvectors of the model. We study the Mermin Hamiltonian and derive the phase diagram of the model. We also present some numerical computations of observables expectation values for eigenstates, and point-out the existence of "exceptional" points within the spectrum for phases (3) and (4). At the border between these regions, there is a QPT line corresponding to a second order phase transition, where the $s - S$ system also displays an entangled to non-entangled behaviour. We expect this preliminary work to help us studying the dynamical properties of the model. It could also be interesting, but maybe difficult in practice, to study big, but nevertheless finite s values; such a system would interpolate between an integrable system, with one (collective) degree of freedom and an effective two dimensional system (where chaotic behaviour would be expected).

Appendix C

Entanglement and Hilbert space geometry for few qubits systems

C.1 Introduction

The rapidly growing field of quantum information is based on the subtle and often counter-intuitive properties of quantum states entanglement[124][84]. It is therefore of high interest to have a geometrical picture of this latter property, directly written in the Hilbert space where the quantum evolution takes place. However, even for few qubits, this space is of high dimension, which makes it difficult to visualize, and entanglement turns out to be a complicate concept (see for example [125, 126]).

In this appendix, we present some optimal discretized Hilbert space (similar to what polytopes are to continuous hyperspheres), and their interesting relation to dense sphere packings in high-dimensional real space. To do so, we briefly recall some known facts on Hilbert space geometry for few (two and three) qubits, in relation with the so-called (high dimensional) sphere Hopf fibrations. For one qubit (a single two-level system), a well known tool in quantum optics is the Bloch sphere (S^2) representation, which is related to Hopf fibration of the S^3 hypersphere. A generalization for a two-qubit system was proposed [127], in the framework of the S^7 sphere Hopf fibration. An interesting result is that the S^7 Hopf fibration is entanglement sensitive and therefore provides a kind of foliation for the 2 qubits (projective) Hilbert space with respect to their entanglement content. An extension of this description to a three qubits system, using the S^{15} Hopf fibration, will also be presented here.

Interesting sets of discrete two and three-qubits states are then obtained by intersecting the S^7 and S^15 spheres with high dimensional dense lattices in 8 and 16 dimensions. The same discrete qubits sets can also be defined algebraically based on stabilizer theory.

C.2 Entanglement and Hopf fibrations

A n-qubit state can be written as

$$|\Psi\rangle = \sum_{l=0}^{2^n-1} t_l \, |l\rangle \quad \text{with} \;\; t_l \in \mathbb{C}, \text{ and the normalization } \sum \;\; |t_l|^2 = 1$$

Here $|l\rangle$ stands for the n-qubit base 2 decomposition of the integer l, with each qubit being associated with one basis factor of the n-qubit tensor product

$$|l\rangle = |\alpha_1\rangle_1 \otimes |\alpha_2\rangle_2 \otimes \cdots |\alpha_n\rangle_n$$

where $\alpha_j = 0$ or 1 according to the decomposition of l. In principle, the n-qubit Hilbert space is $\mathbb{C}^{2^n}$, or $\mathbb{C}P^{2^n-1}$ for the projective version where the global phase freedom is taken into account. But the normalization condition makes it more natural to consider $S^{2^{n+1}-1}$ spheres embedded in $\mathbb{R}^{2^{n+1}}$

C.2.1 Two qubits entanglement and the S^7 Hopf fibration

A generic two-qubit state reads

$$|\Psi\rangle = t_0 \, |00\rangle + t_1 \, |01\rangle + t_2 \, |10\rangle + t_3 \, |11\rangle$$

where we have explicitely used the base 2 decomposition to highlight the underlying tensor product. A state $|\Psi\rangle$ is said "separable" if, thank to individual qubits basis rotations, it can be written as a simple product

$$|\Psi\rangle = |\varphi\rangle_1 \otimes |\theta\rangle_2 \, .$$

It is easy to show that this is only possible if

$$t_0 t_3 - t_1 t_2 = 0$$

The deviation of the LHS from zero leads to a measure of state entanglement, which is known as the "concurrence" c [103], in the form

$$c = 2 \, |t_0 t_3 - t_1 t_2|$$

a quantity which will play an important role below. Indeed, we aim to foliate the two qubit projective Hilbert space $\mathbb{C}P^3$, in terms of equi-concurrence manifolds. As will become soon clear, the S^7 Hopf fibration will prove to be of great help to fulfill this task [127].

The S^7 Hopf fibration is defined using quaternions (with the quaternion algebra denoted $\mathbb{Q}$), instead of complex numbers. We combine two complex components into a quaternion (using the quaternionic $\mathbf{j}$ unit) in the form

$$q_1 = t_0 + t_1\mathbf{j},\ q_2 = t_2 + t_3\mathbf{j}, \qquad q_{1,}q_2 \in \mathbb{Q}, \tag{C.1}$$

A point (representing the state $|\Psi\rangle$) on the unit radius S^7, is represented as a pair of quaternions $(q_{1,}q_2)$ satisfying $|q_1|^2 + |q_2|^2 = 1$. The Hopf map from S^7 to the base S^4 is the composition of a map h_1 from S^7 to R^4 $(+\infty)$, followed by an inverse stereographic map h_2 from R^4 to S^4.

$$\begin{array}{rccc} h_1: & S^7 & \longrightarrow & R^4 + \{\infty\} \\ & (q_1, q_2) & \longrightarrow & Q = \overline{q_1 q_2^{-1}} \end{array} \qquad q_{1,}q_2 \in \mathbb{Q}$$

$$\begin{array}{rccc} h_2: & R^4 + \{\infty\} & \longrightarrow & S^4 \\ & Q & \longrightarrow & M(x_l) \end{array} \qquad \sum_{l=0}^{l=4} x_l^2 = 1 \tag{C.2}$$

The base space S^4 is not embedded in S^7 : the fibration is not trivial. The fibre is a unit S^3 sphere : the S^7 points $(q_{1,}q_2)$ and $(q_1 q,\ q_2 q)$, with q a unit quaternion (geometrically a S^3sphere) are mapped onto the same Q value.

Let us write Q in terms of the original components t_l

$$Q = \overline{q_1 q_2^{-1}} = \frac{1}{\sin^2(\theta/2)}\,(C_1 + C_2\mathbf{j}) \tag{C.3}$$

$$\text{with } \sin(\theta/2) = |q_2|\,,\ C_1 = \left(\overline{t_0}t_2 + \overline{t_1}t_3\right),\ C_2 = (t_0 t_3 - t_1 t_2) \text{ and } C_1, C_2 \in \mathbb{C}$$

The simple relation between the concurrence entanglement measure c and the C_2 term is striking : $c = 2\,|C_2|$. This shows that, if correctly oriented, **the Hopf map is entanglement sensitive**! Indeed, states that are mapped onto pure complex values for Q are separable states. In addition, the fibre structure implies that a whole S^3 manifold is singled out with the same entanglement content.

C.2.2 Three qubits, and the S^{15} Hopf fibration

A generic three-qubit state reads

$$|\Psi\rangle = \sum_{l=0}^{7} t_l\,|l\rangle \quad \text{with } t_l \in \mathbb{C}, \text{ and } \sum |t_l|^2 = 1$$

The $|\Psi\rangle$ normalization condition leads to considering the 15-dimensional sphere S^{15}, embedded in R^{16}. This has suggested to look whether the third Hopf fibration (that of

S^{15}, with base S^8 and fibres S^7) could be helpful for describing the 3 qubits Hilbert space geometry[128][129]. One should first recognize that the concept of entanglement turns complicate when more qubits are added. Do we speek of the entanglement of one qubit with respect to the other two qubits (irrespective of the dedree of entanglement between these latter two), or of some "true" three qubit entanglement, as measured for instance by the 3-tangle [130]?

It is interesting here to recall about entanglement invariants, which are functions of the state component t_l, invariant under the action of local unitary operations (the latter leaving entanglement unchanged). For two qubits, there are 2 such invariants, the (trivial) norm of the state, and the concurrence. Therefore, as shown above, the S^7 Hopf map displays the two-qubit invariant. For three qubits, there are 6 invariants, which can be expressed in different ways. A possible choice is the norm of the state, the three radii r_j, $j = 1 \cdots 3$ of the partial Bloch spheres, the 3-tangle τ_3 and a last one, introduced by J. Kempe [131]

Omitting the trivial norm invariant, we would like to foliate the (14-dimensional) three qubits projective Hilbert space $\mathbb{C}P^7$ with respect to the different values of the invariant 5-uplets. This task is rather complicate, and has not been fulfilled up to now; however, we shall see now that the S^{15} Hopf fibrations can tell something about this manifold.

To define the fibration, one proceeds along the same line as for the S^7 case, but using now octonions (with the octonion algebra denoted $\mathbb{O}$). The interested reader should refer to the appendix of ref. [129] for information about the octonion multiplication that is used here. We write

$$a = a' + a''\mathbf{e},\ b = b' + b''\mathbf{e}, \qquad a, b \in \mathbb{O}, \text{ and } a', a'', b', b'' \in \mathbb{Q}, \tag{C.4}$$

and a point (representing the state $|\Psi\rangle$) on the unit radius S^{15} as a pair of octonions (a, b) satisfying $|a|^2+|b|^2 = 1$. But, to get a Hopf map of physical interest, with coordinates simply related to interesting observable expectation values, one needs to define a slightly tricky relation between $|\Psi\rangle$ and the octonions pair (a, b), as follows:

$$\begin{aligned} a &= (t_0 + t_1\mathbf{j}, t_2 + \mathbf{j}t_3) = (t_0 + t_1\mathbf{j}, t_2 + \overline{t_3}\mathbf{j}) = (a', a'') \\ b &= (t_4 + t_5\mathbf{j}, t_6 + \mathbf{j}t_7) = (t_4 + t_5\mathbf{j}, t_6 + \overline{t_7}\mathbf{j}) = (b', b'') \end{aligned} \tag{C.5}$$

The Hopf map from S^{15} to the base S^8 is the composition of a map h_1 from S^{15} to R^8 $(+\infty)$, followed by an inverse stereographic map h_2 from R^8 to S^8.

$$\begin{aligned} h_1 : \quad & \begin{array}{ccc} S^{15} & \longrightarrow & R^8 + \{\infty\} \\ (a, b) & \longrightarrow & P = \overline{ab^{-1}} \end{array} \qquad a, b \in \mathbb{O} \\ h_2 : \quad & \begin{array}{ccc} R^8 + \{\infty\} & \longrightarrow & S^8 \\ P & \longrightarrow & M(x_l) \end{array} \qquad \sum_{l=0}^{l=8} x_l^2 = 1 \end{aligned} \tag{C.6}$$

The base space S^8 is not embedded in S^{15} : the fibration is again not trivial. The fibre is a unit S^7 sphere, the proof of which is more tricky (and not given here) than in the lower dimension case. The h_1 map leads to

$$P = \overline{ab^{-1}} = \frac{1}{\sin^2\theta/2}\left(Q_1 + Q_2\mathbf{e}\right) \tag{C.7}$$
$$\text{with } \sin\theta/2 = |b|\,,\ Q_1 = (b'\overline{a'} + \overline{a''}b'')\,,\ Q_2 = (-a''b' + b''a') \text{ and } Q_1, Q_2 \in \mathbb{Q}$$

Although this is not at first sight evident, the Hopf map is still entanglement sensitive in that case. To show this, it is instructive to first express Q_1 and Q_2 in term of the t_l components read out from (C.5).

$$Q_1 = \left(\overline{t_0}t_4 + \overline{t_1}t_5 + \overline{t_2}t_6 + \overline{t_3}t_7\right) + \left(t_0t_5 - t_1t_4 + \overline{t_2t_7} - \overline{t_3t_6}\right)\mathbf{j}$$
$$Q_2 = \left(t_0t_6 + t_2t_4 + \overline{t_3t_5} - \overline{t_1t_7}\right) + \left(t_1t_6 - t_2t_5 + \overline{t_0t_7} - \overline{t_3t_4}\right)\mathbf{j}$$

Introducing the generalised complex concurrence terms $T_{ij,kl} = t_it_j - t_kt_l$ allows to write in a synthetic form the coordinates on the unit radius base S^8. The second map h_2 sends states onto points on S^8, with coordinates x_l, with l running from to 0 to 8. With the inverse stereographic pole located on the S^8 "north pole " ($x_0 = +1$), and the target space R^8 cutting S^8 along the equator, we get the following coordinate expressions

$$x_0 = \cos\theta = |a|^2 - |b|^2 = \langle\sigma_z \otimes Id \otimes Id\rangle_\Psi \tag{C.8}$$
$$x_1 + \mathbf{i}\,x_2 = 2\left(\overline{t_0}t_4 + \overline{t_1}t_5 + \overline{t_2}t_6 + \overline{t_3}t_7\right) = \left\langle\left(\sigma_x + \mathbf{i}\,\sigma_y\right)_1 \otimes Id \otimes Id\right\rangle_\Psi$$
$$x_3 + \mathbf{i}\,x_4 = 2\left(T_{05,14} + \overline{T_{27,36}}\right)$$
$$x_5 + \mathbf{i}\,x_6 = 2\left(T_{06,24} + \overline{T_{35,17}}\right)$$
$$x_7 + \mathbf{i}\,x_8 = 2\left(T_{16,25} + \overline{T_{07,34}}\right)$$

Three-qubits states such that the first qubit is separated from the two others map onto a point such that $x_j = 0$, for $j = 3\cdots8$. Indeed, in a multi-qubit state, a given qubit is separated from the others when its partial Bloch sphere has a radius $r_1 = 1$. The first qubit partial Bloch sphere is spanned here by the triplet (x_0, x_1, x_2). Going back to the above definition of the h_1 map, this means that in that case, the Hopf map carries an octonion couple onto a pure complex number P. Therefore, as for two-qubits case, the S^{15} Hopf fibration is also entanglement sensitive for three qubits!

C.3 Hilbertian polytopes

In this section, we derive discretized versions of the n-qubit projective Hilbert space $\mathbb{C}P^{2^n-1}$, which are analogous to standard polytopes with respect to spherical spaces. These

"Hilbertian polytopes" have been described along two a priori different (algebraic and geometric) approaches, which eventually leads to the same structures. These structures have been defined from a generic point of view, and detailed for one and two qubits [132]. This construction will be briefly recalled here; in addition, we further describe the three-qubit case, with its 1080 states in $\mathbb{C}P^7$.

C.3.1 Discretization based on stabilizer theory

Let us first define the n-qubit Pauli group $\mathcal{G}_n$, as the set of all n-fold tensor products of 2×2 Pauli matrices, with four possible overall phases to satisfy the closure requirement:

$$\mathcal{G}_n = \{\sigma_w, \sigma_x, \sigma_y, \sigma_z\}^{\otimes n} \otimes \{\pm 1, \pm i\}\,,$$

We denote by $\Sigma_{\alpha\beta\ldots\zeta} = \sigma_\alpha \otimes \sigma_\beta \otimes \cdots \otimes \sigma_\zeta$ the generalized Pauli matrices .

Here we disregard the phases $\{\pm 1, \pm i\}$ required for closure of $\mathcal{G}_n$ under multiplication and deal with the *set* $\mathcal{S}_n$ of 4^n generalized Pauli matrices rather than the group $\mathcal{G}_n$. Doing this, the stabilizer of $\mathcal{G}_n$ transfer to Abelian subsets of $\mathcal{S}_n$, called *pseudo*stabilizers. The largest possible subsets of $\mathcal{S}_n$ whose elements all mutually commute have 2^n elements, and are denoted s_n^a, where a labels the different subsets . These *maximal* pseudostabilizers form the foundation of this discretization procedure.

Finally, the Hilbertian polytope $\mathfrak{H}_n$ is defined as the set of n-qubit state vectors which are the common eigenvectors of the elements of s_n^a, for all subsets a.

The uniform Hilbertian polytope on n qubits $\mathfrak{H}_n$ contains

$$V_n = 2^n \prod_{k=0}^{n-1} (2^{n-k} + 1)$$

vertices, or states. The following table gives the first values of V_n, along with C_n, the number of classical bit configurations for comparison.

n	1	2	3	4	5	6	7
V_n	6	60	1080	36720	2423520	315057600	81284860800
C_n	2	4	8	16	32	64	128

V_n grows as $2^{(n^2+3n)/2}$, so the information content is super-extensive in n.

We shall not give here an explicit construction of the uniform Hilbertian polytope for the one- and two-qubit cases based on this algebraic approach. We shall focus on an alternative geometrical approach.

C.3.2 Alternate approach: shelling the high-dimensional dense lattices

We now present another, more geometrical, approach to Hilbert space discretization, which uses the successive shells of dense lattices in $\mathbb{R}^{2^{n+1}}$ to discretize the high dimensional hyperspheres. At the same time, we must take into account the global phase freedom, and show how a discretization of the projective Hilbert space is induced (this means that several points on S^{2^n-1} will represent the same physical state). In light of this, it is important to distinguish between "qubit states"—the quantum states associated to the points on S^{2^n-1}—and "physical states"—the states in the projective Hilbert space, which has the geometry of a complex projective space CP^{2^n-1}.

We consider the family of laminated lattices Λ_i. These laminated lattices form a series which starts with the triangular lattice in $2d$ (the densest lattice in $2d$). Λ_3 is obtained as a particular sequence of Λ_2 lattices packed in a third dimension, which gives the face centered cubic lattice, one of the two densest lattices in $3d$. Appropriately packing Λ_3 lattices along a fourth dimension leads to Λ_4, whose first shell is precisely the $\{3, 4, 3\}$ polytope [133] we will use here for the one-qubit case. Upon iteration, this construction eventually leads to the $\Lambda_8 = E_8$ lattice suitable for the two-qubit case. We shall focus here on the set of 240 sites belonging to the E_8 first shell that forms the, so-called, *Gosset polytope* and, as for the one-qubit case, enumerate the physical states they represent. Finally we present new results with a set of 1080 discrete 3-qubits states which originate from the 16-dimensional dense lattice Λ_{16}

C.3.3 The one-qubit case and the Λ_4 lattice

We give two possible (dual) coordinates for the $\{3, 4, 3\}$ vertices, in each case as a real quadruplet and a complex pair. The correspondence between real quadruplets and complex pairs amounts simply to taking the first two (last two) real numbers as the real and imaginary part of the first (second) complex number. The first (second) complex number in the pair corresponds to t_0 (t_1).

A first set, denoted T_1, is the union of the eight permutations of type $(\pm 1, 0, 0, 0)$ and the sixteen permutations of type $\frac{1}{2}(\pm 1, \pm 1, \pm 1, \pm 1)$. Note that, modulo a global phase factor, these twenty-four points really represent six different physical states, which appear on the Bloch sphere as opposite points on the three orthogonal axes x, y, z. Indeed, the four points,

Real quadruplets	Complex pairs
$(1,0,0,0)$	$(1,0)$
$(-1,0,0,0)$	$(-1,0)$
$(0,1,0,0)$	$(i,0)$
$(0,-1,0,0)$	$(-i,0)$

represent the states $|\Psi_1,\omega\rangle = e^{i\omega}|0\rangle$, with $\omega = 0,\pi/2,\pi,3\pi/2$,which map to the same point on the Bloch sphere (the north pole), and they are therefore associated to the physical state $|\Psi_1\rangle$. Equivalently, the four points

Real quadruplets	Complex pairs
$(0,0,1,0)$	$(0,1)$
$(0,0,-1,0)$	$(0,-1)$
$(0,0,0,1)$	$(0,i)$
$(0,0,0,-1)$	$(0,-i)$

represent the four states $|\Psi_2,\omega\rangle = e^{i\omega}|1\rangle$ with $\omega = 0,\pi/2,\pi,3\pi/2$. The other sixteen vertices represent four other physical states, in the following way:

$$|\Psi_3\rangle \equiv \tfrac{e^{i(\omega+\pi/4)}}{\sqrt{2}}(|0\rangle - |1\rangle), \quad |\Psi_4\rangle \equiv \tfrac{e^{i(\omega+\pi/4)}}{\sqrt{2}}(|0\rangle - |1\rangle),$$
$$|\Psi_5\rangle \equiv \tfrac{e^{i(\omega+\pi/4)}}{\sqrt{2}}(|0\rangle + i|1\rangle), \quad |\Psi_6\rangle \equiv \tfrac{e^{i(\omega+\pi/4)}}{\sqrt{2}}(|0\rangle - i|1\rangle),$$

with $\omega = 0,\pi/2,\pi,3\pi/2$.

For the later purpose of a discrete two-qubit construction, it is useful to describe a second version of the polytope $\{3,4,3\}$, for which the twenty-four vertices form a set T_2 given by twenty-four permutations of the type $\{\pm1,\pm1,0,0\}/\sqrt{2}$. This polytope is obtained from the former one through a *screw* motion on S^3 of angle $\pi/4$. This set leads to twenty-four states

$$|\Phi_l,\omega\rangle = \epsilon|\Psi_l,\omega\rangle, \quad l = 1..6, \quad \omega = 0,\pi/2,\pi,3\pi/2, \text{ and } \quad \epsilon = e^{i\pi/4}$$

and to the six one-qubit physical states $|\Phi_l\rangle$ identical to $|\Psi_l\rangle$. Indeed, the six states $|\Psi_j\rangle$ sit at the vertices of a regular octahedron. Since the states $|\Phi_l,\omega\rangle$ only differ from $|\Psi_l,\omega\rangle$ by a global phase, they map onto the same six points on the Bloch sphere.

C.3.4 The two-qubit case and the E_8 lattice

The 240 vertices of the Gosset polytope belong to a sphere S^7. These 240 vertices may be separated into ten equivalent subsets, each belonging to non-intersecting S^3 spheres. This is nothing but a discrete version of the S^7 Hopf fibration, with fibers S^3 and base S^4[134, 135, 136].

We use here quaternionic coordinates instead of complex or real ones. The above set T_1, scaled such that the corresponding points belong to a sphere S^3 of radius $\frac{1}{\sqrt{2}}$, now reads:

$$T_1 = \{\pm\frac{1}{\sqrt{2}}, \pm\frac{\mathbf{i}}{\sqrt{2}}, \pm\frac{\mathbf{j}}{\sqrt{2}}, \pm\frac{\mathbf{k}}{\sqrt{2}}, \frac{1}{2\sqrt{2}}(\pm 1 \pm \mathbf{i} \pm \mathbf{j} \pm \mathbf{k})\},$$

where $\mathbf{i}, \mathbf{j}$ and $\mathbf{k}$ are the standard unit quaternions. The set T_2 stays on a unit sphere and reads:

$$T_2 = \{\frac{1}{\sqrt{2}}(\pm 1 \pm \mathbf{i}), \frac{1}{\sqrt{2}}(\pm 1 \pm \mathbf{j}), \frac{1}{\sqrt{2}}(\pm 1 \pm \mathbf{k}), \frac{1}{\sqrt{2}}(\pm \mathbf{i} \pm \mathbf{j}), \frac{1}{\sqrt{2}}(\pm \mathbf{i} \pm \mathbf{k}), \frac{1}{\sqrt{2}}(\pm \mathbf{j} \pm \mathbf{k})\}.$$

The 240 vertices of the Gosset polytope belong to the ten sets:

$$S_1 = (T_2, 0), \quad S_2 = (0, T_2), \quad S_3 = (T_1, T_1), \quad S_4 = (T_1, -T_1), \quad S_5 = (T_1, \mathbf{i}T_1),$$
$$S_6 = (T_1, -\mathbf{i}T_1), \quad S_7 = (T_1, \mathbf{j}T_1), \quad S_8 = (T_1, -\mathbf{j}T_1), \quad S_9 = (T_1, \mathbf{k}T_1), \quad S_{10} = (T_1, -\mathbf{k}T_1).$$

Each of the ten sets gives a copy of a $\{3, 4, 3\}$ polytope on a fiber S^3. The points can be Hopf mapped, as described above, onto the base space S^4. The location of the mapped point is intimately related to the entanglement of the corresponding two-qubit state.

It is then easy to verify that the sets S_1 to S_6 correspond to separable states, while sets S_7 to S_{10} correspond to maximally entangled states.

More precisely, the six sets $S_1 \cdots S_6$ encompass $6 \times 24 = 144$ vertices, forming altogether 36 physical states, with four values of the global phase for each qubit state. Note that the precise value of the phases are important here in order that our discretization procedure uniformly cover the full Hilbert space. Using the above defined eigenstates of the one-qubit Pauli matrices, these states read:

$\|\pm x\rangle \otimes \|\pm x\rangle\, e^{i(\pi/4+m\pi/2)}$	$\|\pm x\rangle \otimes \|\pm y\rangle\, e^{i(\pi/4+m\pi/2)}$	$\|\pm x\rangle \otimes \|\pm z\rangle\, e^{im\pi/2}$
$\|\pm y\rangle \otimes \|\pm x\rangle\, e^{i(\pi/4+m\pi/2)}$	$\|\pm y\rangle \otimes \|\pm y\rangle\, e^{i(\pi/4+m\pi/2)}$	$\|\pm y\rangle \otimes \|\pm z\rangle\, e^{im\pi/2}$
$\|\pm z\rangle \otimes \|\pm x\rangle\, e^{im\pi/2}$	$\|\pm z\rangle \otimes \|\pm y\rangle\, e^{im\pi/2}$	$\|\pm z\rangle \otimes \|\pm z\rangle\, e^{i(\pi/4+m\pi/2)}$

where $m = 0, 1, 2, 3$ triggers the global phase. Each of the nine entries stands for the four possible sign combinations, leading to the announced thirty-six physical states. A simple view of these separable states consists in relating them to the "product" of two octahedra, each one belonging to the Bloch sphere of the individual qubits.

The remaining four sets (altogether $4 \times 24 = 96$ sites) lead to a slightly more subtle structure. We find a total of twenty-four different physical MES, with four phase-distinct two-qubit states for each. But in the present case, the phase-distinct states actually belong to two different sets, either (S_7, S_8) or (S_9, S_{10}). These twenty-four physical states can be written as

$\frac{1}{\sqrt{2}}\left(\|+z,+z\rangle + e^{i\theta}\|-z,-z\rangle\right)$	$\frac{1}{\sqrt{2}}\left(\|+z,-z\rangle + e^{i\theta}\|-z,z\rangle\right)$
$\frac{1}{\sqrt{2}}\left(\|+z,+x\rangle + e^{i\theta}\|-z,-x\rangle\right)$	$\frac{1}{\sqrt{2}}\left(\|+z,-x\rangle + e^{i\theta}\|-z,+x\rangle\right)$
$\frac{1}{\sqrt{2}}\left(\|+z,+y\rangle + e^{i\theta}\|-z,-y\rangle\right)$	$\frac{1}{\sqrt{2}}\left(\|+z,-y\rangle + e^{i\theta}\|-z,+y\rangle\right)$

with $\theta = 0, \pi/2, \pi, 3\pi/2$.

Note that these twenty-four entangled states, together with the above thirty-six separable states, are in one-to-one correspondence, up to a global phase, with the sixty discrete states on $\mathfrak{H}_2$ obtained by the algebraic approach.

C.3.5 Finer discretizations of H_2: higher E_8 shells

The present lattice approach have the benefit of allowing finer discrete sets to be explored in a straightforward manner by considering the higher order shells in E_8. This construction would provide a uniform set of two-qubit states, some of which would have intermediate entanglement. A note of caution is in order here, since we are only interested in describing normalized quantum states. Lattice points which are aligned, as viewed from the origin, contribute to the same two-qubit state.

We do not give here a detailed description of these finer discretizations of H_2. However, we note that the number M_J of sites on the J^{th} shell around an E_8 vertex is simply given by[137]

$$M_J = 240 \sum_{d|J} d^3,$$

where d denotes integers which divide J. The table below displays these numbers for the first four shells. Again, the physical states are obtained from these two-qubit states by modding out a global phase.

J	1	2	3	4
M	240	2160	6720	17520

The shell by shell analysis, and its relation to the Hopf map, was done elsewhere[134, 135]. It allows us to get points on the second shell corresponding to states having concurrence $0, 1/2, 1/\sqrt{2}, 1$. The third shell contributes states of concurrence 0, 1/3, 2/3, $\sqrt{5}/3$, $\sqrt{8}/3$ and 1.

C.3.6 The three-qubit case, $\mathfrak{H}_3$ and the Λ_{16} lattice

This case should be related to the dense lattice Λ_{16} in $\mathbb{R}^{16}$ (see ref.[137]). It is interesting to note that the number of lattice sites closest to the origin—the lattice "kissing number"—for this case is 4320, which is precisely four times the expected number of vertices on the

uniform Hilbertian polytope $\mathfrak{H}_3$. We are therefore likely to face a similar situation as in the one- and two-qubit cases, where there were four phase-related qubit states associated with each physical state. And indeed, the four-to-one relation between the Λ_{16} first shell sites and the vertices of $\mathfrak{H}_3$ has been checked.

With a suitably oriented S^{15} Hopf fibration, the 4320 sites in the first shell organize as 18 sets of 240 sites belonging to a S^7 fibre; each such set is a copy of a 240-site Gosset polytope, which therefore shows a nice nested structure. The 18 sets are uniquely defined by the coordinates of the corresponding point on the base space S^8. The corresponding 18-site polytope is nothing but the "cross polytope" in $\mathbb{R}^9$, with two opposite points along 9 orthogonal directions.

Upon modding out the global phase, we find that, as for the entangled 2-qubits states, some phase-distinct states belong to different fibres. The 1080 discrete 3-qubits states belong to three different classes : fully separable, products of one-qubit times a maximally 2-qubits entangled states, or maximally entangled (as measured by the 3-tangle).

More precisely, among the 18 fibres :

- six fibres (whose octonionic coordinates on the base space reduce to a complex number) contains states that are either triple product states, or product of the first qubit with a MES in the remaining two qubits

- the remaining 12 fibres contains states that are either product of the second or third qubit with a MES in the remaining two qubits, or states with true (and maximal) 3-qubit entanglement, characterized by a 3-tangle equals to unity

As a whole, one finds :

- a set of 216 triple product states
- a set of 432 states, product of one qubit times a MES in the remainig two
- a set of 432 maximally entangled 3-qubit states (with unit 3-tangle)

Note that the first two sets could already be generated from the two and one-qubit analysis, with (suitably oriented) Λ_8 and Λ_4, while the third is really new.

Generalization to more than three qubits cannot use the Hopf fibrations, limited to S^{15}. A particularly interesting family to be checked further is the one described long ago by John Leech[138], which coincides with those studied here for $N = 1, 2$ and 3, and whose kissing number is, for any N, precisely four times that given in the first part of this paper for the number of states in the generic Hilbertian polytopes.

Appendix D

$SU(3)$ Coherent States - Simple Collective Hamiltonians

D.1 Introduction

The $SU(2)$ collective systems are always integrable and most of their physical properties can be obtained following the treatment sketched in Part I of this work. When dealing with higher rank groups, the analysis is complicated by the existence of many degrees of freedom and the fact that the analog classical system exhibits, in general, a chaotic behavior. $SU(3)$ provides a low dimensional model (having 2 of 3 degrees of freedom, depending on the representation) possessing these non-trivial properties. It was used during the 80's and early 90's as a toy model to explore the phenomena of quantum chaos. Compared with other low dimensionality models it has the advantage of having a compact phase space that facilitates the analysis and permits to study the full Hilbert space without need to truncation.

Note that the LMG model has an $SU(3)$ analog, the so-called three-orbital LMG model [17, 139] having a quadratic Hamiltonian in the generators of the $su(3)$ algebra. This model was used to study the classical-quantum correspondence for non-integrable systems [24, 140], in particular through the analysis of the Husimi functions associated with the eigenstates [141, 39], and to test the hypothesis that the level spacings for quantum-chaotic Hamiltonians are characterized by the Gaussian-orthogonal ensamble statistics [139].

In this section we briefly recall the coherent states basis for the fully symmetric irreducible representations of $SU(3)$. They are labeled by an integer n that, as for the $SU(2)$ case, will provide a semi-classical parameter $\hbar = n^{-1}$, a limit case which will not be considered here. This coherent state basis leads to a representation of eigenfunctions in terms of polynomials in two complex variables, in contrast with the $SU(2)$ one-variable Majorana polynomials studied before). We then present a preliminary analysis of simple $SU(3)$ Hamiltonians, which are such that their eigenstates representative polynomials have non generic forms, now characterized by a set of pairs of complex numbers.

D.2 Group structure and Symmetric Representations

The special unitary group of degree 3, denoted $SU(3)$, is the group of 3×3 unitary matrices with determinant 1. Its algebra generators are given for a 3-dimensional representation in a quite simple way: consider the $\mathcal{E}_{i,j}$ as the matrix with entries $[\mathcal{E}_{i,j}]_{k,l} = \delta_{i,k}\delta_{j,l}$, we define the generators of the $su(3)$ algebra as

$$H^i = \mathcal{E}_{i,i} - \mathcal{E}_{i+1,i+1} \qquad \text{for } i = 1,2; \tag{D.1}$$

$$E^{\alpha^{(1)}} = \mathcal{E}_{1,2}\ ; \quad E^{\alpha^{(2)}} = \mathcal{E}_{2,3}\ ; \quad E^{\alpha^{(3)}} = \mathcal{E}_{3,1}\ ; \tag{D.2}$$

$$E^{-\alpha^{(i)}} = (E^{\alpha^{(i)}})^\dagger \qquad \text{for } i = 1,2,3\ ; \tag{D.3}$$

Let us also define $H^3 = H^1 + H^2$. The (representation independant) commutation relations then write in this basis

$$\begin{gathered}\left[H^i, E^{\pm\alpha^{(j)}}\right] = \pm[\alpha^{(j)}]_i E^{\pm\alpha^{(j)}}; \qquad \left[E^{\alpha^{(j)}}, E^{-\alpha^{(j)}}\right] = H^j \\ \left[E^{\pm\alpha^{(1)}}, E^{\pm\alpha^{(2)}}\right] = E^{\pm\alpha^{(3)}}; \quad \left[E^{\pm\alpha^{(1)}}, E^{\mp\alpha^{(3)}}\right] = \mp E^{\mp\alpha^{(2)}}; \quad \left[E^{\pm\alpha^{(2)}}, E^{\mp\alpha^{(3)}}\right] = \mp E^{\pm\alpha^{(1)}};\end{gathered} \tag{D.4}$$

where $[\alpha^{(j)}]_i$ is the i-th component of the root (j) (see Fig. D.1). All the other commutators are zero. The commutation relations in (D.4) are given in the so-called Chevalley basis for a semi-simple Lie algebra (see, for example, [142]).

$SU(3)$ is semi-simple compact group [142], its irreducible representations are fully characterized by the highest-weight $\Lambda = n_1\lambda_1 + n_2\lambda_2$, where λ_i are the fundamental weights which are orthogonal in the Chevalley basis (Fig. D.1-(a)). We are only going to consider the fully symetric irreducible representations of the form $(n_1 = n, n_2 = 0)$ like the ones displayed in Fig. D.1-(b).

The Hilbert space for a system in which $SU(3)$ acts irreducibly throug a fully symmetrical representation $(n,0)$ is spanned by the vectors $\{|\Lambda, \Lambda - k_1\alpha^{(1)} - k_3\alpha^{(3)}\rangle\}$ with $k_1 + k_3 \leq n$, where the first index Λ is the highest weight labeling the representation and the second index labels the state. This space has dimension $\frac{(n+1)(n+2)}{2}$.

D.3 Coherent States

Following the construction by Perelomov [23], we define the coherent states of $SU(3)$ as

$$|\boldsymbol{\tau}\rangle = \mathrm{e}^{\boldsymbol{\tau}.\mathbf{E}_-}|\Lambda,\Lambda\rangle; \tag{D.5}$$

where

$$\mathbf{E}_- = \begin{pmatrix} E^{-\alpha^{(1)}} \\ E^{-\alpha^{(3)}} \end{pmatrix}; \qquad \boldsymbol{\tau} = \begin{pmatrix} \tau_1 & \tau_3 \end{pmatrix}, \tag{D.6}$$

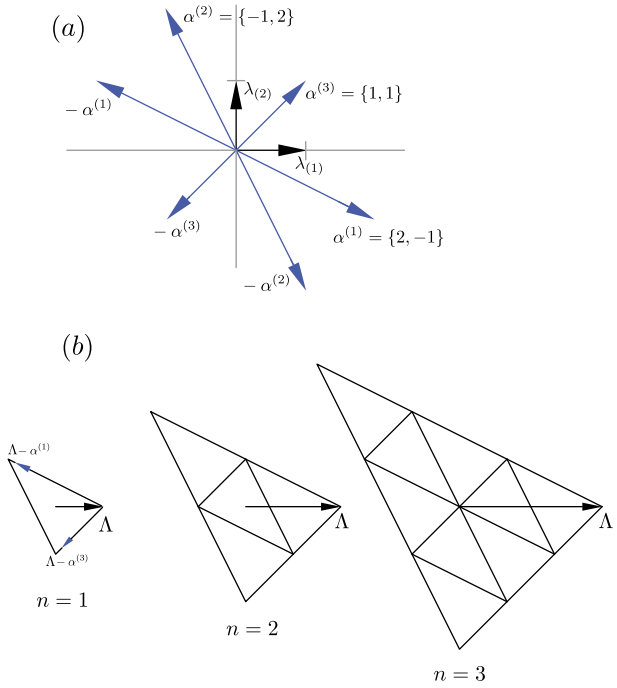

Figure D.1: (a) Root system of the $su(3)$ algebra in the Chevalley basis. (b) Symmetric irreducible representations of $su(3)$ for $(n_1 = n, n_2 = 0)$. The highest weight Λ is represented for $n = 1, 2, 3$.

depending on two complex parameters $\bar{\tau}_1$ and $\bar{\tau}_3$. We also define the conjugated quantities

$$\mathbf{E}_+ = (\mathbf{E}_-)^\dagger = \begin{pmatrix} E^{\alpha^{(1)}} & E^{\alpha^{(3)}} \end{pmatrix}; \qquad \boldsymbol{\tau}^\dagger = \begin{pmatrix} \bar{\tau}_1 \\ \bar{\tau}_3 \end{pmatrix}; \tag{D.7}$$

Acting with the lowering operators $E^{-\alpha^{(i)}}$, the coherent state writes explicitly, in the basis where H^1 and H^2 are diagonal,

$$|\boldsymbol{\tau}\rangle = \sum_{k_1,k_3=0;k_1+k_3\leq n}^{n} \sqrt{\frac{n!}{k_1!k_3!(n-k_1-k_3)!}} \tau_1^{k_1} \tau_3^{k_3} |\Lambda, \Lambda - k_1\alpha^{(1)} - k_3\alpha^{(3)}\rangle. \tag{D.8}$$

Note that, as for $su(2)$, the equation $\langle\boldsymbol{\tau}|\Psi\rangle = 0$ characterizes the state Ψ up to an unphysical constant, but this equation now describe an algebraic surface in $\mathbb{C}^2$. The inner-product of two coherent states is simply given by

$$\langle\boldsymbol{\tau}|\boldsymbol{\tau}'\rangle = \langle\Lambda, \Lambda|\mathrm{e}^{\mathbf{E}_+.\boldsymbol{\tau}^\dagger} \mathrm{e}^{\boldsymbol{\tau}'.\mathbf{E}_-}|\Lambda, \Lambda\rangle = (1 + \boldsymbol{\tau}'.\boldsymbol{\tau}^\dagger)^n. \tag{D.9}$$

Using a Baker-Campbell-Hausdorff-like formula for $su(3)$ [142] (also called Gaussian decomposition formulas [23]) it is possible to obtain representations of the generators of the

algebra in the CS basis

$$H^1 = n - 2\bar{\tau}_1\partial_{\bar{\tau}_1} - \bar{\tau}_3\partial_{\bar{\tau}_3}\ ; \qquad H^2 = \bar{\tau}_1\partial_{\bar{\tau}_1} - \bar{\tau}_3\partial_{\bar{\tau}_3}\ ; \tag{D.10}$$

$$E^{\alpha^{(1)}} = \partial_{\bar{\tau}_1}\ ; \qquad E^{-\alpha^{(1)}} = -\bar{\tau}_1^2\partial_{\bar{\tau}_1} + n\bar{\tau}_1 - \bar{\tau}_3\bar{\tau}_1\partial_{\bar{\tau}_3}; \tag{D.11}$$

$$E^{\alpha^{(2)}} = \bar{\tau}_1\partial_{\bar{\tau}_3}\ ; \qquad E^{-\alpha^{(2)}} = \bar{\tau}_3\partial_{\bar{\tau}_1}\ ; \tag{D.12}$$

$$E^{\alpha^{(3)}} = \partial_{\bar{\tau}_3}\ ; \qquad E^{-\alpha^{(3)}} = -\bar{\tau}_3^2\partial_{\bar{\tau}_3} + n\bar{\tau}_3 - \bar{\tau}_1\bar{\tau}_3\partial_{\bar{\tau}_1}. \tag{D.13}$$

The coherent states form an overcomplete basis. Defining the logarithm of the inner-product

$$\Omega(\boldsymbol{\tau}^\dagger, \boldsymbol{\tau}) = n^{-1}\ln\langle\boldsymbol{\tau}|\boldsymbol{\tau}\rangle \tag{D.14}$$

and the matrix $[\boldsymbol{\omega}]_{i,j} = \partial_{\bar{\tau}_i}\partial_{\tau_j}\Omega$ for $i,j = 1,3$, the closure relation reads

$$\int \mathrm{d}\mu \frac{|\boldsymbol{\tau}\rangle\langle\boldsymbol{\tau}|}{\langle\boldsymbol{\tau}|\boldsymbol{\tau}\rangle} = 1 \tag{D.15}$$

where $\mathrm{d}\mu = (n+1)(n+2)\det(\boldsymbol{\omega})\frac{\mathrm{dRe}\tau_1\ \mathrm{dIm}\tau_1}{\pi}\frac{\mathrm{dRe}\tau_3\ \mathrm{dIm}\tau_3}{\pi}$ with $\det(\boldsymbol{\omega}) = (1+\boldsymbol{\tau}.\boldsymbol{\tau}^\dagger)^{-3}$. The symplectic two-form describing the geometry of the phase space is given by $\omega = [\boldsymbol{\omega}]_{i,j}\,\mathrm{d}\bar{\tau}_i \wedge \mathrm{d}\tau_j$.

D.4 A First Example - Linear Hamiltonians

The simplest type of $su(3)$ Hamiltonians are linear in the generators. Let us briefly describe the eigen-structure of such linear Hamiltonians

$$\hat{H} = \sum_{i=1,2} h_i\ H^i + \sum_{i=1,2,3} \bar{\kappa}_i E^{(\alpha^i)} + \kappa_i E^{(-\alpha^i)}, \tag{D.16}$$

where, in order to respect hermicity, h_i and κ_i are respectively real and complex valued constants. For this case the eigenstates, in the coherent state basis, have the simple form

$$\Psi(\boldsymbol{\tau}^\dagger) = \langle\tau|\Psi\rangle = \left(1+\boldsymbol{\tau}^\dagger.\boldsymbol{\tau}^{(1)}\right)^{k_1}\left(1+\boldsymbol{\tau}^\dagger.\boldsymbol{\tau}^{(2)}\right)^{k_2}\left(1+\boldsymbol{\tau}^\dagger.\boldsymbol{\tau}^{(3)}\right)^{k_3} \tag{D.17}$$

with $k_1, k_2, k_3 \in \mathbb{N}$, $k_1+k_2+k_3 = n$ and $\boldsymbol{\tau}^{(i)} = \{\tau_1^{(i)}, \tau_3^{(i)}\}$ being three couples of complex numbers characterizing the state. This decomposition arises because this type of Hamiltonians can always be written brought to the diagonal form

$$R\hat{H}R^\dagger = \sum_{i=1,2} \tilde{h}_i\ H^i \tag{D.18}$$

by a suitable unitary transformation $R = \mathrm{e}^{\sum_i t_i T^i}$, where T^i are the generators of $su(3)$ defined in (D.1 - D.3). Indeed in the rotated basis the eigen-energies are given by

$$\varepsilon = (\Lambda - k_1\alpha^{(1)} - k_3\alpha^{(3)}).\tilde{\mathbf{h}} = (n-2k_1-k_3)\tilde{h}_1 + (k_1-k_3)\tilde{h}_2 \tag{D.19}$$

$$= \varepsilon_1 k_1 + \varepsilon_2 k_2 + \varepsilon_3 k_3, \tag{D.20}$$

where the extremal energies $\varepsilon_1 = (-\tilde{h}_1 + \tilde{h}_2), \varepsilon_2 = \tilde{h}_1, \varepsilon_3 = -\tilde{h}_2$ correspond respectively to the energies of the extremal states $(k_1 = n, k_3 = 0), (k_1 = 0, k_3 = 0), (k_1 = 0, k_3 = n)$ divided by n. The eigenstates in the rotated basis are simply given by

$$\tilde{\Psi}(\boldsymbol{\tau}^\dagger) = \langle \boldsymbol{\tau} | \Lambda, \Lambda - k_1\alpha^{(1)} - k_3\alpha^{(3)} \rangle \propto \bar{\tau}_1^{k_1} \bar{\tau}_3^{k_3}. \tag{D.21}$$

Inserting the state (D.17) as an ansatz eigenstate for the linear Hamiltonian (D.16) and using the above given coherent state representation of the generators, it is easy to obtain the values of $\boldsymbol{\tau}^{(i)}$'s

$$\boldsymbol{\tau}^{(i)} = \begin{pmatrix} -\frac{h_2\bar{\kappa}_1 + \varepsilon_i\bar{\kappa}_1 + \kappa_2\bar{\kappa}_3}{h_2^2 - h_1h_2 - \varepsilon_i^2 - h_1\varepsilon_i + \kappa_2\bar{\kappa}_2} \\ -\frac{-\bar{\kappa}_1\bar{\kappa}_2 - h_1\bar{\kappa}_3 + h_2\bar{\kappa}_3 - \varepsilon_i\bar{\kappa}_3}{-h_2^2 + h_1h_2 + \varepsilon_i^2 + h_1\varepsilon_i - \kappa_2\bar{\kappa}_2} \end{pmatrix} \tag{D.22}$$

where the ε_i's are given as the roots of the equation

$$\left[-h_2h_1^2 + \left(h_2^2 + \kappa_2\bar{\kappa}_2 - \kappa_3\bar{\kappa}_3\right)h_1 - \bar{\kappa}_1\left(h_2\kappa_1 + \kappa_3\bar{\kappa}_2\right) + \left(h_2\kappa_3 - \kappa_1\kappa_2\right)\bar{\kappa}_3\right] + \tag{D.23}$$

$$\left(-h_1^2 + h_2h_1 - h_2^2 - \kappa_1\bar{\kappa}_1 - \kappa_2\bar{\kappa}_2 - \kappa_3\bar{\kappa}_3\right)\varepsilon + \varepsilon^3 = 0 \tag{D.24}$$

where the three solutions add to zero : $\varepsilon_1 + \varepsilon_2 + \varepsilon_3 = 0$. The simple form (D.17) of the eigenstates is due to the fact that the rotation operator R keeps invariant the form (D.17), changing only the values of the complex contants $\boldsymbol{\tau}^{(i)}$; the eigenstates in the rotated basis are just particular simple states of that form.

These types of Hamiltonian are simple in relation with the fact that they commute with any operator of the type $A = \sum_{i=1,2} \tilde{a}_i \; R^\dagger H^i R$. It is interesting here that, as with the Majorana representation for $SU(2)$ states, it is still possible to represent the eigenstates by a set of points on spheres (2 spheres in the present case). Indeed, the above particular form of the eigenvectors allows us to represent them by three points in $\mathbb{C}^2$ together with their multiplicities k_1 and k_3. Each point in $\mathbb{C}^2$ is a couple of complex numbers, which we can represent (with a double stereographic map) as corresponding points on two separate spheres S^2, as shown for example in Fig. (D.2).

D.5 Eigenstates for another Simple Class of Hamiltonians

Let us consider an $su(3)$ Hamiltonian $\hat{H}$ that commutes with a special element $F = (H^1 - H^2)$ of the $su(3)$ algebra. This implies that $\hat{H}$ couples only states with the same value of $H^1 - H^2$ like in Fig. D.3, i.e. it couples states with the same powers of $\bar{\tau}_1$. We can

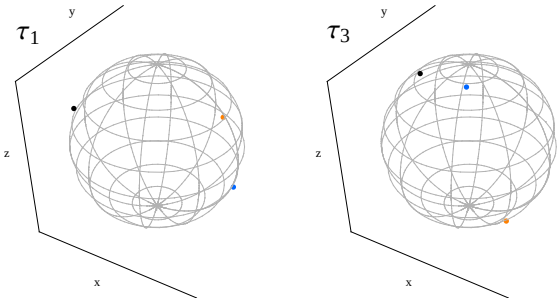

Figure D.2: Couples $\boldsymbol{\tau}_i = \{\tau_1^{(i)}, \tau_3^{(i)}\}$ characterizing the eigen-structure of a linear Hamiltonian, $\{h_1 = 4, h_2 = 5, \kappa_1 = 4 + 2i, \kappa_2 = 1 + 2i, \kappa_3 = 3\}$.

show that the $\hat{H}$ eigenstates factorizes to

$$\tilde{\Psi}(\boldsymbol{\tau}^\dagger) = C\,\bar{\tau}_1^k \prod_{i=1}^{n-k} \left(1 + \bar{\tau}_3 \tau_3^{(i)}\right), \tag{D.25}$$

where C is a non-physical constant and $\tau_3^{(i)}$ are $n-k$ complex numbers. We shall below that these states keeps a rather simple form in any rotated basis.

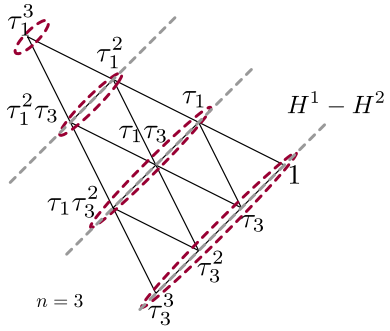

Figure D.3: Coupling matrix elements of an Hamiltonian $\hat{H}$ that commutes with $H^1 - H^2$. Each node corresponds to the basis vectors such that H^1 and H^2 are diagonal which, in the coherent state representation, leads to a polynomial form $\bar{\tau}_1^k \bar{\tau}_3^{k'}$. The matrix elements of $\hat{H}$ couple only states with the same values of $H^1 - H^2$ and thus the eigenstates can be written as in Eq. (D.25).

A simple Hamiltonian having this property is, for example, given by

$$\hat{H} = \sum_{i=1,2} h_i H^i + \sum_{i=1,2} \lambda_i [H^i]^2 + \kappa_3 E^{(\alpha^3)} + \bar{\kappa}_3 E^{(-\alpha^3)} + m_3 [E^{(\alpha^3)}]^2 + \bar{m}_3 [E^{(-\alpha^3)}]^2. \tag{D.26}$$

This construction works for an operator $F = f_1 H^1 + f_2 H^2$ for which $\mathbf{f}.\alpha^{(i)} = 0$ for one of the roots $i = 1, 2, 3$, which means couplings along one the direction prallel to the side

of the representative triangle. These operators have the particular property of being the only linear operators, diagonal in the (H^1,H^2) basis, such that their extremal eigenvalues ε_i, defined in the previous section, verify $\varepsilon_i = \varepsilon_j = -2\varepsilon_k$ for some triplet $i, j, k = 1, 2, 3$.

Using a simple rotation $R = \mathrm{e}^{-\mathrm{i}\sum_i t_i T^i}$, where T^i's stand for the algebra generators, we can perform the transformation $\tilde{F} = R^{-1}FR$. R is indeed an element of the group $SU(3)$, as it is the exponential of some element of the algebra $T = \sum_i t_i T^i$ with $T^\dagger = T$. Using the Baker-Campbell-Hausdorff relations, it can be decomposed as

$$R = \prod_i \mathrm{e}^{\tilde{t}_i T^i}, \tag{D.27}$$

for some constants $\tilde{t}_i$. We need to describe the action of each "decomposed" rotation e^{tT^i} on a general state $\Psi(\boldsymbol{\tau}^\dagger) = \Psi(\bar{\tau}_1, \bar{\tau}_3)$. Using the differential form of the generators, we obtain

$T^{(i)}$	$\tilde{\Psi}(\bar{\tau}_1, \bar{\tau}_3) = \mathrm{e}^{tT^i}\Psi(\bar{\tau}_1, \bar{\tau}_3)$
H^1	$\tilde{\Psi}(\bar{\tau}_1, \bar{\tau}_3) = e^{tn}\Psi(e^{-2t}\bar{\tau}_1, e^{-t}\bar{\tau}_3)$
H^2	$\tilde{\Psi}(\bar{\tau}_1, \bar{\tau}_3) = \Psi(e^{t}\bar{\tau}_1, e^{-t}\bar{\tau}_3)$
$E^{(\alpha^1)}$	$\tilde{\Psi}(\bar{\tau}_1, \bar{\tau}_3) = \Psi(t + \bar{\tau}_1, \bar{\tau}_3)$
$E^{(-\alpha^1)}$	$\tilde{\Psi}(\bar{\tau}_1, \bar{\tau}_3) = (t\bar{\tau}_1 + 1)^n \Psi\left(\frac{\bar{\tau}_1}{t\bar{\tau}_1+1}, \frac{\bar{\tau}_3}{t\bar{\tau}_1+1}\right)$.
$E^{(\alpha^2)}$	$\tilde{\Psi}(\bar{\tau}_1, \bar{\tau}_3) = \Psi(\bar{\tau}_1, t\bar{\tau}_1 + \bar{\tau}_3)$
$E^{(-\alpha^2)}$	$\tilde{\Psi}(\bar{\tau}_1, \bar{\tau}_3) = \Psi(\bar{\tau}_1 + t\bar{\tau}_3, \bar{\tau}_3)$
$E^{(\alpha^3)}$	$\tilde{\Psi}(\bar{\tau}_1, \bar{\tau}_3) = \Psi(\bar{\tau}_1, t + \bar{\tau}_3)$
$E^{(-\alpha^3)}$	$\tilde{\Psi}(\bar{\tau}_1, \bar{\tau}_3) = (t\bar{\tau}_3 + 1)^n \Psi\left(\frac{\bar{\tau}_1}{t\bar{\tau}_3+1}, \frac{\bar{\tau}_3}{t\bar{\tau}_3+1}\right)$

(D.28)

It is then simple to observe that these transformations keep invariant the polynomial form

$$\Psi(\boldsymbol{\tau}^\dagger) = C\prod_{i=1}^{n}\left(1 + \boldsymbol{\tau}^\dagger.\boldsymbol{\tau}^{(i)}\right), \tag{D.29}$$

changing only the pairs of complex numbers $\boldsymbol{\tau}^{(i)} = \{\tau_1^{(i)}, \tau_3^{(i)}\}$ that characterize the state and the non-physical constant C. Note that the state (D.25) is also a state of that form.

Suppose now that an Hamiltonian $\tilde{H}$ commutes with an element of the algebra $\tilde{F}$ having $\varepsilon_i = \varepsilon_j = -2\varepsilon_k$. This implies that all eigenstates of $\tilde{H}$ are of the form (D.29) because we can always perform a rotation R^{-1} that sends $\tilde{H}$ to $\hat{H}$ and $\tilde{F}$ to F.

The $\Psi(\boldsymbol{\tau}^\dagger) = 0$ equation characterizing these types of states leads to a simple surface $\cup_i\{\boldsymbol{\tau}^\dagger : (1 + \boldsymbol{\tau}^\dagger.\boldsymbol{\tau}^{(i)}) = 0\}$. This is in contrast with generic states that cannot be written in the form (D.29) and are thus characterized by a more complicated surface.

If the Hamiltonian is known to commute with some $\tilde{F}$, and thus its eigenstates are of the form (D.29), the equations for the values of the couples $\{\tau_1^{(i)}, \tau_3^{(i)}\}$ can be obtained in a similar way as in the $su(2)$ case. Consider the Riccati-like equation for $S(\boldsymbol{\tau}^\dagger) = \sum_i \ln\left(1 + \boldsymbol{\tau}^\dagger.\boldsymbol{\tau}^{(i)}\right)$ and evaluate it both in $\boldsymbol{\tau}^\dagger \to \{-\frac{1}{\tau_1^{(i)}}, 0\}$ and $\boldsymbol{\tau}^\dagger \to \{0, -\frac{1}{\tau_3^{(i)}}, \}$. The result is a set of $2n$ coupled non-linear equations that are obtained by canceling the poles in the right-hand side of the expressions

$$\mathcal{H}[\boldsymbol{\tau}^\dagger, \boldsymbol{\partial}_{\boldsymbol{\tau}^\dagger} S(\boldsymbol{\tau}^\dagger) + n^{-1}\boldsymbol{\partial}_{\boldsymbol{\tau}^\dagger}]\Big|_{\boldsymbol{\tau}^\dagger \to \{-\frac{1}{\tau_1^{(i)}}, 0\}} = \varepsilon, \tag{D.30}$$

$$\mathcal{H}[\boldsymbol{\tau}^\dagger, \boldsymbol{\partial}_{\boldsymbol{\tau}^\dagger} S(\boldsymbol{\tau}^\dagger) + n^{-1}\boldsymbol{\partial}_{\boldsymbol{\tau}^\dagger}]\Big|_{\boldsymbol{\tau}^\dagger \to \{0, -\frac{1}{\tau_3^{(i)}}\}} = \varepsilon, \tag{D.31}$$

for $i = 1, ..., n$. The solutions of the pole cancellation conditions correspond to eigenstates of the Hamiltonian. As before, the energy can be obtained easily, once these equations are solved, by evaluating the Riccati-like equation on a regular value of $\boldsymbol{\tau}^\dagger$. This method was tested numerically for eigenstates of a quadratic-$su(3)$ Hamiltonian similar the one in D.26. A typical distribution of the $\boldsymbol{\tau}_i$'s is displayed in Fig. D.4. In order to show the non-triviality of such distribution we also show in Fig. D.5 the superposition of the $\boldsymbol{\tau}^{(i)}$ corresponding to all the eigenstates of the Hamiltonian. Even if we think that, in practice, this is not an efficient method to obtain the eigenstates of the system, it may prove usefull in the limit $n \to \infty$. Indeed, since the $\boldsymbol{\tau}^{(i)}$'s code the sets $\Psi(\boldsymbol{\tau}^\dagger) = 0$, we expect that they lay along (eventually complicated) lines, as in the $SU(2)$ case and as it was found in other integrable systems in the literature (see, for example, [40, 143]). Note that, if the Hamiltonian is not of the class specified above, we can always write the equations in (D.30), but the solutions, if they exit, will not uniquely characterize the state.

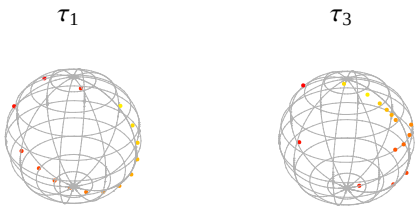

Figure D.4: Inverse stereographic projection of the $\boldsymbol{\tau}^{(i)}$'s characterizing one eigenstate of a simple quadratic-$SU(3)$ Hamiltonian for $n = 15$. The colors label the couples $\{\tau_1^{(i)}, \tau_3^{(i)}\}$.

Let us now consider the more complicate case of a Hamiltonian $\hat{H}$ commuting with some $F = f_1 H^1 + f_2 H^2$ operator having $\mathbf{f}.\mathbf{u} = 0$ with $\mathbf{u} = u_1\alpha^{(1)} + u_3\alpha^{(3)}$ for some integers

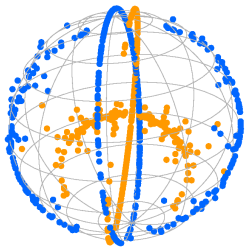

Figure D.5: Superposition of the values of $\boldsymbol{\tau}^{(i)}$'s characterizing all eigenstates of a quadratic-$SU(3)$ Hamiltonian for $n = 8$. The orange and blue dots are respectively the inverse stereographic projections of the $\tau_1^{(i)}$'s and the $\tau_3^{(i)}$'s.

u_1 and u_3. We can take as example the case $u_1 = -2, u_3 = 3$ yielding $\mathbf{u} = \{-1, 1\}$, see Fig. (D.6). The fact that an element of the (H^1, H^2) basis is an eigenstates of F, with eigenvalue a, writes

$$\begin{aligned} F|\Lambda, \Lambda - k_1\alpha^{(1)} - k_3\alpha^{(3)}\rangle &= \mathbf{f}.(\Lambda - k_1\alpha^{(1)} - k_3\alpha^{(3)})|\Lambda, \Lambda - k_1\alpha^{(1)} - k_3\alpha^{(3)}\rangle \quad \text{(D.32)} \\ &= a|\Lambda, \Lambda - k_1\alpha^{(1)} - k_3\alpha^{(3)}\rangle, \quad \text{(D.33)} \end{aligned}$$

i.e. $k_3 = \frac{nf_1 - a}{f_1+f_2} + \frac{(f_2-2f_1)k_1}{f_1+f_2}$. Note that states $|\Lambda, \lambda\rangle$ and $|\Lambda, \lambda + k\mathbf{u}\rangle$ have the same eigenvalue a since $\mathbf{f}.\mathbf{u} = 0$. The choice of $\mathbf{u}$ leads to a foliation of the representative triangle into chains of states (along dotted lines in the figure)connecting states sharing the same eigenvalue a

Let us chose k_1, k_3 such that the state $|\Lambda, \Lambda - k_1\alpha^{(1)} - k_3\alpha^{(3)}\rangle$ is an eigenvector of F, with eigenvalue a, and also such that the state $|\Lambda, \Lambda - k_1\alpha^{(1)} - k_3\alpha^{(3)} + \mathbf{u}\rangle$ does not belong to the representation. This state is at one end of the chain as in Fig.(D.6); the state at the other end of the chain is obtained by acting m times with a $\mathbf{u}$ translation. A general eigenstate of an Hamiltonian commuting with F writes, in the CS basis,

$$\begin{aligned} \Psi(\boldsymbol{\tau}^\dagger) &= \bar{\tau}_1^{k_1}\bar{\tau}_3^{k_3}\sum_{k=0}^{m} c_k(\bar{\tau}_1^{u_1}\bar{\tau}_3^{u_3})^k \quad \text{(D.34)} \\ &= C\bar{\tau}_1^{k_1}\bar{\tau}_3^{k_3}\prod_{i=1}^{m}\left(1 + \tau^{(i)}\bar{\tau}_1^{u_1}\bar{\tau}_3^{u_3}\right), \quad \text{(D.35)} \end{aligned}$$

for m constants $\tau^{(i)} \in \mathbb{C}$ characterizing the state and some non-physical constant C. Note that we can always chose u_1 to be positive and so u_3 can be a positive or negative integer. In case $u_3 < 0$ we can rewrite the polynomial (D.34) as

$$\Psi(\boldsymbol{\tau}^\dagger) = C\bar{\tau}_1^{k_1}\bar{\tau}_3^{k_3+mu_3}\prod_{i=1}^{m}\left(\bar{\tau}_3^{-u_3} + \tau^{(i)}\bar{\tau}_1^{u_1}\right). \quad \text{(D.36)}$$

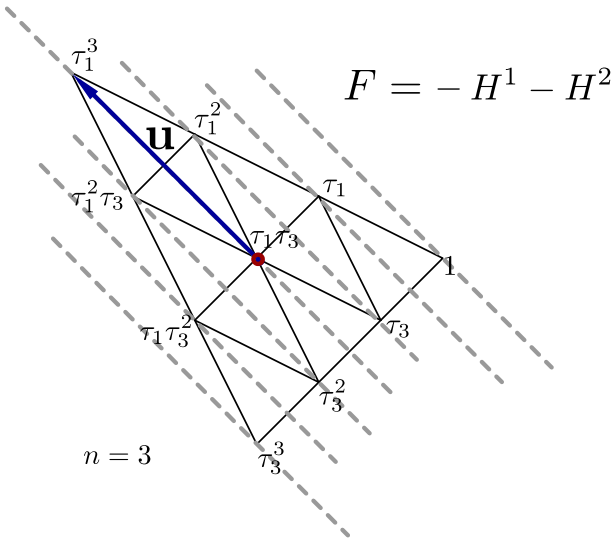

Figure D.6: Coupling matrix elements of an Hamiltonian $\hat{H}$ that commutes with $F = -H^1 - H^2$. The states that differ by $\mathbf{u}$ are coupled by the Hamiltonian. The state marked by the red dot is the initial state in the extremity of the chain.

Performig a R rotation the states Ψ transform to

$$\tilde{\Psi}(\boldsymbol{\tau}^\dagger) \;=\; \prod_{i=1}^{m} p_i(\bar{\tau}_1, \bar{\tau}_3), \tag{D.37}$$

where $p_i(\bar{\tau}_1, \bar{\tau}_3)$ are polynomials of maximal degree $d = \max\{u_1, u_3, u_1 + u_3\}$, which still remain to be better characterized. Note that we expect that the complexity of the surface $\Psi(\boldsymbol{\tau}^\dagger) = 0$ will increase with $|\mathbf{u}|$.

D.6 Discussion and Conclusion

In this appendix, we have performed a preliminary study about the algebraic structure of the eigenstates of simple $SU(3)$-Hamiltonians (integrable in the sense of [24, 140]). Our aim was in particular to find simple models, in the framework of $SU(3)$ coherent state representation, about which some characterization of the eigenstate structure could be done.

Indeed, for the most generic integrable systems, the eigenstates are associated with quantized invariant tori and the classical actions of these tori provide a complete set of good quantum numbers for the quantization rules [24, 140]. But, even if the quantization in such cases is understood, the structure of the eigenfunctions are in general rather complex.

We first treated the rather trivial case of "linear" Hamiltonians, for which the eign-states are the product of first order polynomials. We then introduced a particular class

of $SU(3)$-Hamiltonians, whose eigenstates, in the coherent state basis, belong to a simple family of polynomials parametrized by couples of complex numbers. In that case, a set of algebraic relations can be derived for these complex couples. We finally tried to generalize this treatment to other classes of simple Hamiltonians, leading to still non generic, but nevertheless more complex, polynomial forms for the eigenstates.

An interesting perspective would be to study this system in the semi-classical limit, where $n \to \infty$. In particular, we would like to check whether a generalization of the method used in the $SU(2)$ case, may provide spectral details of these types of model.

Bibliography

[1] S. Sachdev. *Quantum Phase Transitions*. Cambridge University Press, 1999.

[2] R. Gilmore and D. H. Feng. Phase transitions in nuclear matter described by pseudospin hamiltonians. *Nucl. Phys. A*, 301:189–204, 1978.

[3] J. P. Elliott. The interacting boson model of nuclear structure. *Rep. Prog. Phys.*, 48:171–222, 1985.

[4] Da Hsuan Feng, R. Gilmore, and S. R. Deans. Phase transitions and the geometric properties of the interacting boson model. *Phys. Rev. C*, 23:1254–1258, 1981.

[5] P. Cejnar, S. Heinze, and J. Jolie. Ground-state shape phase transitions in nuclei: Thermodynamic analogy and finite-n effects. *Phys. Rev. C*, 68:034326, 2003.

[6] J. I. Cirac, M. Lewenstein, K. Mølmer, and P. Zoller. Quantum superposition states of bose-einstein condensates. *Phys. Rev. A*, 57:1208–1218, 1998.

[7] J. I. Cirac P. Zoller A. Sorensen, L.-M. Duan. Many-particle entanglement with bose–einstein condensates. *Nature*, 409:63–66, 2001.

[8] S. Morrison and A. S. Parkins. Collective spin systems in dispersive optical cavity qed: Quantum phase transitions and entanglement. *Phys. Rev. A*, 77:043810, 2008.

[9] M. Vojta. Quantum phase transitions. *Rep. Prog. Phys.*, 66:2069–2110, 2003.

[10] W. D. Heiss and M. Müller. Universal relationship between a quantum phase transition and instability points of classical systems. *Phys. Rev. E*, 66:016217, 2002.

[11] W. D. Heiss, F. G. Scholtz, and H. B. Geyer. The large n behaviour of the lipkin model and exceptional points. *J. Phys. A*, 38:1843–1851, 2005.

[12] F. Leyvraz and W. D. Heiss. Large-n scaling behavior of the lipkin-meshkov-glick model. *Phys. Rev. Lett.*, 95:050402, 2005.

[13] M.A. Caprio, P. Cejnar, and F. Iachello. Excited state quantum phase transitions in many-body systems. *Ann. Phys.*, 323:1106–1135, 2008.

[14] P. Ribeiro, J. Vidal, and R. Mosseri. The thermodynamical limit of the lipkin-meshkov-glick model. *Phys. Rev. Lett.*, 99:050402, 2007.

[15] A. V. Turbiner. Quasi-exactly-solvable problems and sl(2) algebra. *Commun. Math. Phys.*, 118:467–474, 1988.

[16] V. V. Ulyanov and O. B. Zaslavskii. New methods in the theory of quantum spin systems. *Phys. Rep.*, 216:179–251, 1992.

[17] H. J. Lipkin, N. Meshkov, and A. J. Glick. Validity of many-body approximation methods for a solvable model : (i). exact solutions and perturbation theory. *Nucl. Phys.*, 62:188–198, 1965.

[18] D. A. Garanin, X. Martínez Hidalgo, and E. M. Chudnovsky. Quantum-classical transition of the escape rate of a uniaxial spin system in an arbitrarily directed field. *Phys. Rev. B*, 57:13639–13654, 1998.

[19] J. Vidal, G. Palacios, and R. Mosseri. Entanglement in a second-order quantum phase transition. *Phys. Rev. A*, 69:022107, 2004.

[20] J. Vidal, R. Mosseri, and J. Dukelsky. Entanglement in a first-order quantum phase transition. *Phys. Rev. A*, 69:054101, 2004.

[21] J. Kurchan, P. Leboeuf, and M. Saraceno. Semiclassical approximations in the coherent-state representation. *Phys. Rev. A*, 40:6800–6813, 1989.

[22] L. G. Yaffe. Large n limits as classical mechanics. *Rev. Mod. Phys.*, 54:407–435, 1982.

[23] A. Perelomov. *Generalized Coherent States and Their Applications*. Springer-Verlag Berlin and Heidelberg New York, 1986.

[24] W.-M. Zhang, Da H. Feng, and R. Gilmore. Coherent states: Theory and some applications. *Rev. Mod. Phys.*, 62:867–927, 1990.

[25] E. Majorana. Atomi orientati in campo magnetico variabile. *Nuovo Cimento*, 9:43, 1932.

[26] A. Voros. Wentzel-kramers-brillouin method in the bargmann representation. *Phys. Rev. A*, 40:6814–6825, 1989.

[27] A. Garg and M. Stone. Bohr-sommerfeld quantization of spin hamiltonians. *Phys. Rev. Lett.*, 92:010401, 2004.

[28] R. Shankar. Bohr-sommerfeld quantization of pseudospin hamiltonians. *Phys. Rev. Lett.*, 45:1088–1091, 1980.

[29] J. N. L. Connor. On the semiclassical approximation for double well potentials. *Chem. Phys. Lett.*, 4:419–420, 1969.

[30] P. M. Bleher. Semiclassical quantization rules near separatrices. *Commun. Math. Phys.*, 165:621–640, 1994.

[31] Y. Colin de Verdière and B. Parisse. Équilibre instable en régime semi-classique. I. Concentration microlocale. *Comm. Partial Differential Equations*, 19:1535–1563, 1994.

[32] Y. Colin de Verdière and B. Parisse. Singular bohr?sommerfeld rules. *Commun. Math. Phys.*, 205:459–500, 1999.

[33] J. R. Klauder. The action option and a feynman quantization of spinor fields in terms of ordinary c-numbers. *Ann. Phys.*, 11:123–168, 1960.

[34] Roy J. Glauber. The quantum theory of optical coherence. *Phys. Rev.*, 130:2529–2539, 1963.

[35] A. M. Perelomov. Coherent states for arbitrary lie group. *Commun. Math. Phys.*, 26:222–236, 1972.

[36] R. Gilmore. Geometry of symmetrized states. *Ann. Phys.*, 74:391–463, 1972.

[37] R. Gilmore. Baker-campbell-hausdorff formulas. *J. Math. Phys.*, 15:2090–2092, 1974.

[38] K. Husimi. *Proc. Phys. Math. Soc. Jpn.*, 22:264, 1940.

[39] P. Leboeuf and M. Saraceno. Eigenfunctions of non-integrable systems in generalised phase spaces. *J. Phys. A*, 23:1745–1764, 1990.

[40] P. Leboeuf and A. Voros. Chaos-revealing multiplicative representation of quantum eigenstates. *J. Phys. A*, 23:1765–1774, 1990.

[41] G. Wentzel. A generalisation of the quantum constraints for the purposes of the wave mechanics. *Zeits. f. Phys.*, 38:518–529, 1962.

[42] L. Brillouin. The ondulatory mechanics of schrodinger; a general method of resolution by successive approximations. *Comptes Rendus*, 183:24–27, 1926.

[43] H. A. Kramers. Wave mechanics and half-integral quantisation. *Zeits. f. Phys.*, 39:828–840, 1962.

[44] V. Bargmann. On a hilbert space of analytic functions and an associated integral transform part i. *Commun. Pure Appl. Math.*, 14:187, 1961.

[45] N. Meshkov, A. J. Glick, and H. J. Lipkin. Validity of many-body approximation methods for a solvable model : (ii). linearization procedures. *Nucl. Phys.*, 62:199–210, 1965.

[46] A. J. Glick, H. J. Lipkin, and N. Meshkov. Validity of many-body approximation methods for a solvable model : (iii). diagram summations. *Nucl. Phys.*, 62:211–224, 1965.

[47] S. Morrison and A. S. Parkins. Dynamical quantum phase transitions in the dissipative lipkin-meshkov-glick model with proposed realization in optical cavity qed. *Phys. Rev. Lett.*, 100:040403, 2008.

[48] Y. Hamdouni and F. Petruccione. Time evolution and decoherence of a spin-(1/2) particle coupled to a spin bath in thermal equilibrium. *Phys. Rev. B*, 76:174306, 2007.

[49] H. T. Quan, Z. D. Wang, and C. P. Sun. Quantum critical dynamics of a qubit coupled to an isotropic lipkin-meshkov-glick bath. *Phys. Rev. A*, 76:012104, 2007.

[50] A. Das, K. Sengupta, D. Sen, and B. K. Chakrabarti. Infinite-range ising ferromagnet in a time-dependent transverse magnetic field: Quench and ac dynamics near the quantum critical point. *Phys. Rev. B*, 74:144423, 2006.

[51] J. Vidal, G. Palacios, and C. Aslangul. Entanglement dynamics in the lipkin-meshkov-glick model. *Phys. Rev. A*, 70:062304, 2004.

[52] J. I. Latorre, R. Orus, E. Rico, and J. Vidal. Entanglement entropy in the lipkin-meshkov-glick model. *Phys. Rev. A*, 71:064101, 2005.

[53] R. G. Unanyan, C. Ionescu, and M. Fleischhauer. Many-particle entanglement in the gaped antiferromagnetic lipkin model. *Phys. Rev. A*, 72:022326, 2005.

[54] T. Barthel, S. Dusuel, and J. Vidal. Entanglement entropy beyond the free case. *Phys. Rev. Lett.*, 97:220402, 2006.

[55] J. Vidal, S. Dusuel, and T. Barthel. Entanglement entropy in collective models. *J. Stat. Mech. : Theor. Exp.*, 2007:P01015, 2007.

[56] H.-M. Kwok, W.-Q. Ning, S.-J. Gu, and H.-Q. Lin. Quantum criticality of the lipkin-meshkov-glick model in terms of fidelity susceptibility, 2007. arXiv:0710.2581.

[57] H. T. Cui. Multiparticle entanglement in the lipkin-meshkov-glick model. *Phys. Rev. A*, 77:052105, 2008.

[58] S. Dusuel and J. Vidal. Finite-size scaling exponents of the lipkin-meshkov-glick model. *Phys. Rev. Lett.*, 93:237204, 2004.

[59] S. Dusuel and J. Vidal. Continuous unitary transformations and finite-size scaling exponents in the lipkin-meshkov-glick model. *Phys. Rev. B*, 71(2):224420, 2005.

[60] G. Rosensteel, D. J. Rowe, and S. Y. Ho. Equations of motion for a spectrum-generating algebra: Lipkin-meshkov-glick model. *J. Phys. A*, 41:025208, 2008.

[61] F. Pan and J. P. Draayer. Analytical solutions for the lmg model. *Phys. Lett. B*, 451:1–10, 1999.

[62] J. Links, H.-Q. Zhou, R. H. McKenzie, and M. D. Gould. Algebraic bethe ansatz method for the exact calculation of energy spectra and form factors: applications to models of bose–einstein condensates and metallic nanograins. *J. Phys. A*, 36:R63–R104, 2003.

[63] G. Ortiz, R. Somma, J. Dukelsky, and S. Rombouts. Exactly-solvable models derived from a generalized gaudin algebra. *Nucl. Phys. B*, 707:421–457, 2005.

[64] R. Botet, R. Jullien, and P. Pfeuty. Size scaling for infinitely coordinated systems. *Phys. Rev. Lett.*, 49:478–481, 1982.

[65] R. Botet and R. Jullien. Large-size critical behavior of infinitely coordinated systems. *Phys. Rev. B*, 28:3955–3967, 1983.

[66] Alan Dzhioev, Z. Aouissat, A. Storozhenko, A. Vdovin, and J. Wambach. Extended holstein-primakoff mapping for the next-to-leading order of the 1/n expansion at finite temperature. *Phys. Rev. C*, 69:014318, 2004.

[67] Gang Chen and J-Q Liang. Unconventional quantum phase transition in the finite-size lipkin–meshkov–glick model. *New J. Phys.*, 8:297, 2006.

[68] A. Kuriyama, M. Yamamura, C. Providência, J. da Providência, and Y. Tsue. The lipkin model. beyond mean field with generalized coherent states. *J. Phys. A*, 36:10361–10372, 2003.

[69] W. D. Heiss. On the thermodynamic limit of the lipkin model. *J. Phys. A*, 39:10081–10086, 2006.

[70] O. Castanos, R. Lopez-Pena, J. G. Hirsch, and E. Lopez-Moreno. Classical and quantum phase transitions in the lipkin-meshkov-glick model. *Phys. Rev. B*, 74:104118, 2006.

[71] P. Ribeiro, J. Vidal, and R. Mosseri. Exact spectrum of the lipkin-meshkov-glick model in the thermodynamic limit and finite-size corrections. *Phys. Rev. E*, 78:021106, 2008.

[72] T. Paul and A. Uribe. A construction of quasi-modes using coherent states. *Ann. de l'Institut Henri Poincaré-Physique Théorique*, 59:357, 1993.

[73] J. J. Morehead. Semiclassical integrable matrix elements. *Phys. Rev. A*, 53:1285–1294, 1996.

[74] I.S. Gradshteyn and I.M. Ryzhik. *Table of Integrals, Series and Product.* Academic Press, New-York, 1980.

[75] P. Ribeiro, P. Solinas, and R. Mosseri. In preparation.

[76] S. Nonnenmacher and A. Voros. Eigenstate structures around a hyperbolic point. *J. Phys. A*, 30:295–315, 1997.

[77] J. R. Cary and P. Rusu. Quantum dynamics near a classical separatrix. *Phys. Rev. A*, 47:2496–2505, 1993.

[78] P. Benioff. The computer as a physical system: A microscopic quantum mechanical hamiltonian model of computers as represented by Turing machines. *J. Stat. Phys.*, 22:563–591, 1980.

[79] P. Benioff. Quantum mechanical models of Turing machines that dissipate no energy. *Phys. Rev. Lett.*, 48:1581–1585, 1982.

[80] R. P. Feynman. Simulating physics with computers. *Int. J. of Theor. Phys.*, 21:467, 1982.

[81] D. Deutsch. Quantum theory, the Church-Turing principle and the universal quantum computer. *Proc. R. Soc. Lond. A*, 400:97–117, 1985.

[82] P. W. Shor. Algorithms for quantum computation: Discrete logarithms and factoring. In S. Goldwasser, editor, *Proceedings of the 35th Annual Symposium on the Foundations of Computer Science (FOCS'94)*, pages 124–134, Los Alamitos, CA, 1994. IEEE Computer Society.

[83] P. W. Shor. Polynomial-time algorithms for prime factorization and discrete logarithms on a quantum computer. *SIAM J. Comput.*, 26:1484–1509, 1997.

[84] M. A. Nielsen and I. L. Chuang. *Quantum Computation and Quantum Information*. Cambridge University Press, October 2000.

[85] E. Farhi, J. Goldstone, S. Gutmann, and M. Sipser. Quantum computation by adiabatic evolution, 2000. quant-ph/0001106.

[86] A. Messiah. *Quantum Mechanics*, volume II. Amsterdam: North Holland, New York: Wiley, 1976.

[87] Wim van Dam, Michele Mosca, and Umesh Vazirani. How powerful is adiabatic quantum computation? In *FOCS'01: Proceedings of the 42nd Annual IEEE Symposium on Foundations of Computer Science (FOCS'01)*, pages 279–287, Washington, DC, USA, 2001. IEEE Computer Society.

[88] D. Aharonov, W. van Dam, J. Kempe, Z. Landau, S. Lloyd, and O. Regev. Adiabatic quantum computation is equivalent to standard quantum computation. In *FOCS '04: Proceedings of the 45th Annual IEEE Symposium on Foundations of Computer Science*, pages 42–51, Washington, DC, USA, 2004. IEEE Computer Society.

[89] E. Farhi, J. Goldstone, S. Gutmann, and D. Nagaj. How to make the quantum adiabatic algorithm fail, 2005.

[90] B. W. Reichardt. The quantum adiabatic optimization algorithm and local minima. In *STOC '04: Proceedings of the thirty-sixth annual ACM symposium on Theory of computing*, pages 502–510, New York, NY, USA, 2004. ACM.

[91] Z. Wei and M. Ying. Quantum adiabatic evolutions that can't be used to design efficient algorithms, 2006. quant-ph/0604077.

[92] M. Znidaric and M. Horvat. Exponential complexity of an adiabatic algorithm for an np-complete problem. *Phys. Rev. A*, 73:022329, 2006.

[93] E. Farhi, J. Goldstone, and S. Gutmann. A numerical study of the performance of a quantum adiabatic evolution algorithm for satisfiability, 2000.

[94] E. Farhi, J. Goldstone, S. Gutmann, J. Lapan, A. Lundgren, and D. Preda. A quantum adiabatic evolution algorithm applied to random instances of an np-complete problem. *Science*, 292:472, 2001.

[95] J. Roland and N. J. Cerf. Quantum search by local adiabatic evolution. *Phys. Rev. A*, 65:042308, 2002.

[96] A. M. Childs, E. Farhi, and J. Preskill. Robustness of adiabatic quantum computation. *Phys. Rev. A*, 65:012322, 2001.

[97] R. Monasson and R. Zecchina. Entropy of the k-satisfiability problem. *Phys. Rev. Lett.*, 76:3881–3885, 1996.

[98] S. Cocco and R. Monasson. Trajectories in phase diagrams, growth processes, and computational complexity: How search algorithms solve the 3-satisfiability problem. *Phys. Rev. Lett.*, 86:1654–1657, 2001.

[99] J. I. Latorre and R. Orús. Adiabatic quantum computation and quantum phase transitions. *Phys. Rev. A*, 69:062302, 2004.

[100] R. Orús and J. I. Latorre. Universality of entanglement and quantum-computation complexity. *Phys. Rev. A*, 69:052308, 2004.

[101] J. Roland and N. J. Cerf. Adiabatic quantum search algorithm for structured problems. *Phys. Rev. A*, 68:062312, 2003.

[102] E. Farhi, J. Goldstone, and S. Gutmann. Quantum adiabatic evolution algorithms with different paths, 2002. quant-ph/0208135.

[103] W. K. Wootters. Entanglement of formation of an arbitrary state of two qubits. *Phys. Rev. Lett.*, 80:2245–2248, 1998.

[104] X. Wang and K. Mølmer. Pairwise entanglement in symmetric multi-qubit systems. *Eur. Phys. J. D*, 18:385–391, 2002.

[105] J. Vidal. Concurrence in collective models. *Phys. Rev. A*, 73:062318, 2006.

[106] L. D. Landau. *Phys. Z. Sow. Union*, 2:46, 1932.

[107] C. Zener. 1932. *Proc. Roy. Soc. A*, 137:696.

[108] G. E. Santoro and E. Tosatti. Optimization using quantum mechanics: quantum annealing through adiabatic evolution. *J. Phys. A*, 39:R393–R431, 2006.

[109] S. Brundobler and V. Elser. S-matrix for generalized landau-zener problem. *J. Phys. A*, 26:1211–1227, 1993.

[110] R. I. Cukier, M. Morillo, and J. M. Casado. Dynamics of single and multiple zener transitions. *Phys. Rev. B*, 45:1213–1222, 1992.

[111] Y. Kayanuma. Role of phase coherence in the transition dynamics of a periodically driven two-level system. *Phys. Rev. A*, 50:843–845, 1994.

[112] Q. Niu and M. G. Raizen. How landau-zener tunneling takes time. *Phys. Rev. Lett.*, 80:3491–3494, 1998.

[113] K. Mullen, E. Ben-Jacob, Y. Gefen, and Z. Schuss. Time of zener tunneling. *Phys. Rev. Lett.*, 62:2543–2546, 1989.

[114] V.I. Arnold. *Mathematical methods of classical mechanics, 2nd edition*. Springer, 1979.

[115] N. V. Prokof'ev and P. C. E. Stamp. Theory of the spin bath. *Reports on Progress in Physics*, 63:669–726, 2000.

[116] D. Mermin. Can a phase transition make quantum mechanics less embarrassing? *Physica A*, 177:561–566, 1991.

[117] D. Ellinas and V.s Kovanis. Motion of the wave-function zeros in spin-boson systems. *Phys. Rev. A*, 51:4230–4239, 1995.

[118] H.-P. Breuer, D. Burgarth, and F. Petruccione. Non-markovian dynamics in a spin star system: Exact solution and approximation techniques. *Phys. Rev. B*, 70:045323, 2004.

[119] M. Bortz and J. Stolze. Exact dynamics in the inhomogeneous central-spin model. *Phys. Rev. B*, 76:014304, 2007.

[120] G. Levine and V. N. Muthukumar. Localization transition in the mermin model. *Phys. Rev. B*, 63:245112, 2001.

[121] M. Bortz and J. Stolze. Spin and entanglement dynamics in the central-spin model with homogeneous couplings. *J. Stat. Mech. : Theor. Exp.*, 2007:P06018, 2007.

[122] M. Lucamarini, S. Paganelli, and S. Mancini. Two-qubit entanglement dynamics in a symmetry-broken environment. *Phys. Rev. A*, 69:062308, 2004.

[123] G. A. Finney and J. Gea-Banacloche. Quantum suppression of chaos in the spin-boson model. *Phys. Rev. E*, 54:1449–1456, 1996.

[124] A. Zeilinger D. Bouwmeester, A. K. Ekert. *The Physics of Quantum Information: Quantum Cryptography, Quantum Teleportation, Quantum Computation*. Springer, 2000.

[125] M. Kuś and K. Życzkowski. Geometry of entangled states. *Phys. Rev. A*, 63:032307, 2001.

[126] P. Lévay. The geometry of entanglement: metrics, connections and the geometric phase. *J. Phys. A*, 37:1821–1841, 2004.

[127] R. Mosseri and R. Dandoloff. Geometry of entangled states, bloch spheres and hopf fibrations. *J. Phys. A*, 34:10243–10252, 2001.

[128] B. A. Bernevig and H.-D. Chen. Geometry of the three-qubit state, entanglement and division algebras. *J. Phys. A*, 36:8325–8339, 2003.

[129] R. Mosseri. *"Topology in Condensed Matter", Springer Series in Solid-State Physics n. 150*, pages 187–203. Springer-Verlag, 2006. quant-ph/0310053.

[130] V. Coffman, J. Kundu, and W. K. Wootters. Distributed entanglement. *Phys. Rev. A*, 61:052306, 2000.

[131] J. Kempe. Multiparticle entanglement and its applications to cryptography. *Phys. Rev. A*, 60:910–916, 1999.

[132] C. Rigetti, R. Mosseri, and M. Devoret. *Quantum Information Processing*, pages 351–380. Springer, 2004. quant-ph/0312196.

[133] H. S. M. Coxeter. *Regular Polytopes*. Dover Publications, 1974.

[134] J. F. Sadoc and R. Mosseri. *Geometric Frustration*. Cambridge University Press, 1999.

[135] J. F. Sadoc and R. Mosseri. The e8 lattice and quasicrystals: geometry, number theory and quasicrystals. *Journal of Physics A: Mathematical and General*, 26:1789–1809, 1993.

[136] N. S. Manton. Connections on discrete fibre bundles. *Commun. Math. Phys.*, 113:341, 1987.

[137] Conway and Sloane. *Sphere Packings, Lattices and Groups*. Springer Verlag, New York, 1988.

[138] J. Leech. Some sphere packings in higher space. *Canad. J. Math.*, 16:657–682, 1964.

[139] D. C. Meredith, S. E. Koonin, and M. R. Zirnbauer. Quantum chaos in a schematic shell model. *Phys. Rev. A*, 37:3499–3513, 1988.

[140] W.-M. Zhang, Da H. Feng, J.-M. Yuan, and S.-J. Wang. Integrability and nonintegrability of quantum systems: Quantum integrability and dynamical symmetry. *Phys. Rev. A*, 40:438–447, 1989.

[141] P. Leboeuf and M. Saraceno. Structure of eigenfunctions in terms of classical trajectories in an su(3) schematic shell model. *Phys. Rev. A*, 41:4614–4624, 1990.

[142] R. Gilmore. *Lie Groups, Lie Algebras, and Some of Their Applications.* Dover Publications, 2006.

[143] M. B. Cibils, Y. Cuche, P. Leboeuf, and W. F. Wreszinski. Zeros of the husimi functions of the spin-boson model. *Phys. Rev. A*, 46:4560–4568, 1992.